Samo Stanič

Search for charged Higgs bosons at LEP 2 collider

Doctoral Thesis

Supervisor: prof. dr. Danilo Zavrtanik

Ljubljana, 1999

Samo Stanič

Iskanje nabitih Higgsovih bozonov s trkalnikom LEP 2

Disertacija

Mentor: prof. dr. Danilo Zavrtanik

Abstract

According to our present knowledge, Higgs bosons have a key role in the Standard model of elementary particle physics. All elementary particles, leptons, quarks and gauge bosons obtain their masses from their couplings to the Higgs boson. Standard model incorporates mathematically simplest Higgs boson sector, giving one neutral Higgs boson. Extensions of the Standard model require also the existence of charged Higgs bosons. However, the model or its extensions do not predict the Higgs boson mass and none of them were yet experimentally discovered.

We searched for decay signatures of charged Higgs boson decays in the LEP electron-positron collisions at centre-of-mass energy $183\,\mathrm{GeV}$. Data was collected by the DELPHI spectrometer. According to the model, charged Higgs bosons are produced through photon and Z^0 exchanges and decay either hadronically into a $c\bar{s}$ or leptonically into $\tau\nu$ pair. Signal selection was optimised on simulated samples of charged Higgs boson decays and background reactions. With respect to the decay modes of the two Higgs bosons, the events were classified into hadronic, mixed and leptonic decay channel. Each of the channels was treated separately.

After the selection, data was checked against the remaining background. Since there was no statistically significant excess of data in any of the three decay channels, we derived upper limits on the charged Higgs boson production cross-section, weighted by unknown values of the decay branching ratios. To set a lower limit on the charged Higgs boson mass, data from all three channels were combined and checked against the model prediction. $m_{\mathrm{H}^\pm}$ was found to be more than $53.5\,\mathrm{GeV}/c^2$ with 95% confidence level.

Keywords: charged Higgs boson, Higgs boson mass, two doublet model,
          cross-section, DELPHI, LEP.

Povzetek

V Standardnem modelu močnih in elektrošibkih interakcij igrajo Higgsovi bozoni ključno vlogo, saj so glavni manjkajoči gradniki v sicer skladni zgradbi Standardnega modela osnovnih delcev in sil v naravi. Vsi osnovni delci, leptoni, kvarki in umeritveni bozoni dobijo mase preko sklopitev s Higgsovimi bozoni. Standardni model ima en sam nevtralen Higgsov bozon, nadgrajene različice pa zahtevajo poleg nevtralnih tudi nabite Higgsove bozone. Noben od modelov ne napoveduje mas Higgsovih bozonov, kar otežuje njihovo odkritje.

V meritvah trkov elektronov in pozitronov pri težiščni energiji $183\,\mathrm{GeV}$ na trkalniku LEP smo iskali razpade nabitih Higgsovih bozonov. Meritve so bile izvedene s spektrometrom DELPHI. Po nadgrajeni različici Standardnega modala pari nabiti Higgsovih bozonov pri trkih elektronov in pozitronov nastanejo preko izmenjave fotona ali nevtralnega šibkega bozona. Razpadejo bodisi hadronsko v pare kvarkov $c\bar{s}$ ali leptonsko v delce τ in odgovarjajoče nevtrine. Ločevanje signala od ozadja je bilo optimizirano s pomočjo simuliranih vzorcev razpadov nabitih Higgsovih bozonov in simuliranih vzorcev ostalih reakcij, ki predstavljajo ozadje. Glede na razpadna načina H^+ in H^- so bili izmerjeni podatki razvrščeni v hadronski, mešani in leptonski razpadni kanal. V različnih kanalih je analiza meritev potekala ločeno.

Po izbiri kandidatov za razpade nabitih Higgsovih bozonov smo izmerjene reakcije primerjali s simuliranimi rekacijami, ki predstavljajo ozadje. Ker v nobenem izmed treh razpadnih kanalov ni bilo statistično signifikantnega presežka izmerjenih kandidatov nad pričakovanim ozadjem, smo izračunali zgornje meje za produkcijski presek para $\mathrm{H}^+\mathrm{H}^-$, utežene z neznanimi vrednostmi razpadnih razvejitvenih razmerij. Meritve v vseh treh kanalih smo uporabili pri izračunu spodnje meje na masi nabitega Higgsovega bozona $m_{\mathrm{H}^\pm}$, ki je s 95% odstotno stopnjo zanesljivosti večja od $53.5\,\mathrm{GeV}/c^2$.

Ključne besede: nabiti Higgsov bozon, masa Higgsovega bozona, model z dvema dubletoma, presek, DELPHI, LEP.

Contents

Introduction

Nowadays it is generally believed [1] that a proper way of describing dynamics of a physical system is to take into account its symmetries. A theory, where symmetry transformations with respect to the appropriate symmetry group are space-time dependent (gauge symmetries), can be used to generate the system's dynamics - the gauge interactions. In the case of elementary particles, quarks and leptons, the symmetry groups that describe the system's behaviour are non-Abelian groups SU(2) and SU(3) together with the Abelian group U(1). The gauge theory constructed in this case is gauge invariant, which means that the Lagrangian does not change under local gauge transformations. It is also renormalisable, which means that the infinities encountered during the calculation can be isolated and removed. Since its first application in elementary particle physics [2], the predictions of the non-Abelian gauge theory have been in good agreement with the measured data. For this reason a non-Abelian gauge theory became the base of the Standard model of electroweak and strong interactions in use today.

However, the local gauge symmetries imposed by the non-Abelian gauge theory imply the existence of massless fermions, leptons and quarks, as well as massless gauge bosons. As this is not the case, since the elementary particle masses have been experimentally measured, it is necessary to break the gauge symmetries in some way and thus obtain particle masses. Nevertheless, it has to be done in a way that keeps the Lagrangian of the theory fully invariant under the chosen symmetry transformations, thus keeping the theory renormalisable [3]. This is being done by constructing a degenerate ground state of the system, a ground state that does not reflect the symmetry properties of the Lagrangian. By choosing one of the equivalent ground states as the physical vacuum state, the symmetry is no longer manifested in the degenerate energy levels, although the Lagrangian is still invariant under the symmetry transformations. Such a situation is referred to as a spontaneous symmetry breakdown. Perturbative expansion around the chosen vacuum state creates scalar fields [4], which are used up as the longitudinal polarisations of the massless gauge bosons, thus converting them into massive ones. This is called the Higgs mechanism [5]. In the Standard model, there is one remaining scalar field left which is identified with a real scalar particle - the Higgs boson. The rest of the particles in the Standard model - the fermions - also obtain their masses from their couplings to the Higgs boson, which thus plays the crucial role in the mass generation scheme.

The obvious thing to do in order to improve our knowledge about elementary particle

1

physics, is to detect the Higgs boson experimentally. One of the experimental estimates for the Standard model Higgs boson mass has been deduced from results, obtained from the high precision measurements at e^+e^- collider LEP. The theoretical aspect of the Standard model, stating that it becomes renormalisable only after including Higgs particles in the loop corrections for certain processes, is an indication that the electroweak observables should be sensitive to masses of these particles. The increasing precision of the measurements makes it possible to derive χ^2 curves as a function of $m_{H^\pm}$ by means of a global fit to electroweak data (figure 1). Results of the fit [6] favour a light Higgs boson with a central value of $m_{H^\pm}$ around $80\,\mathrm{GeV}$.
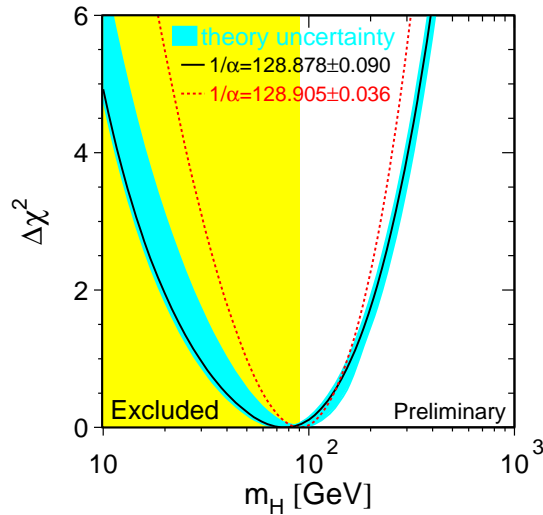
Figure 1: The change in χ^2 of the global electroweak data fit as the Higgs mass is varied between 10 and $400\,\mathrm{GeV}$. The blue band represents an estimate of the uncertainty from missing higher order corrections. The area shaded in yellow indicates the excluded region from the direct Higgs searches at LEP. The red curve shows the improvement in the indirect determination which is possible with a more precise estimate of $\alpha(m_Z^2)$.

These indirect bounds can assure neither the existence of a light Higgs boson in the mass range up to $100\,\mathrm{GeV}/c^2$, in the reach of the existing experiments, nor the existence of the Higgs boson in general, but are nevertheless a welcome stimulation for all kinds of the ongoing Higgs boson searches.

To be able to claim a discovery of a Higgs boson, it is necessary to detect a statistically significant signal reconstructed from its decay products. Since the Higgs boson mass is not predicted by the model, the range of such a measurement is limited by the energy available for the Higgs boson production. This kind of Higgs boson searches conducted at existing particle colliders have up to now not been able to confirm its existence. Lack of the Higgs boson signal has therefore been interpreted as a lower limit on the Higgs boson mass, up to which its existence has been excluded. From 1995 on, the centre-of-mass energy of the LEP collider at

CERN is being gradually increased from the original $90\,\mathrm{GeV}$ to the expected $200\,\mathrm{GeV}$ in 1999, opening a new possibility for the Higgs boson discovery in a much wider mass range.

The aim of this thesis was to exploit the newly achievable centre-of-mass energies of the LEP collider in the search for charged Higgs boson decay signatures among the products of e^+e^- collisions. The data used in the analysis was collected at the centre-of-mass energy of $183\,\mathrm{GeV}$ by the DELPHI spectrometer. First chapter of this work explains the specifics of the experimental setup with an emphasis on the DELPHI spectrometer and its sub-detectors, used in the analysis. A short phenomenological introduction to physics of Higgs bosons in the framework of Standard model and its extensions is given in the second chapter. Third chapter presents in detail data selection criteria and background estimation in the search for decay signatures of charged Higgs bosons. Results of the data selection, their interpretation and calculation of upper limits are described in chapter four. Finally, in the fifth chapter, the results are combined and conclusions are drawn.

1

Experimental Environment

1.1   Large Electron Positron Collider

The Large Electron Positron (LEP) collider is operating at the European particle physics laboratory (CERN) near Geneva. The beam pipe has 26.6 kilometres in circumference to reduce energy losses due to the synchrotron radiation. Four spectrometers, ALEPH, DELPHI, L3 and OPAL, are situated at four out of eight experimental halls on the collider ring. Map marking the position of CERN and LEP in the vicinity of Geneva is shown in figure 1.1. After its commissioning in 1989, LEP operated at a beam energy of $46\,\mathrm{GeV}$ for $\mathrm{e^+e^-}$ collisions at the $\mathrm{Z^0}$ resonance. Until 1995, LEP delivered an integrated luminosity of $200\,\mathrm{pb^{-1}}$ to each of the four experiments.

The acceleration of particles colliding at LEP is performed in several stages. Electrons from an electron gun and positrons from an electron converter are first accelerated to $600\,\mathrm{MeV}$ energy in the two linear accelerators followed by an electron-positron accumulator which injects the particles into the CERN Proton Synchrotron (PS). At the energy of $3.5\,\mathrm{GeV}$ particles are passed over from the PS into the CERN Super Proton Synchrotron (SPS). In the SPS electrons and positrons reach $22\,\mathrm{GeV}$, a starting energy for the injection into LEP.

Since October 1995 the beam energy in LEP is being gradually raised [7, 8, 9] from original $46\,\mathrm{GeV}$ to expected $100\,\mathrm{GeV}$ in 1999 and 2000, allowing to study the production of $\mathrm{W^+W^-}$ and $\mathrm{Z^0}$ pairs. This opens new possibilities for the Standard model tests as well as searches for new particles, especially Higgs bosons and supersymmetric particles.

LEP energy upgrade is being done in several steps, following the installation of an increasing number of superconducting radio-frequency cavities used for the acceleration. At present, LEP is operating with $\mathrm{e^+}$ and $\mathrm{e^-}$ beams each consisting of four bunches of particles. Final beam energy is $94.5\,\mathrm{GeV}$. At injection the bunch current is of the order of $760\,\mu\mathrm{A}$ and it reduces to $720\,\mu\mathrm{A}$ after losses during the acceleration from $22\,\mathrm{GeV}$ to $94.5\,\mathrm{GeV}$. Luminosity at injection time is $7\times10^{31}\,\mathrm{cm^{-2}s^{-1}}$ and lifetime of the two beams is of the order of 5 to 6 hours. A typical LEP fill for physics lasts 4 hours. Then LEP has to be refilled, which usually lasts between 60

and 90 minutes.
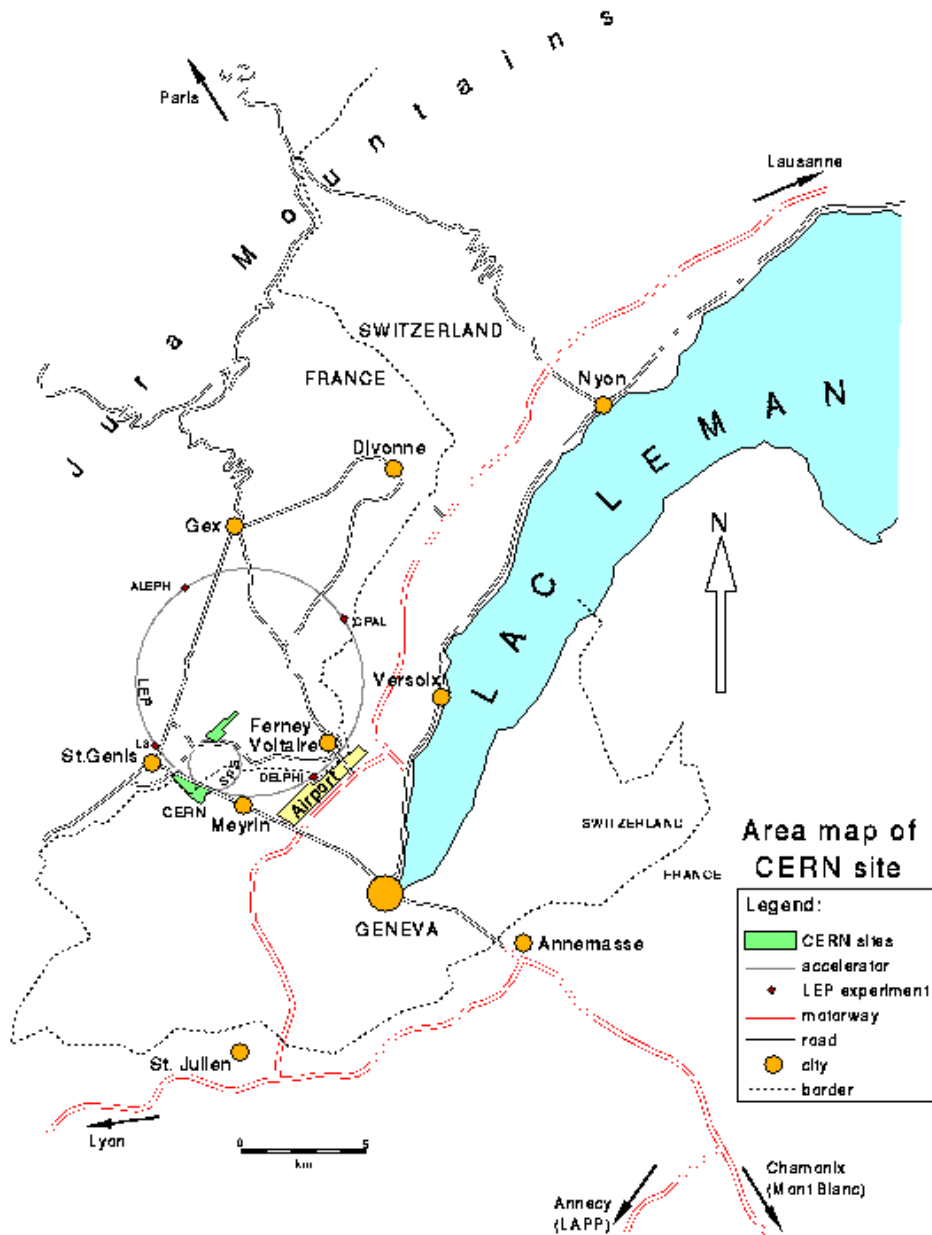
Figure 1.1: Surroundings of Geneva with CERN sites and LEP collider with marked experimental points.

Since the end of 1995 LEP has been operating and taking data at $130 - 136\,\mathrm{GeV}$, $161\,\mathrm{GeV}$, $172\,\mathrm{GeV}$, $183\,\mathrm{GeV}$ and $189\,\mathrm{GeV}$ centre-of-mass energy, with DELPHI recording respectively $6\,\mathrm{pb}^{-1}$, $10\,\mathrm{pb}^{-1}$, $10\,\mathrm{pb}^{-1}$, $54\,\mathrm{pb}^{-1}$ and $200\,\mathrm{pb}^{-1}$ of data. The total integrated luminosity as seen by the four experiments is summarised in figure 1.2.
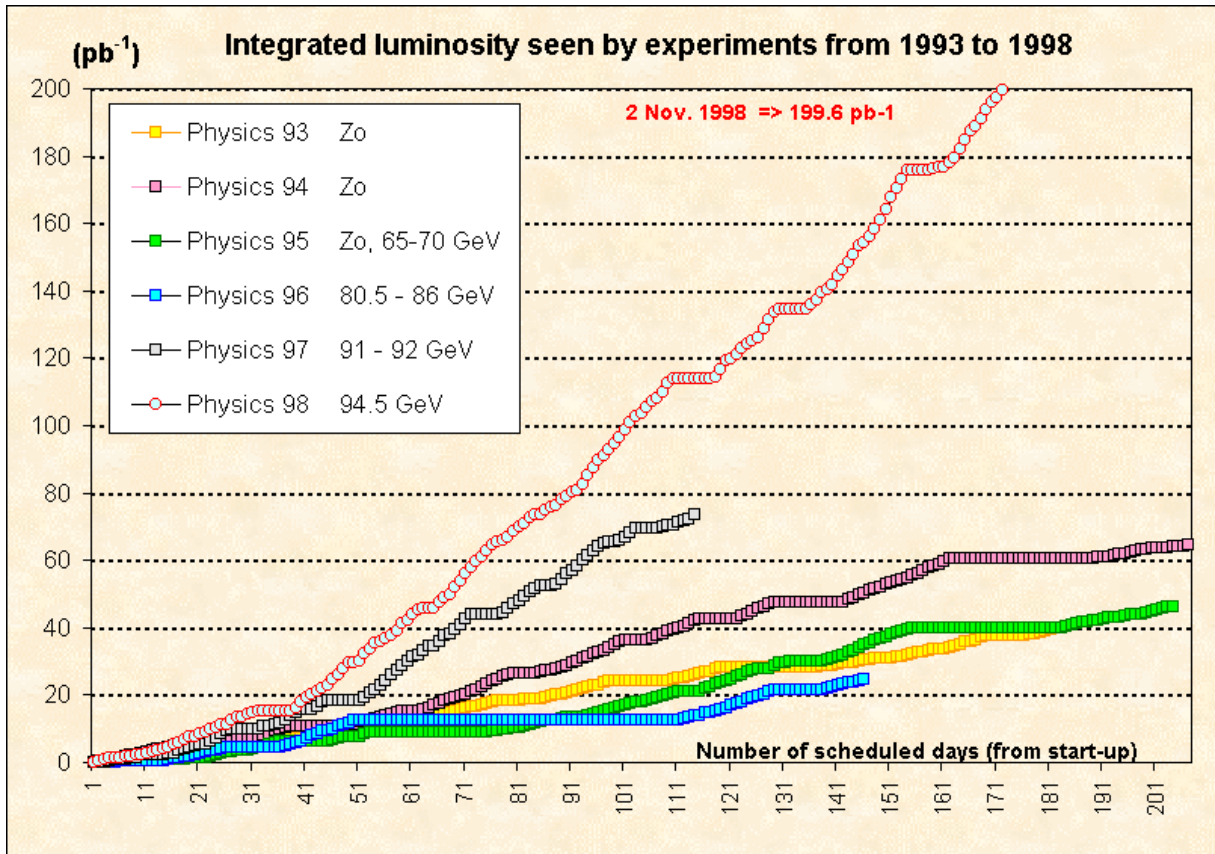
Figure 1.2: Integrated luminosity as seen by each of the four LEP experiments in years 1993 to 1998.

1.2 The DELPHI Spectrometer

DELPHI (**DE**tector with **L**epton, **P**hoton and **H**adron **I**dentification) spectrometer is one of the four spectrometers operating at the collider. Collaboration of physicists gathered around DELPHI spectrometer consists of more than 540 scientists from 53 institutes in 22 countries. Nine physicists from the Experimental Particle Physics Department of the Jožef Stefan Institute in Ljubljana are taking part in the collaboration as well.

The spectrometer was designed to identify and accurately track particles produced in e^+e^- collisions. It is composed of many detectors structured in a cylindrical shape (barrel) and two end-caps, covering most of the solid angle around the electron-positron interaction point. Both end-caps of 10 m diameter can be independently removed to allow access to specific detector components. A schematic view of the cross-section through the spectrometer is shown in figure 1.3. The spectrometer as well as the entire collider is installed in a tunnel 100 meters below the surface.
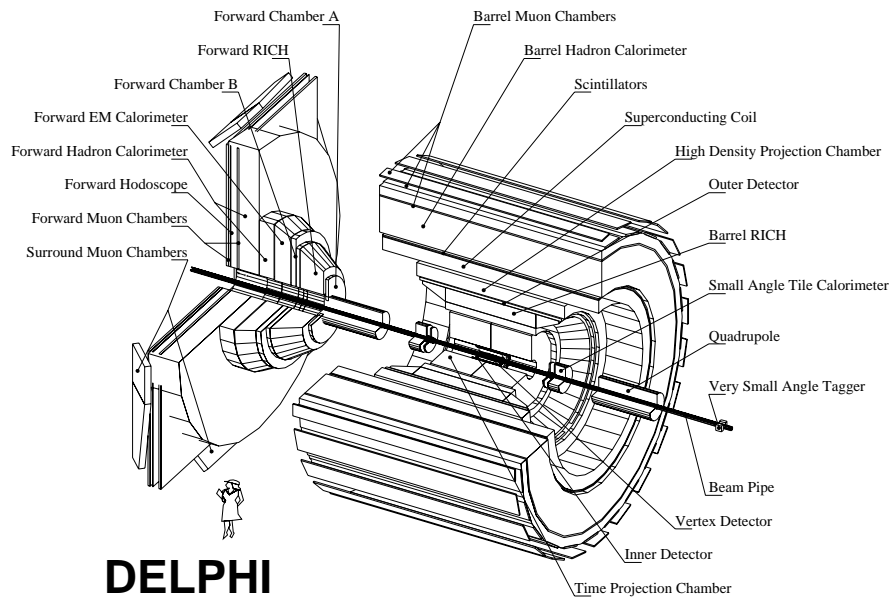
Figure 1.3: Schematic view of the DELPHI spectrometer.

Tracking detectors, Ring Imaging Čerenkov detectors and Electromagnetic calorimeter are placed inside a superconducting solenoid, which produces a uniform magnetic field in the direction of the beam axis. Magnitude of the longitudinal component of the field inside the Time Projection Chamber (see description below) is $B_z = 1.2334 \pm {}^{0.0001}_{0.0010}$ T [10], while the magnitude of the radial component is less than 0.0005 T. Outside the solenoid are the time of flight counters, hadron calorimeter and muon chambers. The end-caps of the spectrometer are composed

in a similar way. Nearest to the beam-pipe in each of the end-caps is a luminosity monitor followed by tracking chambers, forward Ring Imaging Čerenkov detectors, calorimeters and muon chambers.

A complete description of the spectrometer can be found elsewhere [10, 11]. In the following we will briefly review the most important properties of detectors relevant to the analysis presented in this work. We shall use the coordinate system with the z-axis parallel to the electron beam. The radial coordinate R is measured from the beam axis and the azimuth angle φ in the plane perpendicular to it. θ is the polar angle with respect to the z-axis.

1.2.1   Tracking Detectors

Tracking part of DELPHI is placed inside a homogeneous magnetic field and is used to reconstruct tracks of charged particles. It consists of the Silicon Tracker, Inner Detector (ID), Time Projection Chamber (TPC) and Outer Detector (OD) in the barrel region, and Forward chambers.

- Silicon Tracker
  At the beginning of high centre-of-mass energy runs at LEP the Silicon Tracker has undergone an upgrade to meet the new physics requirements. It now consists of a Vertex Detector in the barrel region and of Very Forward Tracker in the forward region [13].

  The barrel region consists of three concentric layers of silicon micro-strip detectors around the beam pipe. The Closer layer lies at a radius of 63 mm, the Inner at 90 mm and the Outer at 109 mm. The layers involve modules which consist of two electrically independent half-modules joined together in the centre. Length of the barrel part of Silicon Tracker is 48 cm. The long barrel requires a good mechanical stability which is achieved by a carbon-fibre honeycomb support between the layers.

  The interval of polar angles in which the particle originating from the interaction point crosses all three layers of the Vertex Detector is $27° \leq \theta \leq 153°$. Apart from the central part of the Inner layer, which provides only two-dimensional information, all modules of the Vertex Detector enable the measurement of the (R, φ) as well as of the z coordinate.

  A schematic view of the Silicon Tracker is shown in figure 1.4. The Vertex Detector enables high precision measurements of a track position in the vicinity of a primary vertex and improves the particle momentum resolution. It is used to reconstruct decay vertices of particles with decay lengths from a few milimeters to about $10 \, \mathrm{cm}$ and is indispensable for tagging events that contain heavy quarks. Charged particles, crossing the Vertex Detector, ionize atoms of the semiconducting material. Coordinates of the tracks are obtained from the division of the charge, released in the semiconductor, among several sense strips of the detector. A single layer of the detector provides a measurement of the track position with a precision of $7.6 \, \mu\mathrm{m}$ and approximately $100 \, \mu\mathrm{m}$ double track separation in the $R\varphi$
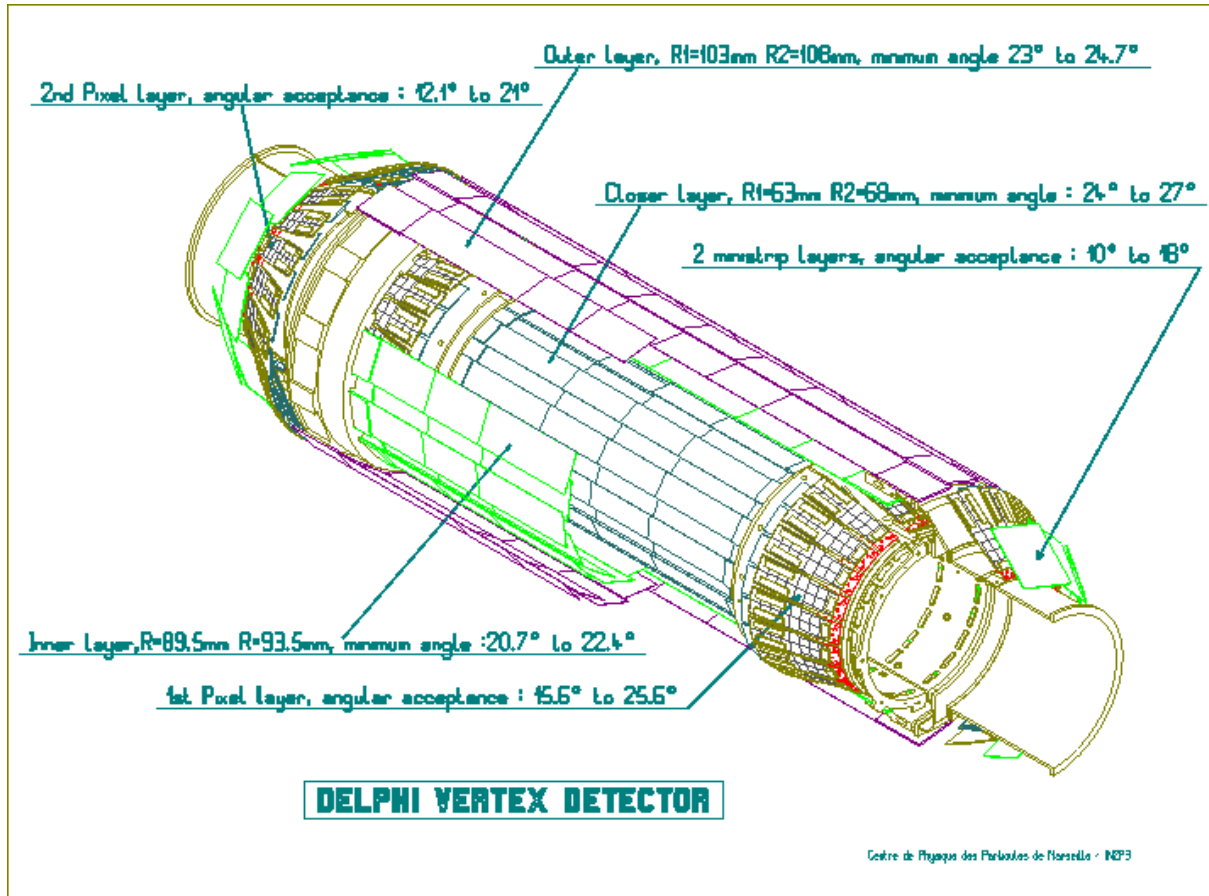
Figure 1.4: Schematic view of the DELPHI Silicon Tracker.

coordinate, averaged over the polar angle [10]. In the z coordinate single hit precision varies from 9 μm at $\theta = 90°$ to around 30 μm at $\theta = 45°$ [14].

The Very Forward Tracker (VFT) is located on each side of the Vertex Detector and consists of two layers of mini-strip and two layers of pixel detectors. VFT covers polar angles from $10°$ to $25°$. Each layer of the pixel detectors is made of two crowns of modules rotated against each other to cover the holes between the modules. A pixel detector crown has 18 to 20 modules, each containing 8064 detector elements. In total, the pixel detectors provide about 1.2 million detector elements (pixels) each with dimensions $330 \times 330 \mu m^2$. Intrinsic resolution for tracks orthogonal to the detector plane is better than $100 \mu m$ [15].

Each layer of the mini strip detector is made of two half rings with 6 detector modules. A module is formed by two single-sided strip detectors assembled back to back with perpendicular strip orientation. In total there are 48 mini strip modules consisting of 96 detectors. All the mini strip modules installed provide about 24.500 readout channels. Ministrip modules provide intrinsic resolution of about $30 \mu m$ [16].

- Inner Detector (ID)

  The Inner Detector is a tracking and triggering detector mounted at radii between 12 and 28 cm. Its geometrical acceptance is from $15°$ to $165°$ in the polar angle ϑ. It consists of two parts: a JET chamber providing and Trigger Layers (TL), providing the (R, φ) coordinate. A schematical view of the ID is shown in figure 1.5.

  JET chamber is a drift chamber, subdivided into 24 sectors of $15°$ in φ. Each sector consists of 24 sense wires, measuring the drift time. TL consist of 5 cylindrical layers of 192 straw tubes of about 8 mm in diameter. The tubes in subsequent planes are staggered by half a cell.
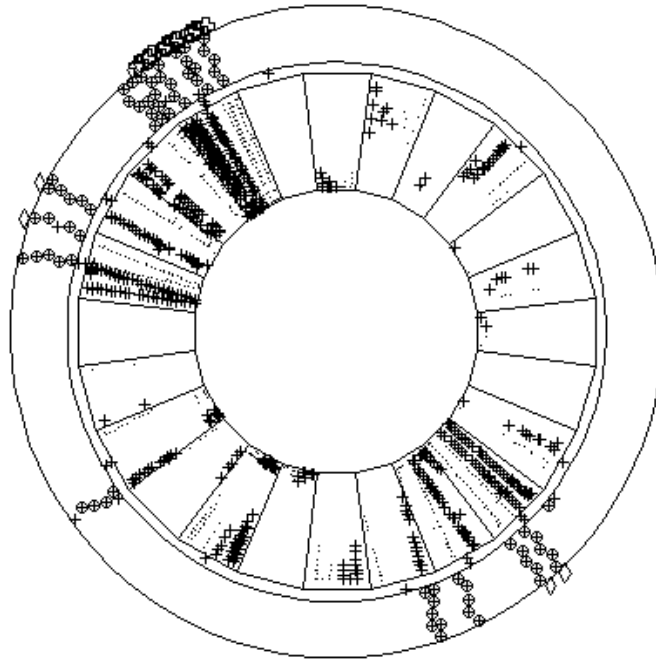
Figure 1.5: Schematic view of the Inner Detector. Each φ module is made of a drift chamber and 5 layers of straw tubes.

  The (R, φ) coordinate of a track traversing the JET chamber is determined from the measured drift time of electrons from ionization. For each event the JET chamber measures up to 24 and TL up to 5 points in $R\varphi$ plane for a given charged track. The achieved single wire resolution in the JET chamber is of the order of $90\,\mu$m, depending on the drift distance. The drift time does not provide information on the direction of the drift. These inherent left-right ambiguities of drift chambers are resolved by the straw tube Trigger Layers. Combined with the TE the total resolution is of the order of $40\,\mu$m in $R\varphi$ and

about 1.2 mrad in the angle φ. Separation resolution for two charged tracks is of the order of 1 mm.

- Time Projection Chamber (TPC)

  The TPC [12] is the most important tracking detector in DELPHI, since it is from the TPC response that a charged track reconstruction usually starts. The detector provides a 3-dimensional measurement of particle trajectories. A schematic view of the TPC is shown in figure 1.6. Electrons, produced in ionization of gas atoms in the TPC by a charged track, drift in the electric field parallel to the beam axis. From the drift time the z coordinate of the trajectory is reconstructed. Precision of the track position measurement in z direction depends crucially on the accurate knowledge of the electron drift velocity.
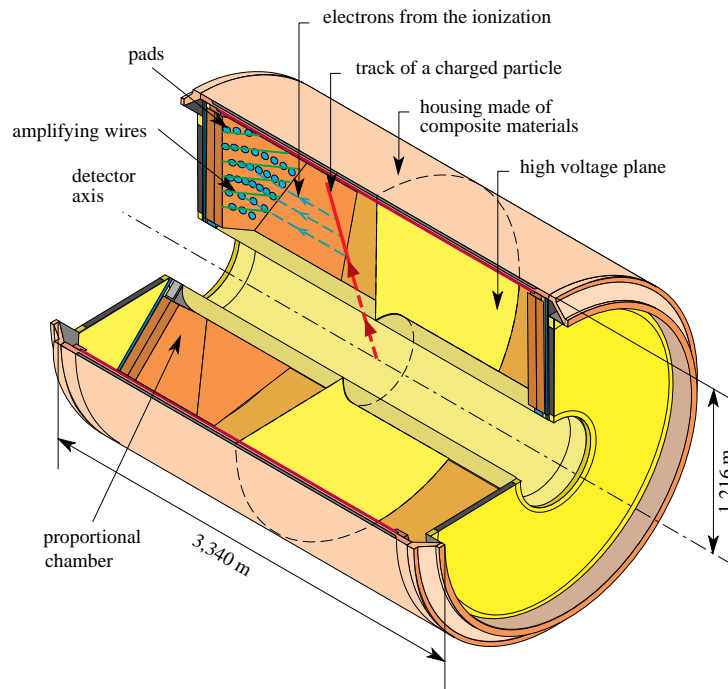
Figure 1.6: Schematic view of the TPC.

At both end-caps of the TPC, drifting electrons enter the multi-wire proportional chambers. Each chamber is divided into 6 sector plates with 192 sense wires and 16 circular pad rows. The induced electric signal on the cathode pads serves for the measurement of the (R, φ) coordinate of the charged track. The granularity of pads determines the spatial resolution of the detector in this coordinate. Pads give up to 16 measurements of the (R, φ) coordinate between $R \approx 35$ cm and $R \approx 111$ cm. If one requires at least 3 pad rows to be hit, the angular acceptance of the TPC is between $\theta = 20°$ and $\theta = 160°$.

The high voltage plane provides an electric field $E = 187$ V/cm [10], resulting in electron drift velocity of $v_d \approx 7$ cm/μs at T=29°C. The spatial resolution for a single pad row

(measured for $Z^0 \rightarrow \mu^+\mu^-$) is $250\,\mu$m in $R\varphi$ and $880\,\mu$m in z [10]. Signals from two tracks can be separated if the distance between the tracks is at least 1 cm.

Apart from accurate position measurements, the TPC also provides information for particle identification. Each sense wire performs a dE/dx measurement which will be discussed in the section on combined charged particle identification with DELPHI.

- Outer Detector (OD)
  The OD completes the tracking in the barrel region. It consists of 24 azimuthal modules, each one containing 145 drift tubes, compounded in 5 layers. Layers of the drift tubes are shown in figure 1.7. Drift tubes in different layers overlap to give the full azimuthal coverage. The OD improves the momentum resolution particularly for fast particles.
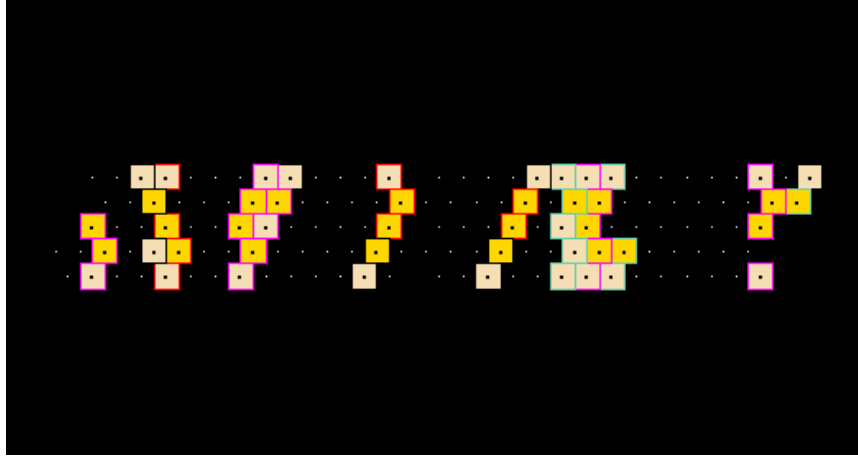
Figure 1.7: 5 layers of OD tubes shown in (R, φ) projection. Tubes, hit by charged particles, are displayed in colours.

Drift tubes are aligned parallel to the beam axis. While all the layers provide the (R, φ) coordinate, three of them measure the z position of a track as well. The z coordinate measurement is obtained by comparing the relative timing of electronic signals at both ends of the drift tube. Drift tubes cover the polar angles from $42°$ to $138°$ and are situated at radii between 197 and 206 cm. Single point precisions are $\sigma_{R\varphi} = 110\,\mu$m and $\sigma_z = 3.5\,$cm [10].

1.2.2 Calorimetry

The barrel and forward electromagnetic calorimeters are used to measure the deposited electromagnetic energy of particles with $43° \leq \theta \leq 137°$ and $10° \leq \theta \leq 36.5°$, $143.5° \leq \theta \leq 170°$, respectively. The hadron calorimeter measures the energy of hadrons with polar angle between $10°$ and $170°$.

- Electromagnetic Calorimeter (HPC)

  The barrel electromagnetic calorimeter of the DELPHI spectrometer is called High Density Projection Chamber (HPC). HPC uses a large number of time-projection chambers for calorimetry measurements. The calorimeter is composed of 144 modules, separated into 6 rings along the beam axis. Each ring includes 24 coaxially arranged modules with an inner radius of 208 cm and an outer radius of 260 cm. Polar angle coverage of the HPC is $43° < \theta < 137°$.

  Each module is a time-projection chamber. The gas volume of the chamber is in the radial direction intercepted by 41 lead walls. Electrons and photons, penetrating this high density material of HPC, induce electromagnetic showers. Charged particles from the showers ionize atoms of the gaseous parts of the chamber. Layers of lead, which serve as a converter material, provide also a constant drifting electric field for the electrons from ionization. One end of the module is equipped with a multi-wire proportional chamber. Like in the TPC, charge carriers released in the ionization, drift to the proportional chamber. They induce an electric signal on 128 cathode pads arranged in 9 rows.

  The response of the detector is monitored and calibrated by occasional small admixture of radioactive $^{83}\mathrm{Kr}^*$ to the gas of the time-projection chambers [17]. Electrons with an energy of about 40 keV are produced in the decay of $^{83}\mathrm{Kr}^*$. The charge, released by such electrons, is normally collected by a single cathode pad. This enables an equalisation of responses of individual pads to particles with a given energy deposition. The final energy calibration of HPC is performed with electrons and positrons of precisely known energy, arising from Bhabha scattering.

  The total thickness of lead layers in each HPC module corresponds to 17.5 radiation lengths in the direction perpendicular to the beam axis [18]. The time-projection method used in the calorimeter enables a measurement of showers, induced by Bhabha electrons and positrons. Spatial resolution in z is from 1.3 to $3.1\,\mathrm{mm}$, depending on polar angle, and around $0.2°$ in azimuthal angle φ. The relative energy resolution for these particles is $(6.4 \pm 0.2)\%$ [18]. The precision of energy measurement for lower energy particles is obtained from the decays of neutral pions into two photons. 7% of the photons convert into $\mathrm{e}^+\mathrm{e}^-$ pairs in front of the TPC and can thus be measured with a high precision. One can use the position and the width of the π^0 invariant mass peak, reconstructed from one converted photon and one photon detected in the HPC, to obtain the resolution on the measured photon energy [10]:

  $$\frac{\sigma(E)}{E} = \sqrt{(0.043)^2 + \frac{(0.32)^2\,\mathrm{GeV}}{E}} \,. \tag{1.1}$$

- Hadron Calorimeter (HCAL)

  The barrel HCAL consists of streamer tubes, inserted in 1.8 cm slots between 5.0 cm thick

iron plates of the return yoke of the DELPHI solenoid. 20 layers of tubes are mounted between $R = 3.20$ m and $R = 4.79$ m. Tubes are grouped in modules. 24 modules cover a full azimuthal range.

Hadrons, entering the HCAL, strongly interact in the iron plates and produce hadronic showers, which are almost completely absorbed in the detector. Muons loose energy dominantly through ionization and leave only a fraction of their energy in the calorimeter.

Charge, released by ionization of the gas in streamer tubes, induces a signal on the cathode pads. Each pad covers an angular region of $2.96°$ in θ and $3.75°$ in φ [10]. The electronic signal from streamer tubes is independent of the amount of ionization produced by a charged particle. The energy is measured from the number of hits in different tubes, which is of course larger for hadronic showers than for penetrating muons. Calibration is performed using di-muon decays of Z^0 and the total deposited energy in hadronic decays of Z^0.

The calibration of hadronic shower energy is checked by comparing the measured energy of a single pion, arising from $\tau^- \to \pi^- \nu_\tau$ decays, with momentum of the pion, measured in tracking detectors. The precision of the energy measurement in the hadronic calorimeter is determined to be [10]

$$\frac{\sigma(E)}{E} = \sqrt{(0.21)^2 + \frac{(1.12)^2\,\text{GeV}}{E}}\,. \tag{1.2}$$

1.2.3 Charged Particle Identification

- Electron Identification
  Electron identification is performed from two independent pieces of information [19]. The first one relies on the energy deposition of particles in the electromagnetic calorimeter (HPC). In the HPC one uses the ratio of the particle's energy and momentum, directional mismatch between the reconstructed charged track and electromagnetic shower, and the longitudinal profile of the shower to discriminate between electrons and other charged particles. The second piece of information is the dE/dx measurement in the TPC.

  Electrons and positrons, unlike other charged particles, are completely absorbed in the HPC. The ratio of the deposited energy and momentum, measured with tracking devices, should thus be close to unity. The measured E/p ratio of a certain track is compared to the one, expected for electrons. The agreement is expressed as a probability for a track being an electron.

  Showers produced by particles penetrating the HPC are associated to tracks reconstructed in the TPC. A difference between the reconstructed track and the direction of the associated shower, in z and φ coordinates, enables to exclude showers, produced by neutral particles.

Finally, the expected energy deposition rate dE/dt [20], where t is the shower depth, expressed in units of radiation length, is fitted to the measured energy deposition in the HPC. The quality of the fit, given by a χ^2 probability, can be used to determine whether the shower is of electromagnetic origin.

The second piece of information used in the electron identification is dE/dx measurement in the TPC. Specific ionization is sampled by 192 anode wires of the TPC. Signals arising from nearby tracks cannot be correctly separated and are not used for the dE/dx measurement. The minimum track distance enabling a separate measurement of dE/dx is around 2 cm [10]. In order to reduce the effect of the Landau distribution tail, the average energy loss is calculated from 80% of lowest amplitudes of the wire signals. By requiring at least 30 TPC sense wires to give a signal the relative precision on this truncated mean is found to be 7.4% for particles in hadronic jets [10]. This gives above 2σ separation between electrons and pions with momenta up to $20\,\mathrm{GeV}/c$. Figure 1.8 shows the specific ionization of electrons and their separation from hadrons as a function of particles momenta.
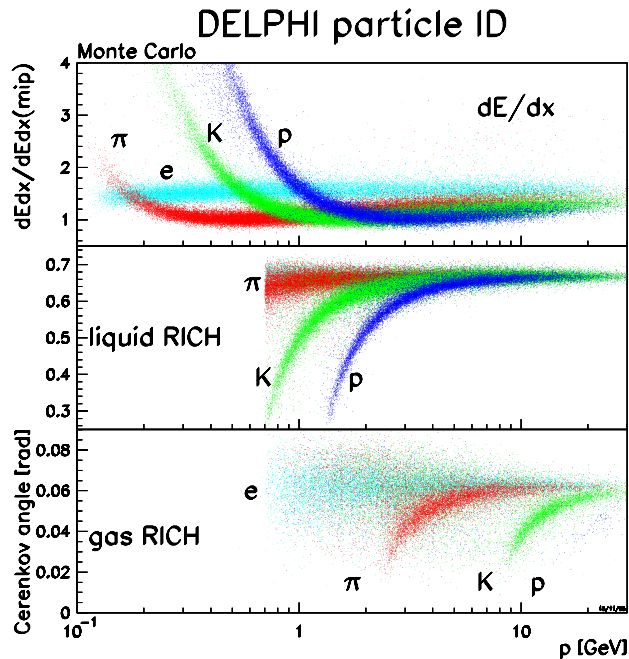
Figure 1.8: Specific ionization reconstructed by the TPC and Čerenkov angle reconstructed by the RICH for electrons and different types of hadrons as a function of the particle momentum [10]. The specific ionization is normalised to the dE/dx of minimum ionizing particles. Plots shown are the result of the reconstruction for simulated hadronic Z^0 decays.

The combination of both measurements yields a classification of electrons with momentum above $2\,\mathrm{GeV}/c$ into three categories: loose, standard and tight. They are sorted

according to decreasing efficiency and increasing purity of the electron sample. Efficiencies and typical misidentification probabilities of different tags for electrons in hadronic Z^0 decays are given in table 1.1 [10]. Misidentification probability is defined as probability for a single pion, arising from $K_s^0 \to \pi^+ \pi^-$ decays, to be identified as an electron.

Tag	Efficiency [%]	Misid. probability [%]
Loose	80	≈ 1.6
Standard	55	≈ 0.4
Tight	45	≈ 0.2

Table 1.1: Efficiencies and misidentification probabilities, averaged over momentum and direction of tracks, for different tags of electron identification (taken from [10]). Misidentification probabilities are measured on selected $K_s^0 \to \pi^+ \pi^-$ decays.

Photons, converted into electron-positron pairs in material in front of the TPC are also reconstructed and the electrons from such a process are tagged.

- Muon Identification
  The separation between hadrons and muons is provided by the iron of the Hadron Calorimeter (HCAL). This material prevents the majority of hadrons to enter five planes of Muon Chambers (MUC), located in the final part and outside the HCAL. However, there are still residual hadronic tracks, or remnants of the hadronic showers developed in the HCAL, that are traversing the material in front of the MUC. Hits in the drift chambers of the MUC which are produced by such punch-through are more scattered than hits produced by the prompt muons. Hence an additional suppression of the background is obtained by performing a χ^2 fit to extrapolated tracks from the tracking part of the spectrometer together with associated hits in the MUC. Tracks with associated hits are tagged as tight, standard, loose or very loose muon candidates, each tag corresponding to a different cut on the χ^2 of the fit. Standard and tight tags require also an associated hit in one of the two outermost layers of the MUC.

  The efficiency for muon identification was determined from data. Decays of Z^0 into muon pairs provide a source of muons which can be easily identified from the topology of events. The same is valid also for $Z^0 \to \tau^+ \tau^-$ decays, where one of τ leptons decays into a muon. The latter sample can be used for extraction of misidentification probability as well. For that purpose, τ decays into pions were used. Efficiencies are given in table 1.2 [10], together with probability for pions to be identified as muons.

- Charged Hadron Identification
  In DELPHI, charged hadrons are being identified by dE/dx measurements in the TPC and with the Ring Imaging Čerenkov Detectors (RICH). The measurement of specific ionization is performed as described in the section about the electron identification. A

Tag	Efficiency [%]	Misid. probability [%]
Very Loose	95.9 ± 0.1	5.4 ± 0.2
Loose	94.8 ± 0.1	1.5 ± 0.1
Standard	86.1 ± 0.2	0.7 ± 0.1
Tight	76.0 ± 0.2	0.4 ± 0.1

Table 1.2: Efficiencies and misidentification probabilities, averaged over momentum and direction of tracks, for different tags of muon identification (taken from [20]).

dE/dx value is available for about 75% of the particles in hadronic Z^0 decays. The inefficiency is mostly due to the imposed cut on the number of wires hit by a track, and due to a 2 cm two track separation in the TPC. One σ level separation between kaons and pions for momenta above $2 \, \mathrm{GeV}/c$ is achieved by the specific ionization measurement alone [10] (see figure 1.8 for the plot of specific ionization for different hadrons).

The RICH detector contains two radiators in which particles emit Čerenkov light. The two radiators differ in the value of refractive index n. The angle between the direction of emitted photons and direction of the particle is

$$\cos \theta_c = \frac{1}{n} \sqrt{1 + \frac{M^2 c^2}{p^2}}, \tag{1.3}$$

where M and p are mass and momentum of the particle. By measuring the value of Čerenkov angle θ_c and given the momentum of the particle, one can reconstruct its mass.

Čerenkov light is emitted only above a certain threshold momentum which can readily be obtained from equation (1.3), imposing the inequality $\cos \theta_c \leq 1$. If the RICH is used for separation of particles below the threshold from those giving light in radiators, it is said to be used in a veto mode.

The Čerenkov angle as a function of the momentum is shown in figure 1.8 for different types of particles. The plot is a result of the reconstruction for a simulated sample of hadronic Z^0 decays [11]. Approximate momentum ranges for separation of pions, kaons and protons, using either reconstruction of the Čerenkov angle or a veto mode, are given in table 1.3 [21]. Pions and kaons, for example, are identified by a measurement of θ_c in the liquid radiator from $p \approx 0.7 \, \mathrm{GeV}/c$ (threshold for kaons Čerenkov radiation) to $p \approx 5 \, \mathrm{GeV}/c$. The veto mode in the gas radiator can be used from $2.5 \, \mathrm{GeV}/c$, where pions start to radiate, to $8.5 \, \mathrm{GeV}/c$, the momentum, up to which kaons do not emit light. The Čerenkov angle for kaons in the gas radiator can thus be reconstructed from $8.5 \, \mathrm{GeV}/c$, and distinguished from θ_c for pions up to $p \approx 21 \, \mathrm{GeV}/c$.

Expected values of θ_c are determined from data over a wide range of momenta, using clean samples of particles, e.g pions from K_s^0 decays. Knowing the expected angles for

	$K^\pm/\pi^\pm$	$p^\pm/\pi^\pm$	$K^\pm/p^\pm$
Liquid, θ_c	0.7 - 5.0	1.5 - 7.5	0.7 - 7.5
Gas, veto	2.5 - 8.5	2.5 - 16	8.5 - 16
Gas, θ_c	8.5 - 21	16 - 25	16 - 25

Table 1.3: Approximate momentum ranges (in GeV/c) for separation of pions, kaons and protons, with measurement of Čerenkov angle or using a veto mode in the RICH detector (taken from [21]).

different particles, the measured value can be translated into a probability for a track being due to a pion, kaon or proton. This probability is combined with an analogous quantity obtained by the dE/dx measurement in the TPC.

The combined measurements of dE/dx in the TPC and Čerenkov angle in the RICH provide a tight, standard, loose and very loose tag for kaons and protons, offering a selection of particle samples with different efficiency and of different purity. By requiring, for example, the very loose kaon tag, kaons can be selected with an efficiency over 90%, averaged over the momentum and direction of particles. The purity, defined as a fraction of true kaons in the selected sample, is of the order of 30%. Tighter tags have lower efficiency and higher purity. For the standard tag both the efficiency and purity have a value of 70% [10].

2

The Higgs Boson

2.1 The Standard Model Higgs Boson

In the Standard Model [24], Higgs boson arises from the Higgs mechanism [5] as a direct physical manifestation of the origin of masses of elementary particles. Higgs mechanism is a way of introducing particle masses into a non-Abelian gauge theory that originally requires massless fermions and massless gauge bosons. Lagrangian density of such a model with massless particles can be written as

$$\mathcal{L} = \mathcal{L}^{\mathrm{F}} + \mathcal{L}^{\mathrm{B}}$$

where $\mathcal{L}^{\mathrm{F}}$ is the fermionic Lagrangian density and $\mathcal{L}^{\mathrm{B}}$ is the boson Lagrangian density and is exactly invariant under SU(2)×U(1) gauge transformations. In order to keep the theory renormalisable [3], masses must be generated in a way that preserves the Lagrangian invariance to symmetry transformations. This is achieved by adding a so called Higgs sector to the Standard Model Lagrangian:

$$\mathcal{L}^{\mathrm{H}} = (D_\mu \Phi)^\dagger (D^\mu \Phi) - V(\Phi). \tag{2.1}$$

$(D_\mu \Phi)^\dagger (D^\mu \Phi)$ is a kinetic term for the Higgs field Φ and D_μ are covariant derivatives,

$$D^\mu = \partial^\mu - ig\vec{W}_\mu \cdot \vec{T} - ig'\frac{Y}{2}B_\mu.$$

They include gauge fixing fields $\vec{W}_\mu$ associated with the generators T_i of $SU(2)$ gauge symmetry group and B_μ associated with Y of the $U(1)$ gauge symmetry group. In our case $Y = 1$ and T_i are Pauli matrices with $Tr(T_i, T_j) = \delta_{ij}$. The term $V(\Phi)$ is called the Higgs potential,

$$V(\Phi) = -\mu^2 \Phi^\dagger \Phi + \lambda(\Phi^\dagger \Phi)^2,$$

and has a quadratic and a quartic term in Higgs fields. Scalar field Φ is a complex doublet under weak $SU(2)$ gauge symmetry, providing four degrees of freedom,

$$\Phi = \begin{pmatrix} \Phi^+ \\ \Phi^0 \end{pmatrix}. \tag{2.2}$$

When $\mu^2 > 0$, the minimum of the potential $V(\Phi)$ is at

$$\langle \Phi^\dagger \Phi \rangle_0 = v^2/2, v = \sqrt{\mu^2/\lambda}. \tag{2.3}$$

The ground state is degenerate since the vacuum expectation value v still has an arbitrary phase. By choosing a particular phase, for example

$$\langle \Phi \rangle_0 = \frac{1}{\sqrt{2}} \begin{pmatrix} 0 \\ v \end{pmatrix}, \tag{2.4}$$

the symmetry is spontaneously broken.

An arbitrary Higgs field can be parametrized in terms of its deviations from the vacuum field Φ_0, for example as

$$\Phi(x) = \frac{1}{\sqrt{2}} \begin{pmatrix} \eta_1(x) + i\eta_2(x) \\ v + \sigma(x) + i\eta_3(x) \end{pmatrix}. \tag{2.5}$$

Using this parametrization, we can rewrite the Lagrangian density $\mathcal{L}^H$ (equation 2.1) in terms of four real fields $\sigma(x)$ and $\eta_i(x)$. By a SU(2)×U(1) gauge transformation, this isospinor can always be transformed into the form

$$\Phi(x) = \langle \Phi \rangle_0 + \Phi'(x) = \frac{1}{\sqrt{2}} \begin{pmatrix} 0 \\ v + \sigma(x) \end{pmatrix} \tag{2.6}$$

which no longer contains the fields $\eta_i(x)$, the so called unitary gauge. In this gauge, three of the four real Higgs fields $\eta_i(x)$ provide gauge invariant mass terms for three of the gauge bosons. The leftover field $\sigma(x)$ is interpreted as a real particle - the Standard model Higgs boson.

Technically, the mass terms of the gauge bosons are obtained by substituting $\Phi(x)$ (equation 2.6) into the covariant derivatives of the Lagrangian. Terms with the vacuum expectation value then yield [25]:

$$(D_\mu \langle \Phi \rangle_0)^\dagger (D^\mu \langle \Phi \rangle_0) = \frac{v^2}{8} \left[g^2 (W_{1\mu}^2 + W_{2\mu}^2) + (gW_{3\mu} - g'B_\mu)^2 \right]. \tag{2.7}$$

The first term,

$$\frac{1}{4} g^2 v^2 \frac{1}{\sqrt{2}} (W_1 + iW_2) \frac{1}{\sqrt{2}} (W_1 - iW_2)$$

are the $W^{\pm}$'s with mass $M_W^2 = g^2 v^2/4$. The second term,

$$\left(\frac{(gW_3 - g'B)}{\sqrt{g^2 + g'^2}}\right)^2$$

is the Z boson with mass $M_Z^2 = (g^2 + g'^2) v^2/4$. Combination $(g'W_3 - gB)/\sqrt{g^2 + g'^2}$ is not present in (2.7) since it represents a massless photon γ. Vacuum expectation value of the Higgs field was determined from measurements of the W boson mass [26] and Weinberg angle [27] to be

$$v = 2M_W/g = \frac{1}{\sqrt{G_F\sqrt{2}}} = 246 \,\mathrm{GeV}.$$

The Higgs boson mass itself, identified with the coefficient of the quadratic term of the remaining Higgs field $\sigma(x)$ in the Lagrangian density,

$$-\frac{1}{2} 2\lambda v^2 \sigma^2(x) = -\frac{1}{2} m_H^2 \sigma^2(x),$$

can unfortunately not be determined by any of the present measurements. Although the Standard Model is a successful theory at energies exploited nowadys, the Higgs sector is not understood very well from the fundamental point of view and the physics that underlies the Higgs mechanism is not yet certain. Since there is still no experimental information regarding the Higgs sector, it is necessary to explore the possibility of a more complicated symmetry breaking structures, of which the Standard Model incorporates only the simplest case. Such an example is a Higgs sector with more than one doublet of the Higgs fields. This scheme is adequate also for describing another possible symmetry in nature, the symmetry between bosons and fermions, called the supersymmetry.

2.2 Higgs bosons beyond the Minimal Standard Model

The most general way to extend the Higgs sector of the Standard Model is to add an additional doublet of complex fields in the Higgs potential [28, 29]. Such a potential is also used to describe the supersymmetric extensions of the Standard model. After choosing

$$\Phi_1 = \begin{pmatrix} \Phi_1^+ \\ \Phi_1^0 \end{pmatrix} \quad \Phi_2 = \begin{pmatrix} \Phi_2^+ \\ \Phi_2^0 \end{pmatrix}, \tag{2.8}$$

with $SU(2)_L$ hypercharge $Y = 1$ for the two doublets, the Higgs potential of the model becomes

$$
\begin{aligned}
V(\Phi_1, \Phi_2) &= \lambda_1 (\Phi_1^\dagger \Phi_1 - v_1^2)^2 + \lambda_2 (\Phi_2^\dagger \Phi_2 - v_2^2)^2 \\
&+ \lambda_3 \left[(\Phi_1^\dagger \Phi_1 - v_1^2)^2 + (\Phi_2^\dagger \Phi_2 - v_2^2)^2 \right]^2 \\
&+ \lambda_4 \left[(\Phi_1^\dagger \Phi_1)(\Phi_2^\dagger \Phi_2) - (\Phi_1^\dagger \Phi_2)(\Phi_2^\dagger \Phi_1) \right] \\
&+ \lambda_5 \left[\mathrm{Re}\,(\Phi_1^\dagger \Phi_2) - v_1 v_2 \cos \xi \right] \\
&+ \lambda_6 \left[\mathrm{Im}\,(\Phi_1^\dagger \Phi_2) - v_1 v_2 \sin \xi \right],
\end{aligned}
\tag{2.9}
$$

where parameters λ_i are real and the phase ξ can be rotated away in a special case of $\lambda_5 = \lambda_6$. This particular choice is made in the Minimal supersymmetric standard model, MSSM [30], so ξ can be set to 0. The quantities v_1 and v_2 are the vacuum expectation values of the two Higgs doublets, Φ_1 and Φ_2. In the unitary gauge, three out of eight degrees of freedom of (2.9) are used up for longitudinal polarisations of W and B fields, which subsequently give mass to $\mathrm{W}^\pm$ and Z bosons. The remaining five degrees of freedom are manifested as five physical Higgs bosons. Two of them are charged states,

$$\mathrm{H}^\pm = -\Phi_1^\pm \sin\beta + \Phi_2^\pm \cos\beta, \tag{2.10}$$

where the angle β is given by the ratio of the vacuum expectation values for the two doublets, $\tan\beta = v_2/v_1$. Other two are neutral scalar particles

$$
\begin{aligned}
\mathrm{H}^0 &= \sqrt{2}[(\mathrm{Re}\,\Phi_1^0 - v_1)\cos\alpha + (\mathrm{Re}\,\Phi_2^0 - v_2)\sin\alpha] \\
\mathrm{h}^0 &= \sqrt{2}[-(\mathrm{Re}\,\Phi_1^0 - v_1)\sin\alpha + (\mathrm{Re}\,\Phi_2^0 - v_2)\cos\alpha]
\end{aligned}
\tag{2.11}
$$

where H^0 is by convention the heavier one. Mixing angle α specifies the rotation necessary to diagonalise the neutral scalar Higgs mass matrix. The remaining particle is the pseudo-scalar Higgs:

$$A^0 = \sqrt{2}[-\mathrm{Im}\,\Phi_1^0 \sin\beta + \mathrm{Im}\,\Phi_2^0 \cos\beta]. \tag{2.12}$$

Instead of one parameter in the Standard Model - the Higgs mass - we have expanded to six arbitrary parameters in a two Higgs doublet model: four Higgs masses, the vacuum expectation values ratio $\tan\beta$, and the mixing angle α of the neutral scalar sector. The square sum of the vacuum expectation values is fixed by the W mass and weak coupling constant:

$$v_1^2 + v_2^2 = \frac{2m_\mathrm{W}^2}{g^2} = (246\,\mathrm{GeV})^2/2. \tag{2.13}$$

For phenomenological studies it is convenient to reduce the number of free parameters by picking a more specific model with additional constraints. There are basically two major constraints. First, it is an experimental fact that $\rho = m_\mathrm{W}^2/(m_\mathrm{Z}^2 \cos\theta_\mathrm{W})$ is very close to 1 [32]. The requirement that $\rho = 1$ for arbitrary values of a non-minimal Higgs potential $\Phi(T, Y)$ was found to be [33]

$$(2T + 1)^2 - 3Y^2 = 1, \tag{2.14}$$

where T and Y specify the total $SU(2)_L$ isospin and hypercharge of the particular representation of the Higgs field. The possibilities beyond $T = 1/2, Y = \pm 1$ are usually discarded because the representations become too complicated. The second major theoretical constraint on possible

Higgs models comes from severe limits on the existence of flavour changing neutral currents. In minimal Higgs model incorporated in the Standard Model, tree level flavour changing neutral currents are automatically absent, because the same operations that diagonalize the mass matrix also diagonalize the Higgs-fermion couplings. In general, this is no longer the case in non-minimal Higgs models, but was shown to be true in a special case when all fermions of a given electric charge couple to no more than one Higgs doublet [34].

One of the models that satisfies these requirements is the Minimal Supersymmetric Standard Model (MSSM). It is a special case of a general two Higgs doublet model where the two doublets of Higgs fields come with opposite hypercharge. The $Y = -1$ doublet couples only to down type quarks and leptons and $Y = 1$ doublet couples only to the up type ones. Such a choice provides masses for all quarks and leptons and at the same time prevents the existence of flavour changing neutral currents in the tree level. Vacuum expectation values v_2 and v_1 from eq. (2.9) correspond to up and down type quarks and leptons, respectively. In MSSM masses of charged Higgs bosons are expected to be of the order $m_{H^\pm}^2 = m_W^2 + m_A^2$, that is larger than m_W. Discovery of such heavy objects at current LEP centre-of-mass energies would be rather difficult. However, in a general two Higgs doublet model existence of light charged Higgs bosons can not be ruled out and their discovery would unambiguously signal the existence of an extended Higgs sector.

The goal of the present Higgs searches in general is, if not to find the Higgs boson altogether, at least to set upper limits on the cross-sections of the reactions that are believed to take place. In the framework of a specific Higgs model, these searches try to narrow the area of the unexplored parameter space where a Higgs boson could exist. This is the common effort of most of the experimental physicists today.

Primary goal of the present work is to investigate production and decays of the charged Higgs bosons in electron positron collisions. This work will focus on the charged Higgs bosons only; the neutral Higgs bosons of the two Higgs doublet model (equations 2.11, 2.12) appear for the sake of completeness of the model presentation and will not be investigated into any further throughout this work.

2.3 Production and decays of charged Higgs bosons at LEP

The production of charged Higgs bosons

$$e^+e^- \rightarrow H^+H^- \tag{2.15}$$

is built up by s-channel γ and Z^0 exchanges (figure 2.1).

Taking into account only tree level Feynman diagrams, the cross section for the reaction depends only on the charged Higgs boson mass m_H and the centre of mass energy $\sqrt{s}$ of the
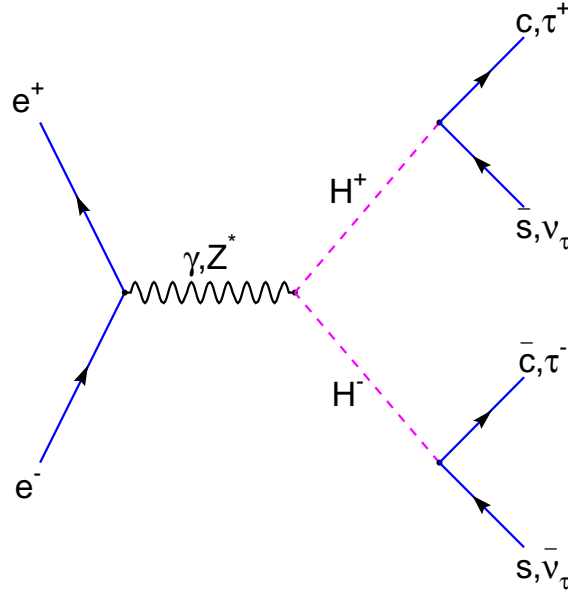
Figure 2.1: Tree level production and dominant decay diagrams for charged Higgs bosons in the framework of the two doublet Higgs model.

colliding electron and positron [35],

$$\sigma(\mathrm{e^+e^-} \to \mathrm{H^+H^-}) = \frac{2G_F^2 m_{\mathrm{W}}^4 s_{\mathrm{W}}^4}{3\pi s}\left[1 + \frac{2\hat{v}_{\mathrm{e}}\hat{v}_{\mathrm{H}}}{1 - m_{\mathrm{Z}}^2/s} + \frac{(\hat{a}_{\mathrm{e}}^2 + \hat{v}_{\mathrm{e}}^2)\hat{v}_{\mathrm{H}}^2}{(1 - m_{\mathrm{Z}}^2/s)^2}\right]\beta_{\mathrm{H}}^3. \tag{2.16}$$

Other factors in the equation (2.16) are well known from various measurements [32]. The rescaled $\mathrm{Z^0}$ charges are defined by $\hat{a}_e = -1/4c_W s_W$, $\hat{v}_e = (-1 + 4s_W^2)/4c_W s_W$ and $\hat{v}_H = (-1 + 2s_W^2)/2c_W s_W$, where s_W and c_W are the sine and the cosine of the Weinberg angle. Factor $\beta_H = (1 - 4m_{\mathrm{H^\pm}}^2/s)^{1/2}$ is velocity of the produced Higgs particles.

Since we want to take into account not only the tree level Feynman diagrams but also higher order corrections, the reaction (2.15) was simulated by the PYTHIA 5.7 [36] event generator that includes higher order and initial state radiation (ISR) corrections. Cross sections computed by PYTHIA for three different centre of mass energies are shown in figure 2.2 and summarised in table 2.1.

Partial widths for charged Higgs boson decays into quarks are obtained from

$$\Gamma(\mathrm{H^\pm} \to \mathrm{U\bar{D}}) = \frac{3\mathrm{G_F}\,m_{\mathrm{H^\pm}}}{4\sqrt{2}\pi}\,|V_{\mathrm{UD}}|^2\left[m_{\mathrm{U}}^2\cot^2\beta + m_{\mathrm{D}}^2\tan^2\beta\right]\left[1 + \frac{17}{3}\frac{\alpha_s}{\pi}\right], \tag{2.17}$$

U being an up-like and D a down-like quark. An analogous expression can be written for decay into leptons. Taking into account zero neutrino masses and omitting the mixing between quark
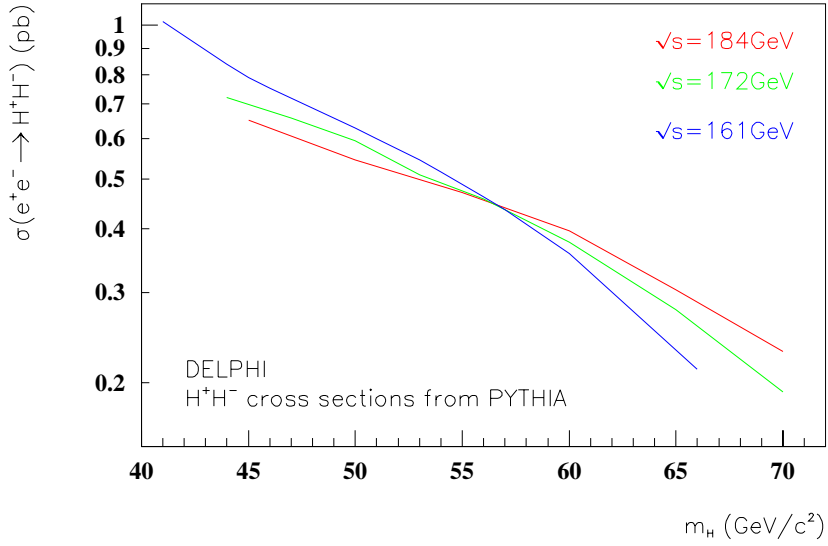
Figure 2.2: Cross section for the reaction $e^+e^- \to H^+H^-$ as generated by PYTHIA 5.7 event generator for three different centre of mass energies. Initial state radiation contributions have been taken into account.

$m_{H^\pm}$ $[\,\mathrm{GeV}/c^2]$	Cross section at $\sqrt{s} = 172\,\mathrm{GeV}$ [pb]	Cross section at $\sqrt{s} = 184\,\mathrm{GeV}$ [pb]
45	0.720	0.651
50	0.593	0.545
55	0.457	0.470
60	0.376	0.396
65	0.277	0.304
70	0.192	0.230

Table 2.1: Cross-sections for the reaction $e^+e^- \to H^+H^-$ as generated by the PYTHIA 5.7 [36] event generator at different values of $m_{H^\pm}$ for the centre of mass energies of 172 and 184 GeV.

families we get

$$\Gamma(H^\pm \to l\bar{\nu}_l) \propto G_F \, m_{H^\pm} \, m_l^2 \tan^2\beta\,. \tag{2.18}$$

Charged Higgs bosons are expected to decay predominantly into the heaviest kinematically accessible fermion pair provided it is not suppressed by a small Cabibbo-Kobayashi-Maskawa [37] matrix element, i.e. $H^+ \to \tau^+\nu_\tau$ or $c\bar{s}$. The expected final states are therefore $\tau^+\nu_\tau\tau^-\bar{\nu}_\tau$, $c\bar{s}\tau\bar{\nu}_\tau$ and $c\bar{s}\bar{c}s$. Which of the final states will actually prevail now depends on the parameter $\tan\beta$, ratio of the vacuum expectation values of the Higgs fields in a two doublet Higgs model (equation 2.10). Since the value of $\tan\beta$ is unknown, it is necessary to investigate the entire $\tan\beta$ parameter space.

In the case of $\tan\beta \gg 1$ the dominant decay is

$$\mathrm{H^+H^-} \rightarrow \tau^+ \nu_\tau \tau^- \bar{\nu}_\tau. \qquad (2.19)$$

Mass of the τ lepton is approximately ten times larger than mass of the s-quark and the first term in eq. (2.17) is suppressed as $\cot^2\beta$ in the case of quarks, so $\mathrm{H^\pm}$ decay predominantly into leptons. Dependence of the $\mathrm{Br}(\mathrm{H^+} \rightarrow \tau^+\nu_\tau)$ on $\tan\beta$ is shown in figure 2.3. In the following sections this decay will be referred to as the leptonic channel.
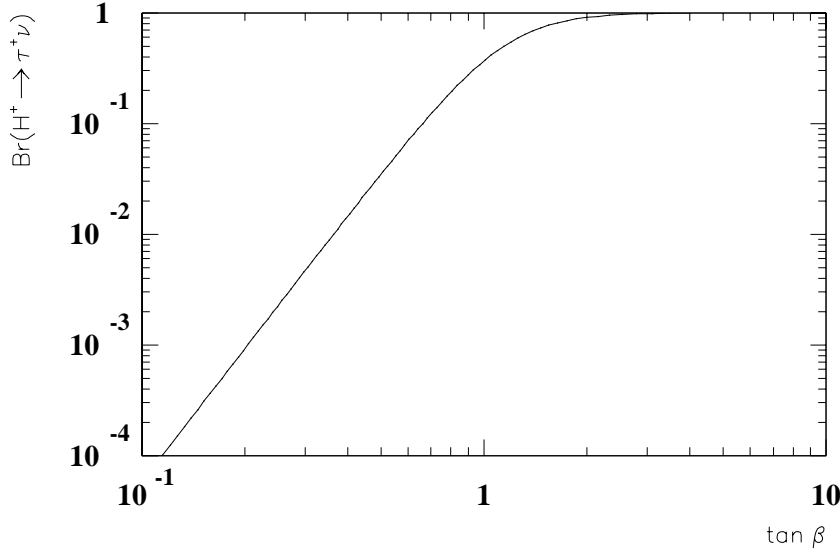

Figure 2.3: The branching ratio for $\mathrm{H^+} \rightarrow \tau^+\nu_\tau$ as a function of $\tan\beta$ [33].

For $\tan\beta \ll 1$ the dominant decay is

$$\mathrm{H^+H^-} \rightarrow \mathrm{c\bar{s}\bar{c}s}. \qquad (2.20)$$

Here the decay width into leptons is low due to $\tan^2\beta$ suppression in equation 2.18. In the following sections this decay will be referred to as the hadronic channel.

For $\tan\beta \approx 1$, branching ratios for both $\mathrm{H^+} \rightarrow \tau^+\nu_\tau$ and $\mathrm{H^+} \rightarrow \mathrm{c\bar{s}}$ are around 0.5 (figure 2.3). In this case, about half of the final states are expected to be $c\bar{s}\tau\bar{\nu}_\tau$,

$$\mathrm{H^+H^-} \rightarrow c\bar{s}\tau\bar{\nu}_\tau. \qquad (2.21)$$

In the following sections this decay will be referred to as the mixed channel.

2.4 Properties of the charged Higgs boson decays and comparison to the major background processes

From the comparison of the expected production cross-sections of the looked-for Higgs bosons (signal) to cross-sections of other reactions (background) summarised in table 2.2 the extraction

of the Higgs signal seems a very hard task. Properties of most important background processes that enable efficient signal-background separation are presented in the following paragraphs. Distributions of the of the kinematical observables are presented without any preselection and are normalised to production cross sections for the specific background reactions.

Reaction	Cross section at $172\,\mathrm{GeV}$ [pb]	Cross section at $184\,\mathrm{GeV}$ [pb]
$e^+e^- \to W^+W^-$	12.28	15.44
$e^+e^- \to We\nu$	0.48	0.60
$e^+e^- \to Z^0Z^0$	1.15	1.34
$e^+e^- \to Z^0\gamma,\ Z^0 \to q\bar{q}$	121	100.4
$e^+e^- \to Z^0\gamma,\ Z^0 \to \mu^+\mu^-$	9.8	9.9
$e^+e^- \to Z^0\gamma,\ Z^0 \to \tau^+\tau^-$	9.5	8.7
$e^+e^- \to e^+e^-\gamma$	63.9	56
$e^+e^- \to e^+e^-$	1442	1260
$e^+e^- \to \gamma\gamma$	12.05	11.5

Table 2.2: Types of background taken into account in the analysis and their corresponding cross sections for the centre of mass energies of 172 and $184\,\mathrm{GeV}$.

Signal events in the hadronic channel are expected to have four nicely separated jets from the quark fragmentation (figure 2.4 top). Total energy of the reconstructed decay products is expected to be close to the centre of mass energy of the colliding electron and positron. Main sources of background in this channel are QCD processes $e^+e^- \to q\bar{q}(\gamma)$ and decays of W bosons $e^+e^- \to W^+W^-, W \to q\bar{q}$.

In case of the reaction $e^+e^- \to Z^0\gamma$, a photon is radiated from the initial e^+ or e^- at very small polar angles and jets are not well separated. In $e^+e^- \to q\bar{q}$ case the quarks fragment into two back to back hadronic jets in the centre of mass inertial frame. This two processes can be efficiently suppressed for example by a cut on sphericity and centre of mass energy of e^+ and e^- after the photon is radiated (figure 2.5 top and centre).
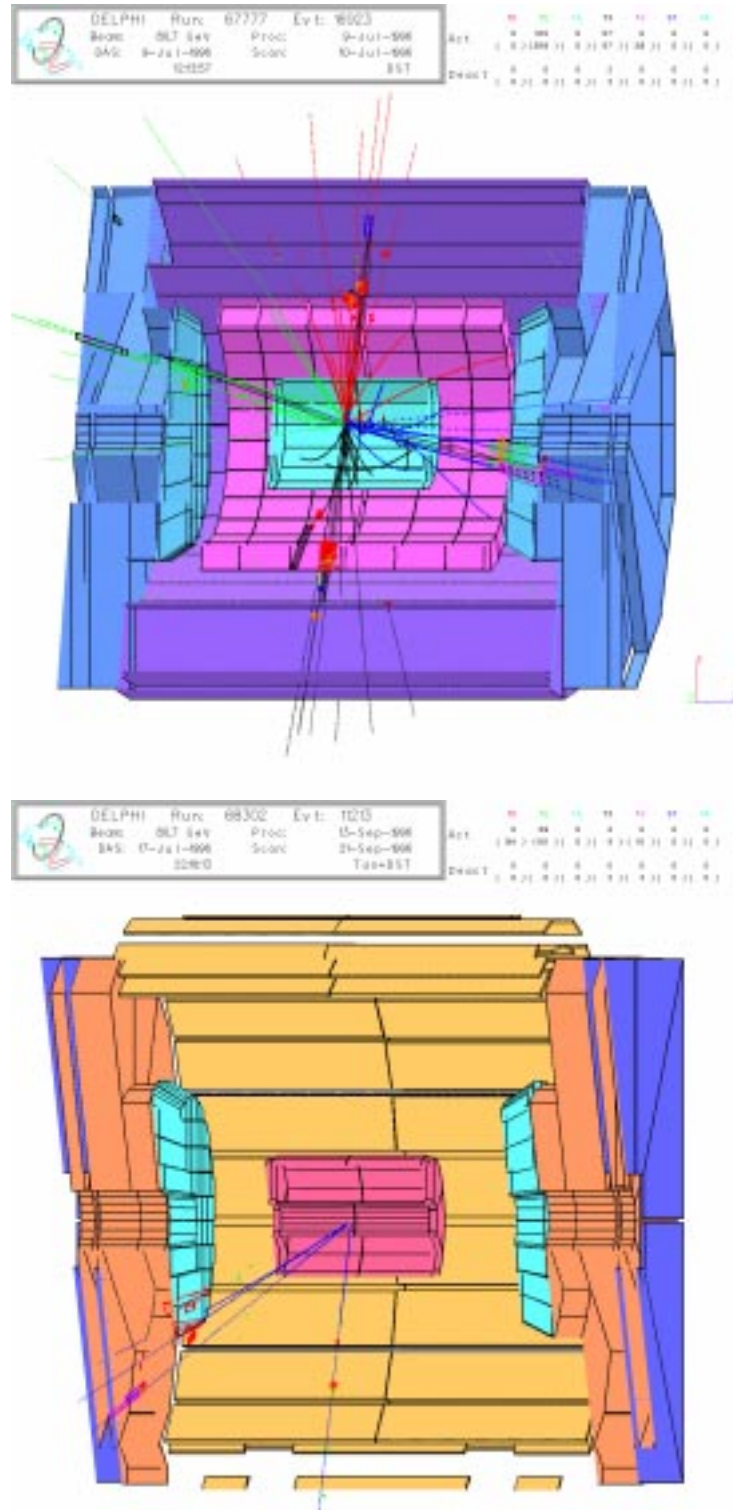
Figure 2.4: Top: example of an event with four nicely separated hadronic jets collected at centre-of-mass energy of $161\,\mathrm{GeV}$ by the DELPHI spectrometer. This event is a $\mathrm{W}^+\mathrm{W}^-$ decay candidate, very similar in topology to charged Higgs boson hadronic decay. Bottom: example of a collected $\mathrm{W}^+\mathrm{W}^- \rightarrow \mu\nu_\mu\tau\nu_\tau$ decay candidate. Topology of this event is similar to a situation in a leptonic Higgs boson decay.

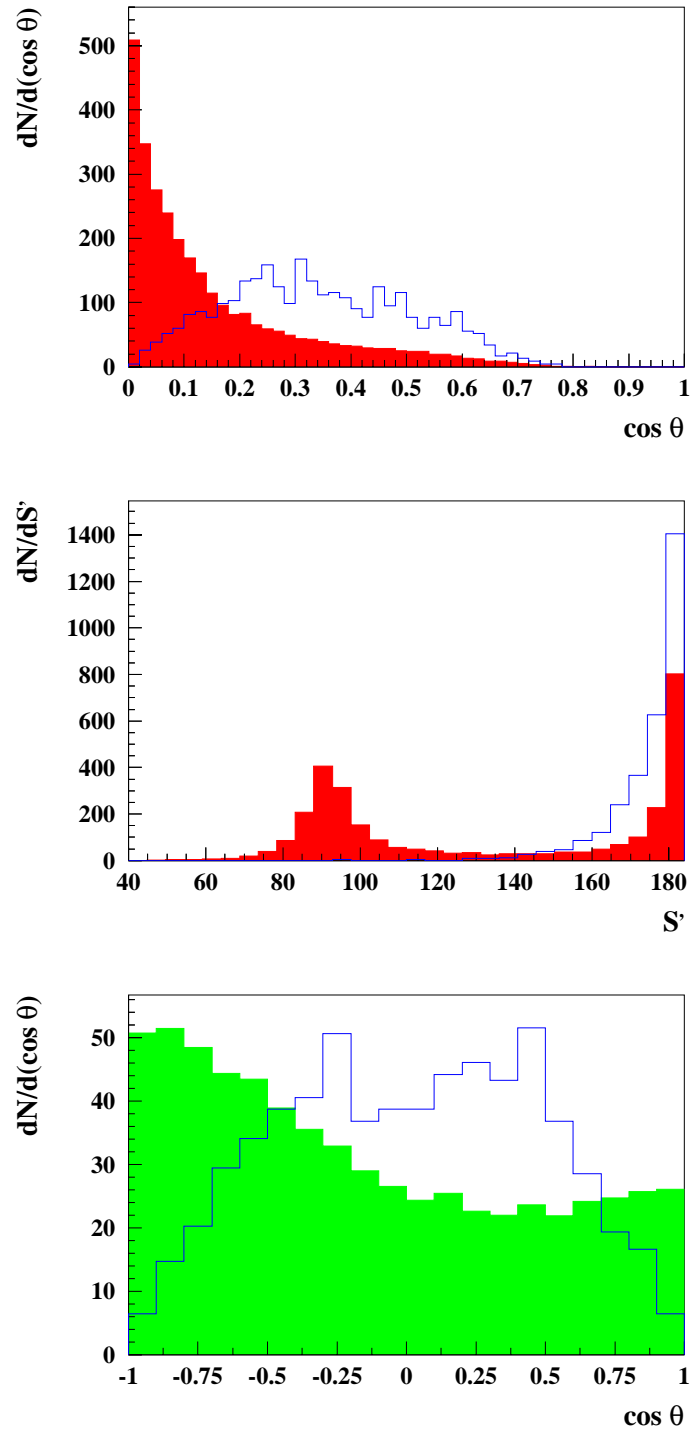**Figure 2.5:** Hadronic channel: distribution of event sphericity (top), effective centre-of-mass energy $s\prime$ after initial state radiation (centre) and cosine of the angle between the reconstructed dijet and z-axis (bottom). Simulated $q\bar{q}(\gamma)$ background is represented by full red histogram, simulated W^+W^- background by full green histogram and signal by open blue histogram. For easier visual comparison, signal was rescaled to the number of events in the background.

Sphericity is defined in eq. (3.4) of the next chapter and describes topological properties of an event. Remaining production of W bosons and their decays into quark pairs are on the other hand hard to suppress since the event topology is very similar to the one of the signal. Difference in angular distributions due to polarisation of W bosons along their momenta (figure 2.5 bottom) allows for some background rejection. However, especially in the case when expected mass of the charged Higgs bosons is close to the W boson mass, this background becomes almost irreducible.

In the mixed channel one of the charged Higgs bosons decays into a $c\bar{s}$ quark pair, while the other decays into $\tau\bar{\nu}$. Such an event is characterised by two hadronic jets and a τ candidate, as well as by missing energy taken by the neutrinos. One of the dominating background processes is $e^+e^- \to q\bar{q}(\gamma)$, which can be suppressed because of different missing momentum distribution with respect to the signal (figure 2.6 top and centre). Due to the conservation of momentum, sum of the momenta of all particles originating in an e^+e^- collision has to be zero. However, sum of the momenta of detected particles in an event is generally not zero because some particles escape unobserved from the detector. Missing momentum of the event is thus defined as negative sum of the momenta of all detected particles, $\vec{p}_{miss} = -\sum_i \vec{p}_i$. The other most important background represent decays of W boson pairs into $c\bar{s}\tau\bar{\nu}_\tau$, which can be rejected by placing a cut on effective centre of mass energy (figure 2.6 bottom).

In the leptonic channel both charged Higgses decay into a $\tau\nu$ pair. These events are characterised by low particle multiplicity and large missing energy. Unlike the other two channels, reconstruction of the Higgs boson masses is not possible because of too many unknowns due to the numerous missing energy sources. The two τ leptons decay into narrow jets or into a pair of muons or electrons (figure 2.4 bottom). In any of the cases missing energy is carried away by at least four undetected neutrinos. The most abundant background processes are two photon reactions $e^+e^- \to \gamma\gamma$, but they can be efficiently rejected by a cut on missing transverse momentum (figure 2.7 top). Transverse momentum is defined as the momentum component perpendicular to the beam axis, $\sum_i |\vec{p}_i \cdot \hat{z}|$. Bhabha scattering (electrons and positrons from $e^+e^- \to e^+e^-$ flying mainly in the forwardbackward direction) is rejected by discarding events with large deposited energy in a cone around the beam pipe (figure 2.7 centre). Most difficult to reject is again W^+W^- background. An example distribution (momentum of the most energetic lepton) that provides good separation is shown in figure 2.7 (bottom).

To be able to separate Higgs boson decays from background reactions in each of the three channels several kinematical properties were combined into a separator that provides good rejection of all types of background. Choice of the kinematical observables depends on the particular decay channel, so kinematical distributions for each channel were looked into separately. A detailed description can be found in the next chapter.
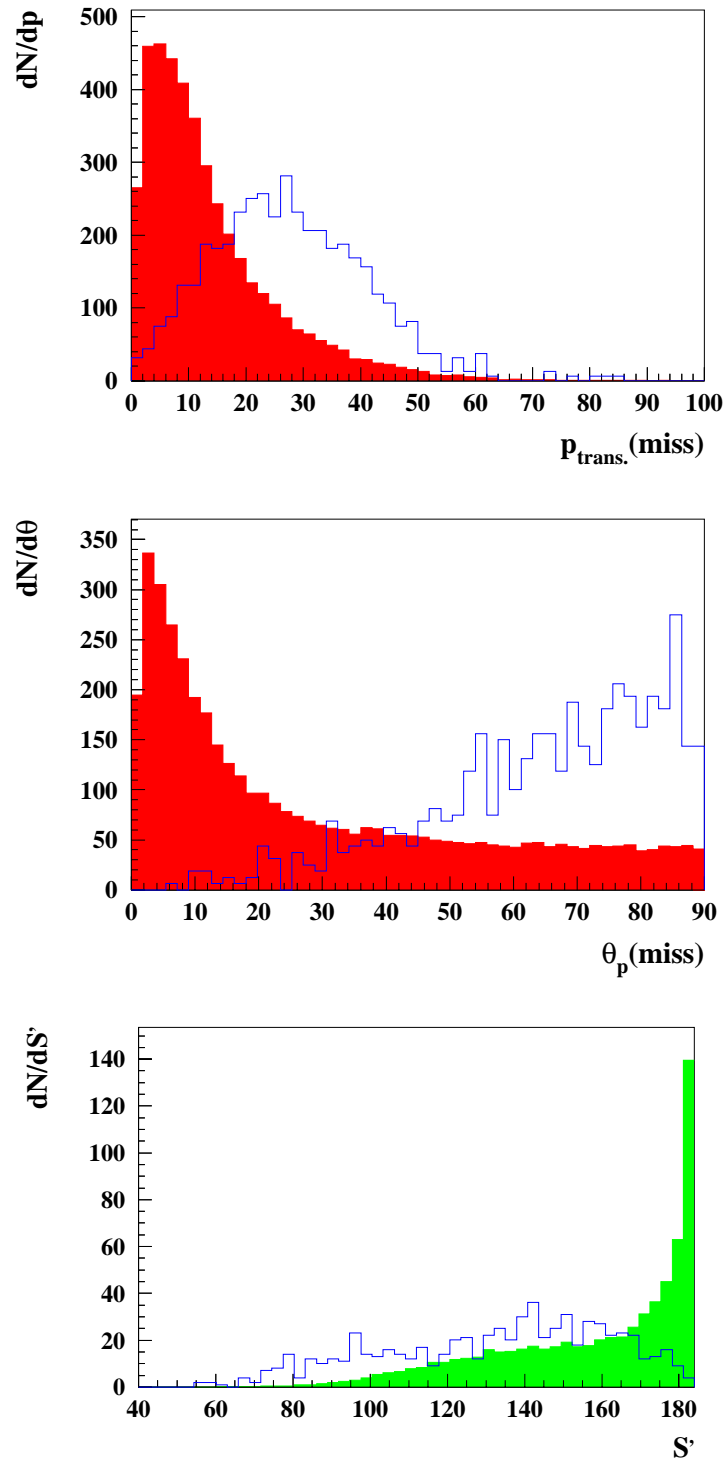
Figure 2.6: Top and centre: distribution of missing transverse momentum and angle of the missing momentum. Simulated $q\bar{q}(\gamma)$ background is represented by full red histogram. Bottom: distribution of the effective centre-of-mass energy $s\prime$ after initial state radiation. Simulated W^+W^- background is represented by full green histogram. In all cases signal was rescaled to the number of events in the background and drawn as open blue histogram.
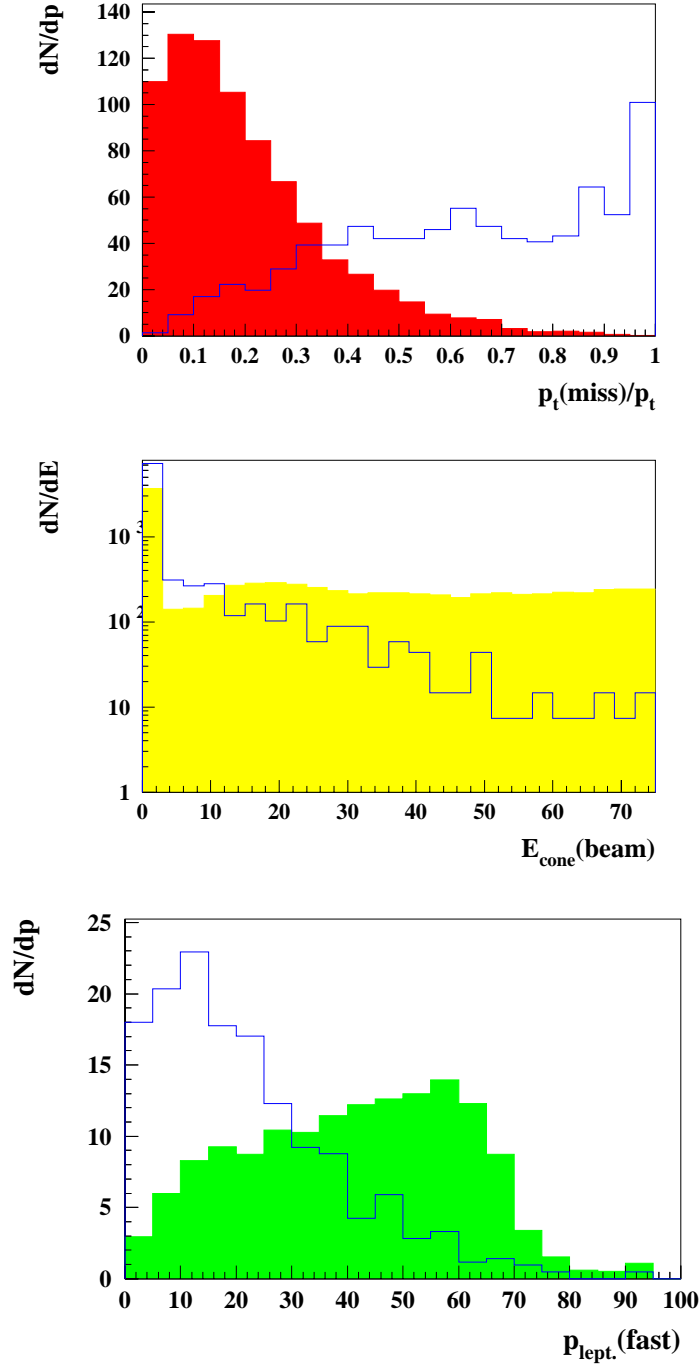
Figure 2.7: Leptonic channel: Distribution of missing transverse momentum for the two photon background (top), polar angle of the most energetic lepton times its charge (centre) and momentum of the most energetic lepton in event (bottom). Simulated $qq(\gamma)$ background is represented by full red histogram, B-habha scattering by full yellow histogram and W^+W^- background by full green histogram. In all cases signal was rescaled to the number of events in the background and drawn as open blue histogram.

3

Data Selection and Background Estimation

This chapter describes selection of the data sample and determination of the remaining background. Data collected by the DELPHI spectrometer was first processed by DELANA [38], the main DELPHI software for raw data event processing. This includes data decoding, pattern recognition, track reconstruction and tagging of basic types of events. Processed events were accepted for further analysis if they satisfied track and event preselection criteria described in the next section. According to the event topology, accepted events were then arranged in three classes: hadronic, mixed and leptonic. In all three cases we used WWANA [39], the standard DELPHI package for four jet and W-analyses. Separation of signal from background was optimised for each of the three classes separately. A number of kinematical observables offering good separation between signal and background was chosen for each class and combined into final probability for the signal. This probability with a cut at maximal efficiency times purity for the signal was used as the final separator for event selection.

3.1 Track and Event Preselection

Analysed data were collected by the DELPHI spectrometer at an average e^+e^- centre-of-mass energy of $\sqrt{s} = 184\,\mathrm{GeV}$. They correspond to an integrated luminosity of $L = 53.9\,\mathrm{pb}^{-1}$.

In an event, charged particles were selected within a polar angle between $10°$ and $170°$ and with a momentum between $0.4\,\mathrm{GeV}/c$ and the beam momentum. In addition, the length of the reconstructed tracks had to be larger than 15 cm, their impact parameters, both longitudinal and transverse with respect to the beam axis, should not exceed 4 cm, and the maximum allowed uncertainty on the momentum measurement was 100%. Neutral particles were accepted if they deposited more than $0.5\,\mathrm{GeV}$ energy in the electro-magnetic or hadronic calorimeters.

For each event all selected particles were clustered into jets using the LUCLUS [36] algorithm. To accept a particle in a jet, a maximum distance $d_{ij} = 6.5$ GeV/c between the particle

and the jet was allowed. Distance d_{ij} is defined as a normalised cross-product

$$d_{ij} \sim \frac{|\vec{p}_i \times \vec{p}_j|}{|\vec{p}_i + \vec{p}_j|} \tag{3.1}$$

of the particle momentum $\vec{p}_i$ and the momentum of the jet $\vec{p}_j$.

Events were arranged in three classes. For fully hadronic decays, where both H^+ and H^- decayed into quarks, the expected event topology was four hadronic jets. In mixed decays one of the two Higgs bosons decayed into a tau lepton and a tau neutrino, such an event being characterised by two hadronic jets and a tau candidate. In leptonic decays both of the Higgs bosons decayed into a tau lepton and a tau neutrino. In about 65% of all cases, tau leptons decay into pions and another tau neutrino, thus producing two narrow acollinear jets. In other 35% of cases tau leptons decay into electrons or muons. Event preselection criteria were applied in each of the three cases separately.

For the $H^+H^- \rightarrow q_1\bar{q}_2 q_3\bar{q}_4$ candidates, particles were forced into a four-jet configuration and, in order to improve the momentum and energy resolution, a kinematically constrained fit was performed [40], imposing energy and momentum conservation and the equality of di-jet masses. Of the three possible pairings of the four jets (figure 3.1), the one which minimised the χ^2 of the fit was chosen. An event was required to have at least two charged tracks in each jet and maximum energy carried by a neutral particle was limited to $50\,\mathrm{GeV}$. Sphericity (equation 3.4) was required to be larger than 0.1 in order to reject a large part of hadronic background coming from $e^+e^- \rightarrow q\bar{q}$.
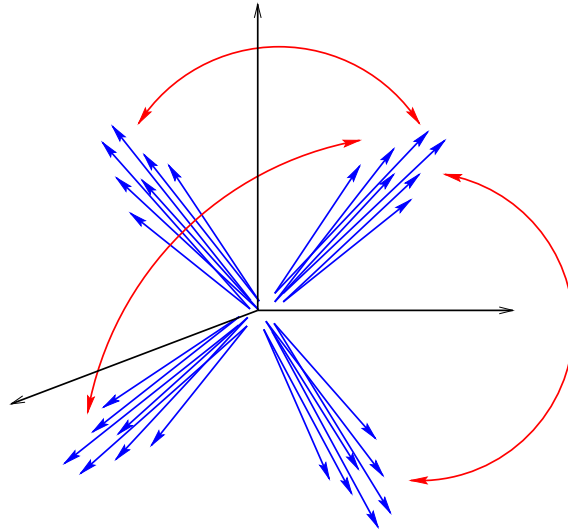

Figure 3.1: The three possible pairing combinations of the four hadronic jets in the $H^+H^- \rightarrow c\bar{s}\bar{c}s$ decay channel.

Events which were candidates for the mixed decays were forced into configurations with three jets. An event was required to have at least 5 charged tracks. In addition, at least one τ

candidate was required, identified as a narrow jet with multiplicity less than 9 and isolated from the rest of the event or a lepton with well defined charge.

In the case of candidates for fully leptonic decays, particles were forced into two jets. The preselection criteria for this channel required from 2 to 6 charged tracks in an event with total energy detected in the event not exceeding $0.55\sqrt{s}$ and total energy of the charged particles exceeding $0.04\sqrt{s}$. In order to reject Bhabha scattering, energy detected in cones with $30°$ half aperture around the beam axis had to be below $0.1\sqrt{s}$. Angle between the beam axis and either jet was required to be larger than $10°$. Jets in the leptonic Higgs boson decays are acollinear because of missing energy taken by the four undetected neutrinos. In order to reject events where the jets are back to back, and radiative return events with a photon along the beam pipe, the angle between the jets was required to be less than $160°$ and its projection on the plane perpendicular to the beam axis less than $175°$. Another useful quantity for the preselection is transverse acolinearity. It is calculated from angular distributions of the jets,

$$A_{\mathrm{tr}} = (\vec{p}_{j1} \times \vec{p}_{j2}) \cdot \vec{p}_{\mathrm{beam}}, \tag{3.2}$$

and is very useful for the suppression of the two photon background an the remaining Bhabha scattering with back to back photons and electrons. Expected value of the transverse acolinearity for this particular kind of background is close to one, with signal having a value less then one due to large missing energy taken by the neutrinos. In the preselection, transverse acolinearity had to be less than 0.75.

At this stage a single event could enter more than one of the three classes.

3.2   Simulation of Signal and Background Processes

Separation of signal from the background was optimised using computer generated $\mathrm{e^+e^-} \rightarrow \mathrm{H^+H^-}$ signal and background (table 2.2) reactions. Events were generated by the PYTHIA 5.7 [36] event generator which also includes initial state radiation (ISR) corrections. The fragmentation model incorporated in the simulation is tuned to the DELPHI data measured at LEP 1 [41]. These generated reactions are then propagated through the simulation of the detector by the detector simulation package DELSIM [42]. In this way one gets the signals from simulated detectors which are in the next step converted into distributions of physical observables by the same analysis programs [38] and in exactly the same way as the measured data. Charged Higgs signal samples were produced by PYTHIA generator [36] at five different $\mathrm{H^\pm}$ masses: $45\,\mathrm{GeV}/c^2$, $50\,\mathrm{GeV}/c^2$, $55\,\mathrm{GeV}/c^2$, $60\,\mathrm{GeV}/c^2$ and $65\,\mathrm{GeV}/c^2$. The QCD background samples were also produced by PYTHIA. Four fermion final states, including $\mathrm{W^+W^-}$ and $\mathrm{Z^0Z^0}$ backgrounds, were produced by the EXCALIBUR generator [43].

3.3 Hadronic channel

Main sources of background in the hadronic channel are the reactions $e^+e^- \rightarrow q\bar{q}(\gamma)$ and $e^+e^- \rightarrow W^+W^-$ as shown in the distribution of the effective centre-of-mass energy $s\prime$ after the initial state radiation (figure 3.2). To see the difference between signal and background distributions, number of signal events was rescaled to the number of background events in all figures in this chapter. Signal distributions were obtained from generated Higgs boson sample with $m_{H^\pm} = 60\,\mathrm{GeV}/c^2$. The variables for the separation were chosen as follows:
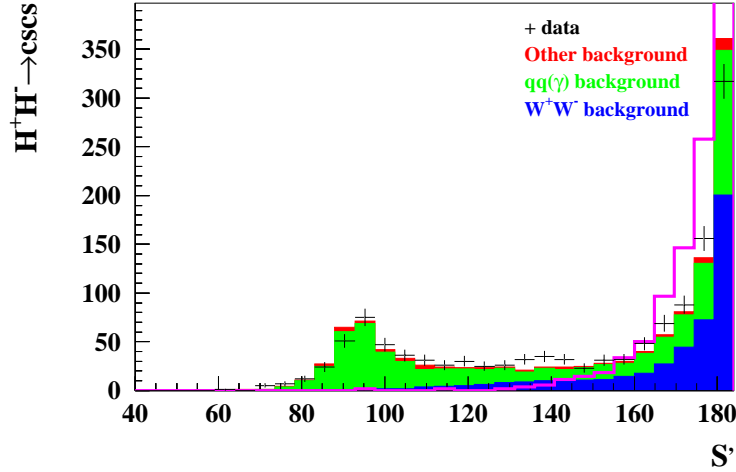
Figure 3.2: Distribution of the effective centre-of-mass energy $s\prime$ after initial state radiation in the hadronic channel after the preselection. Simulated $q\bar{q}(\gamma)$ background is blue, W^+W^- background green and the remaining background reactions are red. For easier visual comparison signal (purple open histogram) is rescaled to the number of events in total background.

- Tracks reconstructed by the DELPHI tracking detectors were clustered into jets using the LUCLUS [36] algorithm. Parameter d_{ij}, defined in equation 3.1 states the clustering rate. As a separating variable was taken D_{join}, i.e. the value of d_{ij} at the point where a three jet event becomes a four jet event. Its distribution can be seen in figure 3.3-1.

- Shape of an event can be presented by several variables calculated from momenta of the detected particles. One of them is called the event sphericity S. It is computed from the eigenvalues $Q_1 < Q_2 < Q_3$ of the normalised 3×3 sphericity tensor,

$$M^{\alpha\beta} = \frac{\sum_i p_i^\alpha p_i^\beta}{\sum_i p_i^2}. \tag{3.3}$$

Indices α and β denote the x, y and z components of the momentum of the i-th particle in the event. Unit eigenvector $\hat{n}_3$ is defined as the sphericity axis while $\hat{n}_1$ and $\hat{n}_2$ spawn the

sphericity plane. The event sphericity S is defined as a sum of the first two eigenvalues,

$$S(0 \leq S \leq 1) = \frac{3}{2}(Q_1 + Q_2).$$ (3.4)

In the preselection an additional cut on sphericity was performed discarding events with sphericity less than 0.1. This strongly reduced $q\bar{q}(\gamma)$ background peaking at 0. Distributions of sphericity in the hadronic channel can be seen in figure 3.3-2. A related variable describing event shape is called aplanarity. It is defined as

$$A(0 \leq A \leq \frac{1}{2}) = \frac{3}{2}Q_1,$$ (3.5)

Q_1 being the smallest eigenvalue of the sphericity tensor defined in equation 3.3. Aplanarity is typically non-zero only in a case of many jets. Aplanarity was used as a separating variable in the leptonic channel.

- Angle between the faster jets from each of the two chosen di-jets (fig. 3.3-3), jet multiplicities (fig. 3.3-4) and the effective centre-of-mass energy after initial state radiation (fig. 3.4-5) were also used as separating quantities. The latter was estimated either from the energy of an isolated highly energetic photon, if such a photon was reconstructed in the detector, or by taking the photon direction to be parallel to the beam and assuming a two-jet topology for the rest of the event [44]. The discriminating power of these variables stems from the fact that the dominant background, coming from $q\bar{q}$ creation in e^+e^- collisions, is frequently accompanied by a photon radiated from the initial state, resulting in a smaller effective centre of mass energy.

Jets from $H^\pm$ pair decays are also distributed more uniformly in space than jets from $q\bar{q}(\gamma)$ events, where two out of four reconstructed jets are expected to arise from fragmentation of gluons, radiated predominantly at small angles with regard to the quark directions. At the same time, these gluon jets are on average less energetic than jets in hadronic W decays. For this reason two variables were constructed. The first one is defined as

$$D = \frac{E_{\min} \cdot \theta_{\min}}{E_{\max}(E_{\max} - E_{\min})}$$ (3.6)

where $\theta_{\min}$ is the angle between two closest hadronic jets, $E_{\min}$ is the minimal and $E_{\max}$ the maximal jet energy. The second one is a product of the momentum ratios of the jets with smaller momentum over jets with larger momentum in the two di-jet combinations,

$$DR = \left[\frac{p_1^{slow}}{p_1^{fast}}\right]_{1.dijet} \left[\frac{p_2^{slow}}{p_2^{fast}}\right]_{2.dijet}.$$ (3.7)

Their distributions are presented in figures 3.4-7 and 3.4-8.

- Important properties of the hadronic H^+H^- decays that help eliminating W^+W^- background are special shapes of angular distributions of reconstructed boson momenta with respect to the z axis and angular distributions of jets with respect to the corresponding boson. The two constructed observables, $\cos\vartheta_{\mathrm{boson}}$ and $\vartheta_{\mathrm{jet-boson1}} \cdot \vartheta_{\mathrm{jet-boson2}}$ are presented in figures 3.4-6 and 3.4-9). In the case of the $W^{\pm}$ bosons, the direction of the jet is correlated to the charge of its primary quark since W^+'s produced in e^+e^- collisions are polarised predominantly along their momenta and W^-'s in the opposite direction. Because of the $V-A$ structure of the W-decays, down-like quarks and anti-quarks will fly mainly along the momentum of the parent $W^{\pm}$. Since $H^{\pm}$ are scalar particles, there are no such $H^{\pm}$ polarisation effects in $e^+e^- \to H^+H^-$ decays.
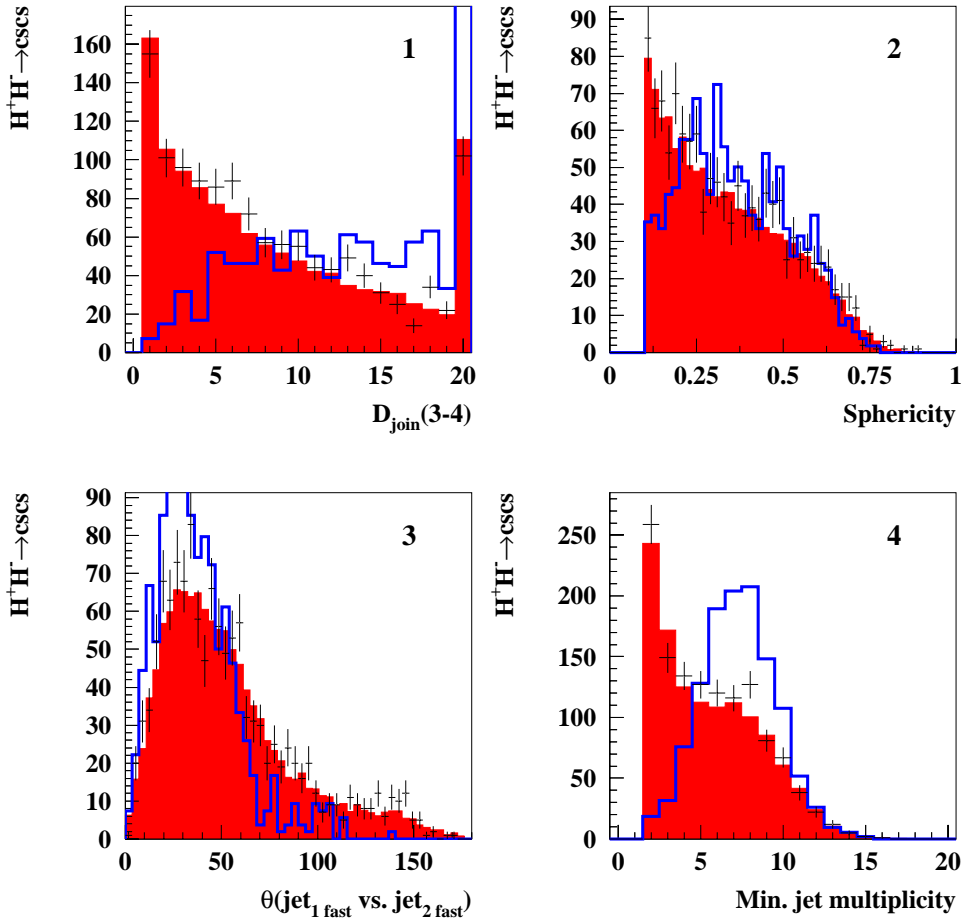

Figure 3.3: Distributions of the observables used for separation of $H^+H^- \to c\bar{s}\bar{c}s$ from the background. Measured data are drawn with error bars, signal is represented by light blue histogram and the background by full red histogram. The signal is rescaled to the full background for easier visual comparison. Different types of background in the background distribution are rescaled to their corresponding generated cross sections.
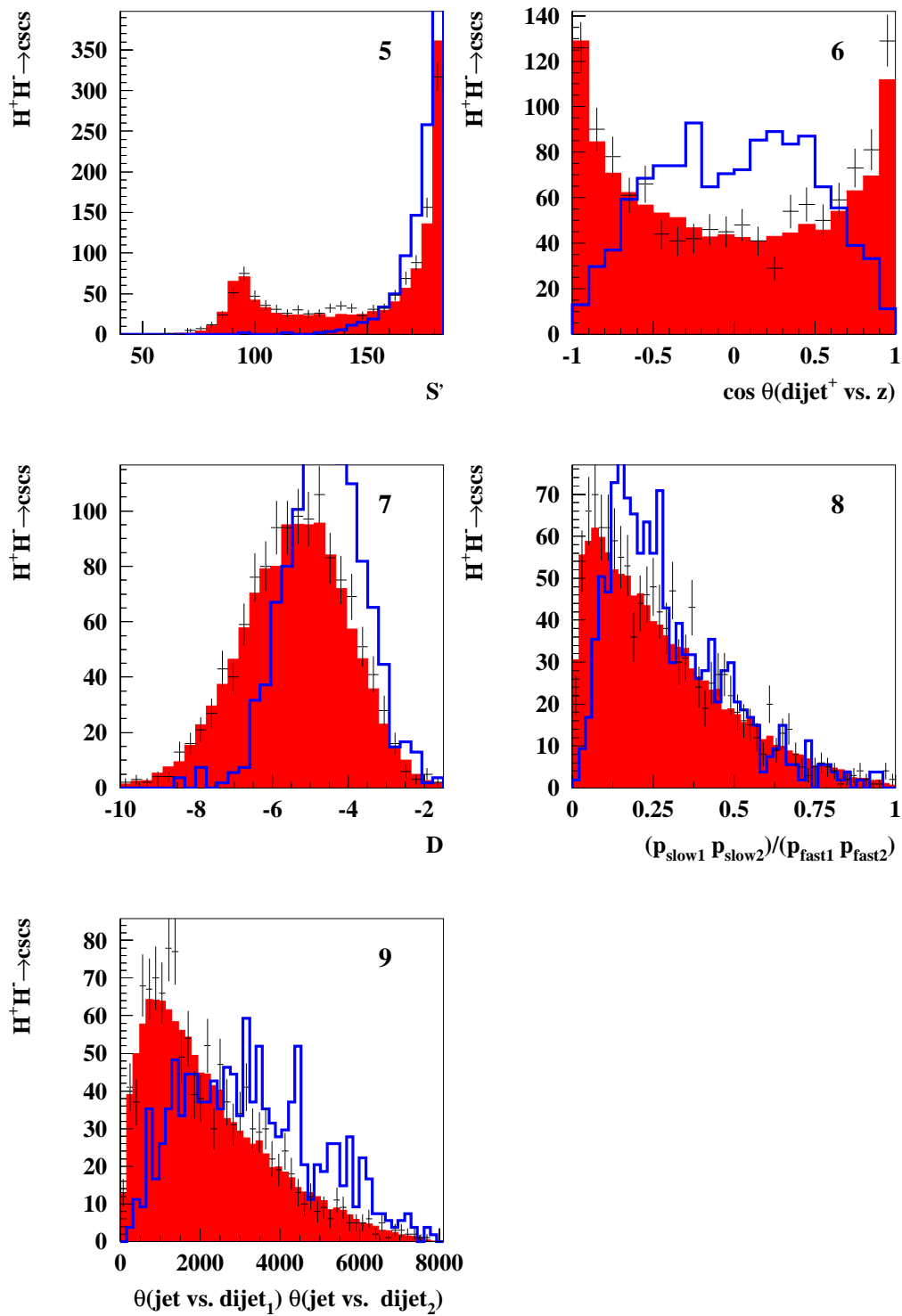
Figure 3.4: Distributions of the observables used for separation of $H^+H^- \to c\bar{s}\bar{c}s$ from the background. Fig. 3.3 Cont'd.

In the hadronic and the mixed channel additional information about the Higgs boson decays can be obtained by tagging the flavour of hadronic jets arising from fragmentation of the primary quarks in $H^{\pm}$ decays. The following discriminating properties have been used:

- Jets from primary b- or c-quarks can be distinguished from the s-, u- and d-jets by the finite lifetime of hadrons, containing b- or c-quarks [45]. Namely, the finite lifetime of the b- and c-quarks reflect in the impact parameters of their decay products with respect to the primary vertex. They tend to be larger than impact parameters of particles in s-, u- and d-jets. In other words, the probability that all particles originate from the reconstructed primary vertex would be lower for c-quark jets and still lower for the b-quark jets. These properties were used for construction of tagging methods for heavy quark jets [45]. To obtain better tagging efficiency, other variables such as effective mass of particles included in the secondary vertex were also included in the so called combined b-tagging method. In our analysis the AABTAG package [46] based on this method was used for tagging of c-quark jets. Distribution of the combined tagging variable is shown in figure 3.5.
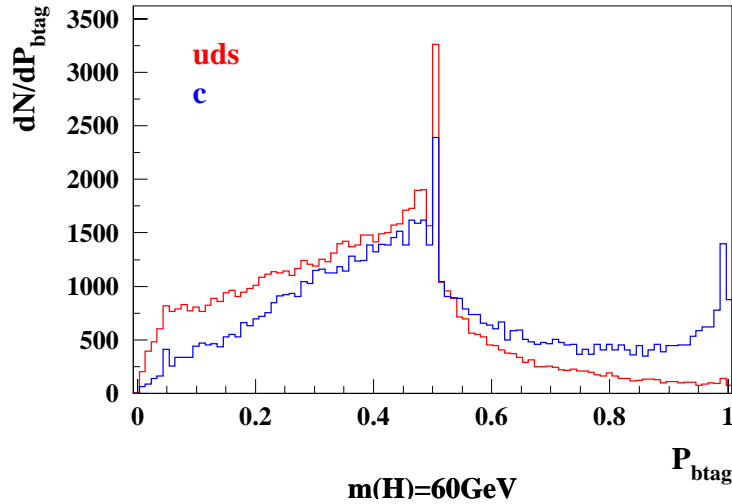

Figure 3.5: Distributions of the combined lifetime tag probability for jets originating from c and s flavoured quarks in the simulated events.

- c- and s-jets can be tagged by the high momentum charged kaons, detected in the system of DELPHI RICH counters. These kaons are very likely to contain a primary s-quark or an s-quark from a $c \rightarrow s$ decay. A schematic diagram of such a decay is shown in figure 3.6. Figure 3.7-a shows the expected charged kaon spectra for jets with c-, s-, u- and d- flavour, respectively. In the same way, if the leading particle in a hadronic jet is an identified pion it is an indication for an u- or d-jet (see Fig. 3.7-b for illustration). The

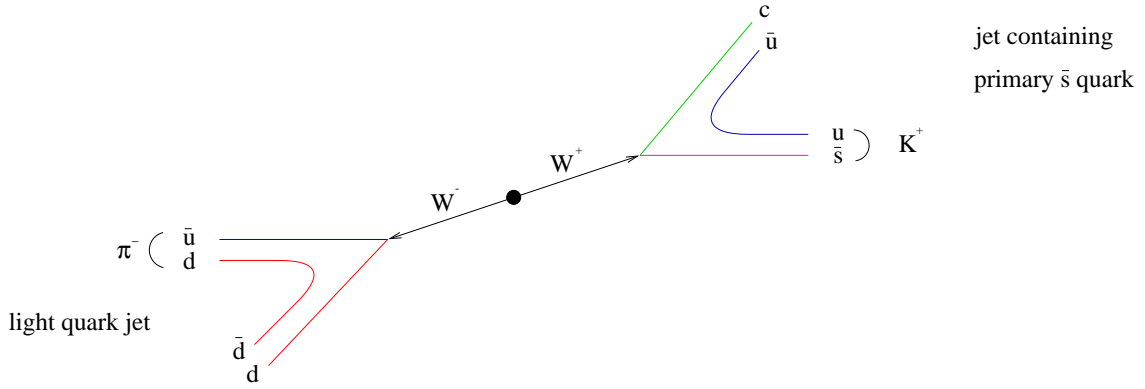number of entries in figures 3.7-a and b corresponds to approximately 15000 generated W^+W^- events.

Figure 3.6: Schematic diagram of K and π production in $W^{\pm}$ decays.
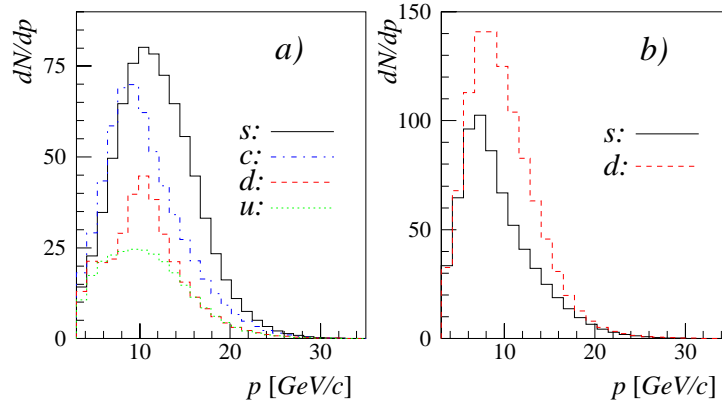

Figure 3.7: K, π identification - momentum of simulated leading charged kaons a) and pions b) in c, s, u and d jets.

Taking into account b-tagging and particle identification information a di-jet probability P_{cs} was calculated. Mean of the distribution of P_{cs} for di-jets consisting of c and s jets was closer to 1 than for other flavour combinations. In the hadronic channel, the P_{cs} probabilities for both di-jets were used to obtain P_{cscs} probability for the event. A sample distribution of P_{cscs} for Higgs boson signal generated at $m_H = 60\,\mathrm{GeV}$ is shown in figure 3.8. In the mixed channel we can only make use of a single di-jet P_{cs} probability.
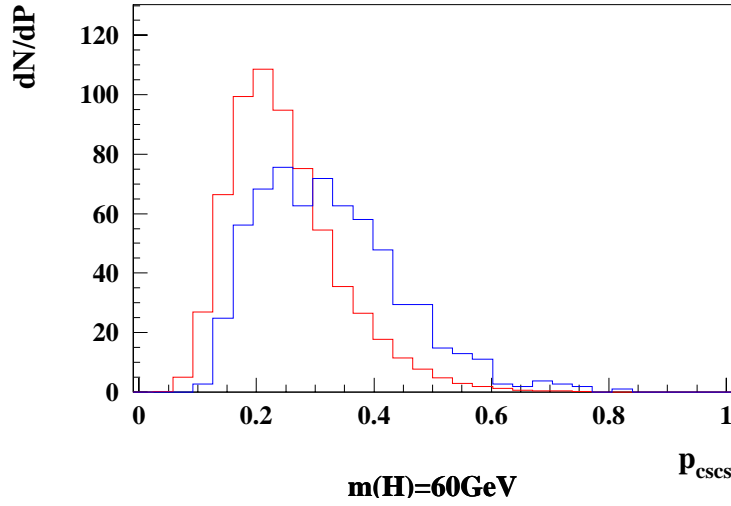
Figure 3.8: Distribution of the P_{cscs} separator for the hadronic channel. H^+H^- signal distribution represented by blue and background distribution by red histogram. Signal histogram has been rescaled to number of entries in background for easier comparison.

3.4 Mixed channel

Background in the mixed channel is similar as in the hadronic channel. Contributions of different background reactions to a sample kinematical distribution - angle between the two hadronic jets - is shown in figure 3.9. Mixed H^+H^- decays were selected using the following set of variables:
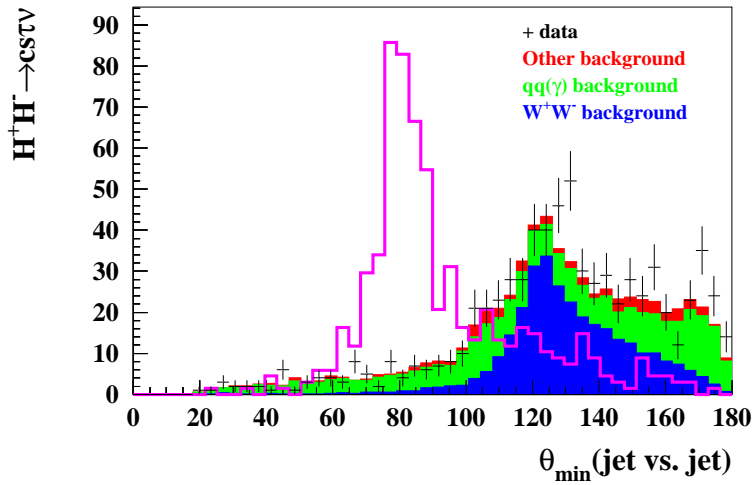

Figure 3.9: Distribution of minimum angle between two jets in the mixed channel. Simulated $qq(\gamma)$ background is shown in blue, W^+W^- background in green and the remaining background reactions in red. For easier visual comparison, distribution of the signal (purple) is rescaled to the total number of background events.

- Variables based on the event topology
  These variables are calculated from momenta of charged particles or momenta of the re-constructed jets and define shape of the event. The variables used are angular distribution of the missing momentum in the event (figure 3.10-2), minimum angle between two jet-s (figure 3.11-3) and angle between reconstructed di-jet and the z axis (figure 3.11-7). In event preselection for the mixed channel, polar angle of the missing momentum was required to be larger than $10°$ in order to suppress the hadronic background.

- Variables based on lepton identification and properties of the τ jets
  Variables using information from the τ decays are the τ-jet energy, $E_{\tau \text{ jet}}$ (figure 3.11-5), τ-jet multiplicity, N_τ (figure 3.11-6) in the case of hadronic and missing momentum of the reconstructed lepton (figure 3.11-8) in case of leptonic decays of the tau. In preselection only events with τ-jet multiplicity less than 9 were accepted thus rejecting a large part of hadronic background. Isolation of τ-jet candidates was defined in terms of the energy of charged particles E_{cone} inside a $30°$ cone around the τ-candidate. An attempt was also made to distinguish τ-jet candidates from other hadronic jets and misassociated tracks by the number of tracks in the jet and by the angle that they formed with direction of the missing momentum.

- Kinematical properties of the event
  Total energy of the event, (figure3.10-1) was required to be below $150\,\text{GeV}$ in the event preselection. This rejected a part of QCD and W^+W^- backgrounds. Effective centre-of-mass energy $s\prime$ after initial state radiation (figure 3.11-4) was used in the same way as in the hadronic channel.
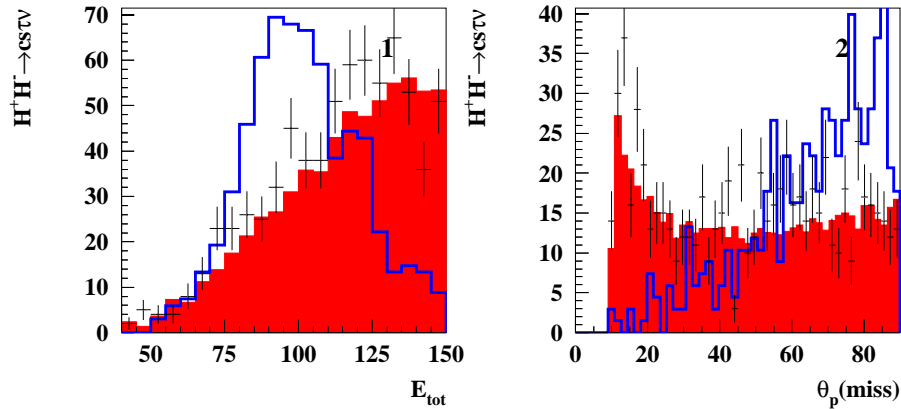

Figure 3.10: Variables used for separation of $H^+H^- \rightarrow c\bar{s}\tau\bar{\nu}_\tau$ from the background. Measured data is represented by histogram with error bars, signal by open blue and background by full red histogram. Signal was rescaled to number of background events for easier visual comparison. Background reactions were rescaled to their corresponding generated cross sections.
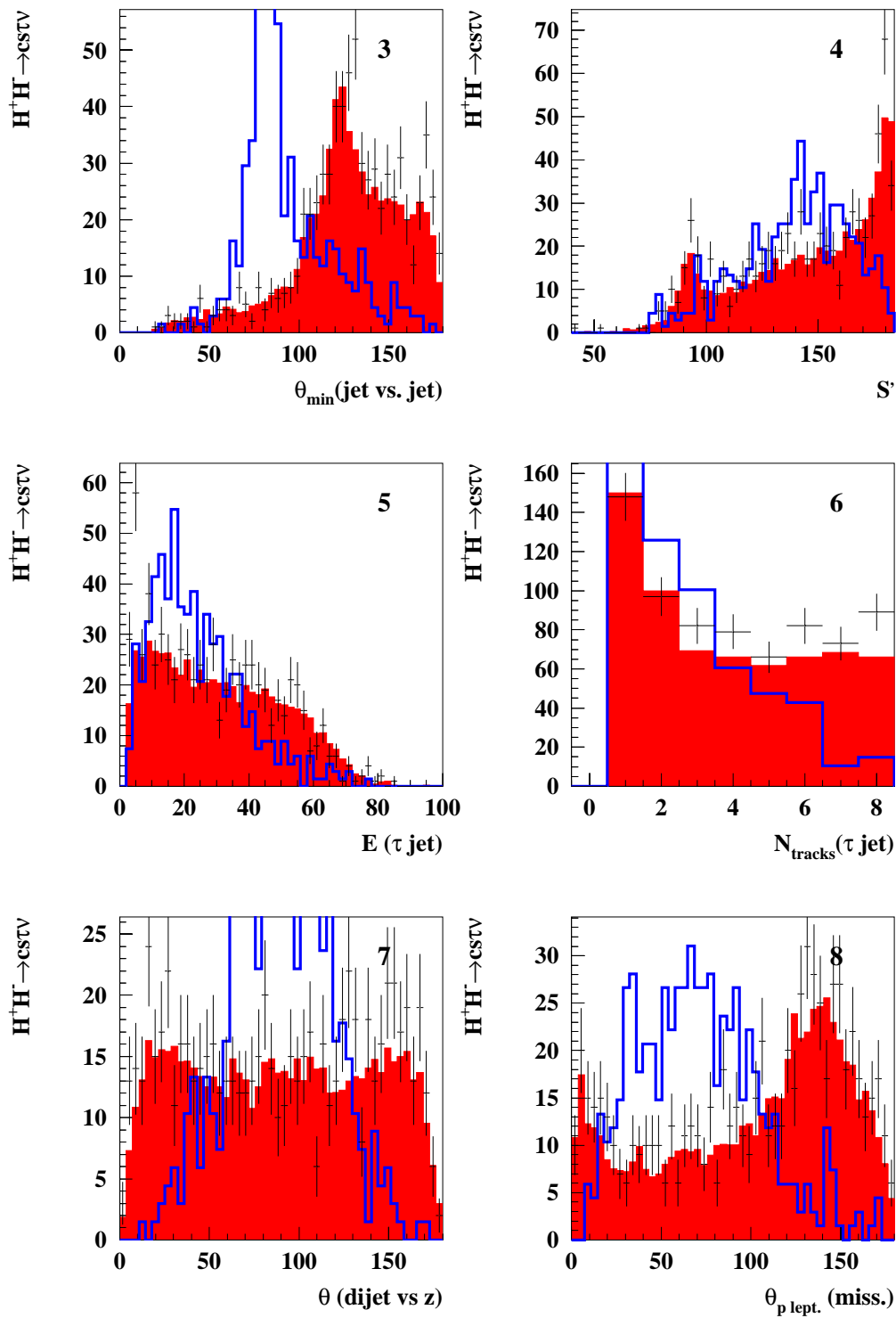
Figure 3.11: Variables used for separation of $H^+H^- \to c\bar{s}\tau\bar{\nu}_\tau$ from the background. Fig. 3.10 Cont'd.

- Flavour tagging

  P_{cs} di-jet probability was calculated using combined b-tagging and particle identification information as described in the section about the hadronic channel. In the mixed channel there is only one hadronic di-jet so P_{cs} can not be combined in P_{cscs}. A sample distribution of P_{cs} for Higgs boson signal generated at $m_H = 60$ GeV is shown in figure 3.12.
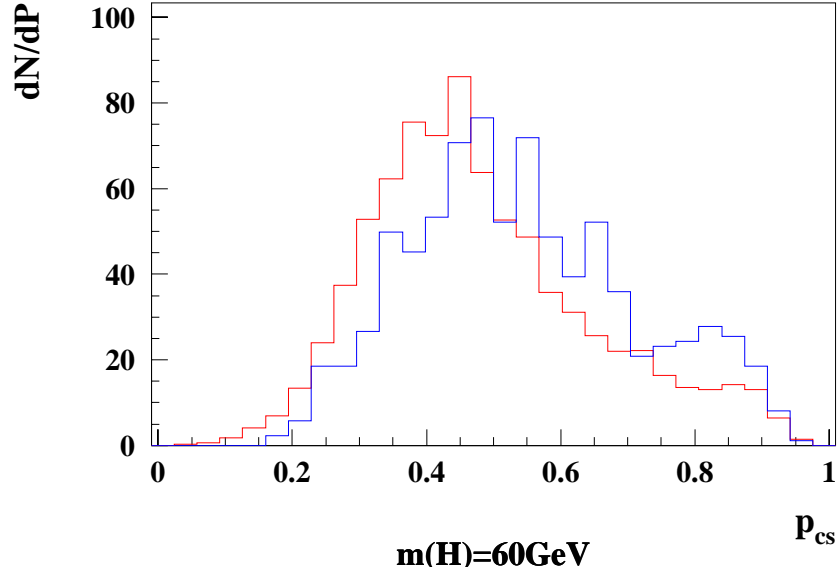

Figure 3.12: Distribution of the P_{cs} separator for the mixed channel. H^+H^- signal distribution is represented by blue and background distribution by red histogram. Signal was rescaled to number of background events for easier visual comparison.

3.5   Leptonic channel

In the leptonic channel there is an abundance of Bhabha scattering events, $e^+e^- \to e^+e^-$. Since the cross-section for Bhabha scattering strongly increases in the forward-backward direction,

$$\frac{d\sigma}{d\Omega} \propto \frac{1}{\sin^4 \theta/2},$$

it can be efficiently rejected by discarding events with large deposited energy in a cone around the beam pipe. The most important types of background that are hard to suppress are two photon reactions, $e^+e^- \to \gamma\gamma$, and production of charged weak bosons, $e^+e^- \to W^+W^-$. Contributions of different background reactions after the preselection to a sample kinematical distribution - momentum of the fastest lepton - is shown in figure 3.13.
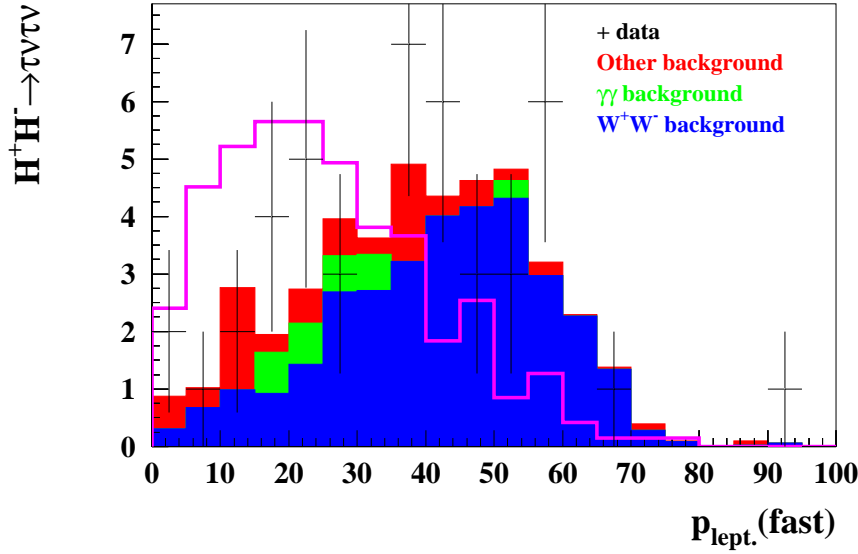
Figure 3.13: Distribution of the momentum of the fastest lepton in the leptonic channel. Simulated W^+W^- background is blue, $\gamma\gamma$ green and the remaining background reactions red. For easier visual comparison, signal (purple) is rescaled to the number of events in total background.

Separating variables for the leptonic channel were chosen in the following way:

- Variables based on the event topology
  We used angular distribution of the missing momentum in the event (figure 3.14-4), polar angle of the jet closest to the beam axis (figure 3.14-13) and aplanarity (figure 3.14-5). Aplanarity, (equation 3.5), was calculated from sphericity tensor (eq. 3.3) as defined in the section on preselection in the hadronic channel.

- Variables based on lepton identification and properties of the τ jets
  These variables were constructed using the properties of tau jets and particle identification. One of them is momentum distribution of the slower lepton P_{lept} in the event (figure 3.14-12), presumably coming from the less energetic τ jet, and the angular distribution of such a lepton weighted by its charge (figure 3.14-10). The same distribution for the fastest lepton is shown in figure 3.14-14.

- Kinematical properties of the event
  Transverse energy of the charged tracks (fig. 3.14-1), number of natural jets before forcing a two jet configuration (fig. 3.14-2), visible energy in the event (fig. 3.14-3), longitudinal missing momentum of the event (along the thrust axis) in fig. 3.14-6, total number of tracks in the event (fig. 3.14-7), maximum energy of a charged particle (fig. 3.14-8), maximum number of charged tracks in a jet (fig. 3.14-9) and invariant mass of the two jets (fig. 3.14-11) were taken into account.
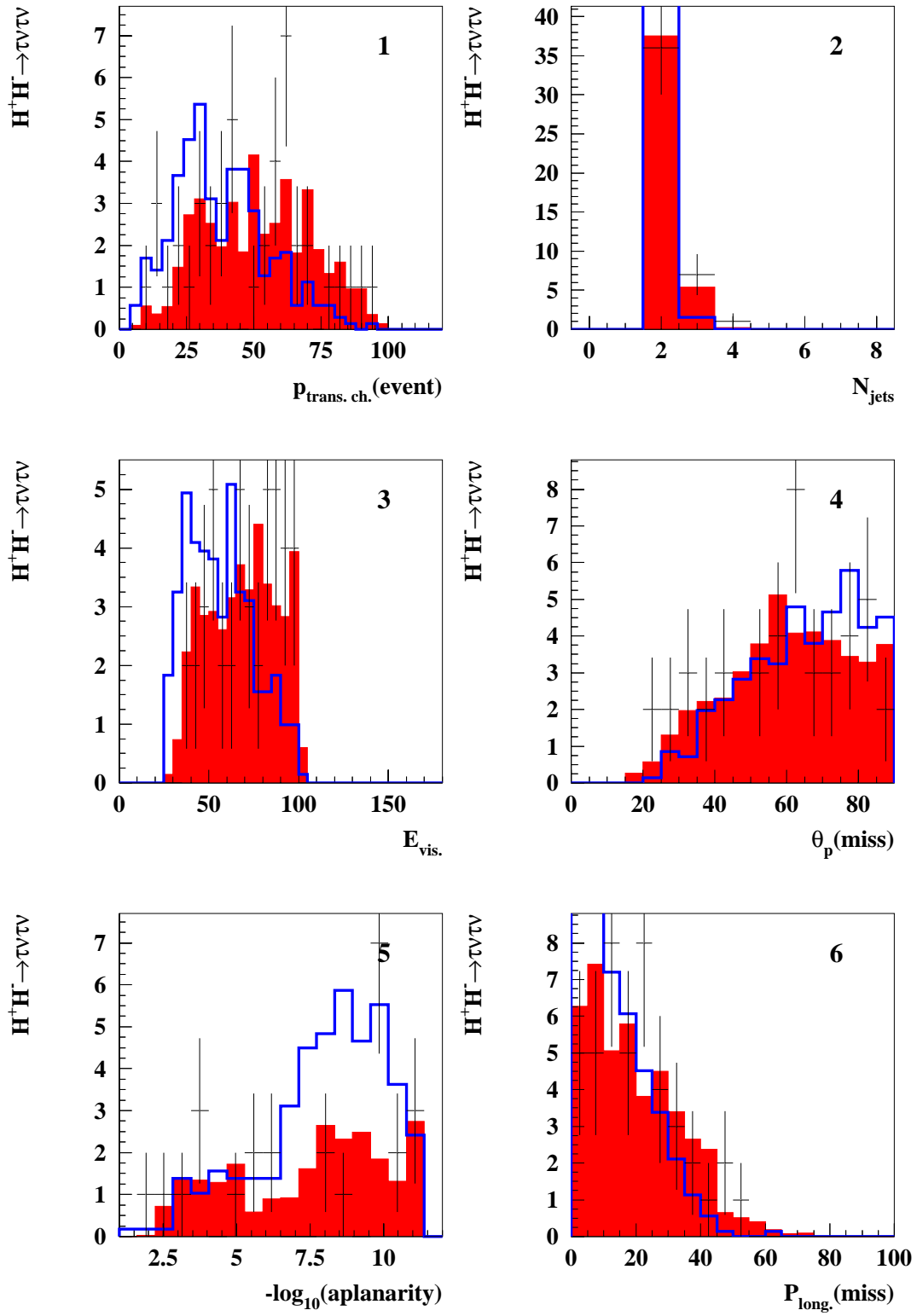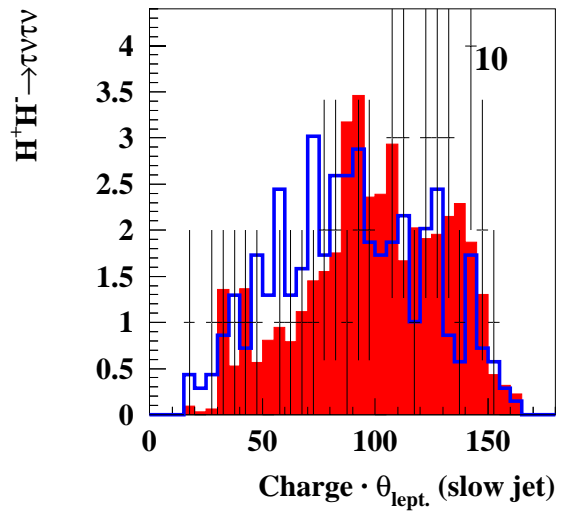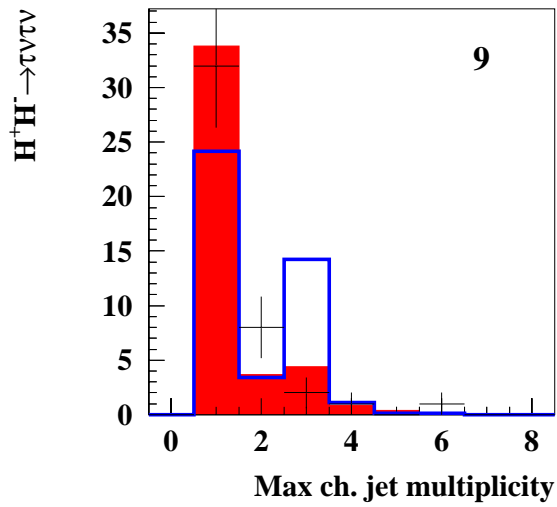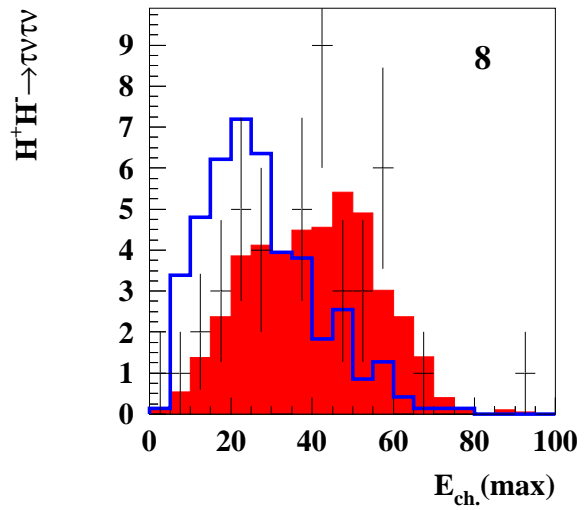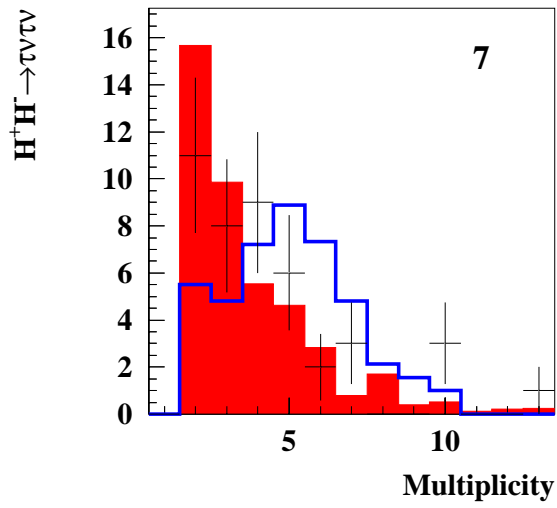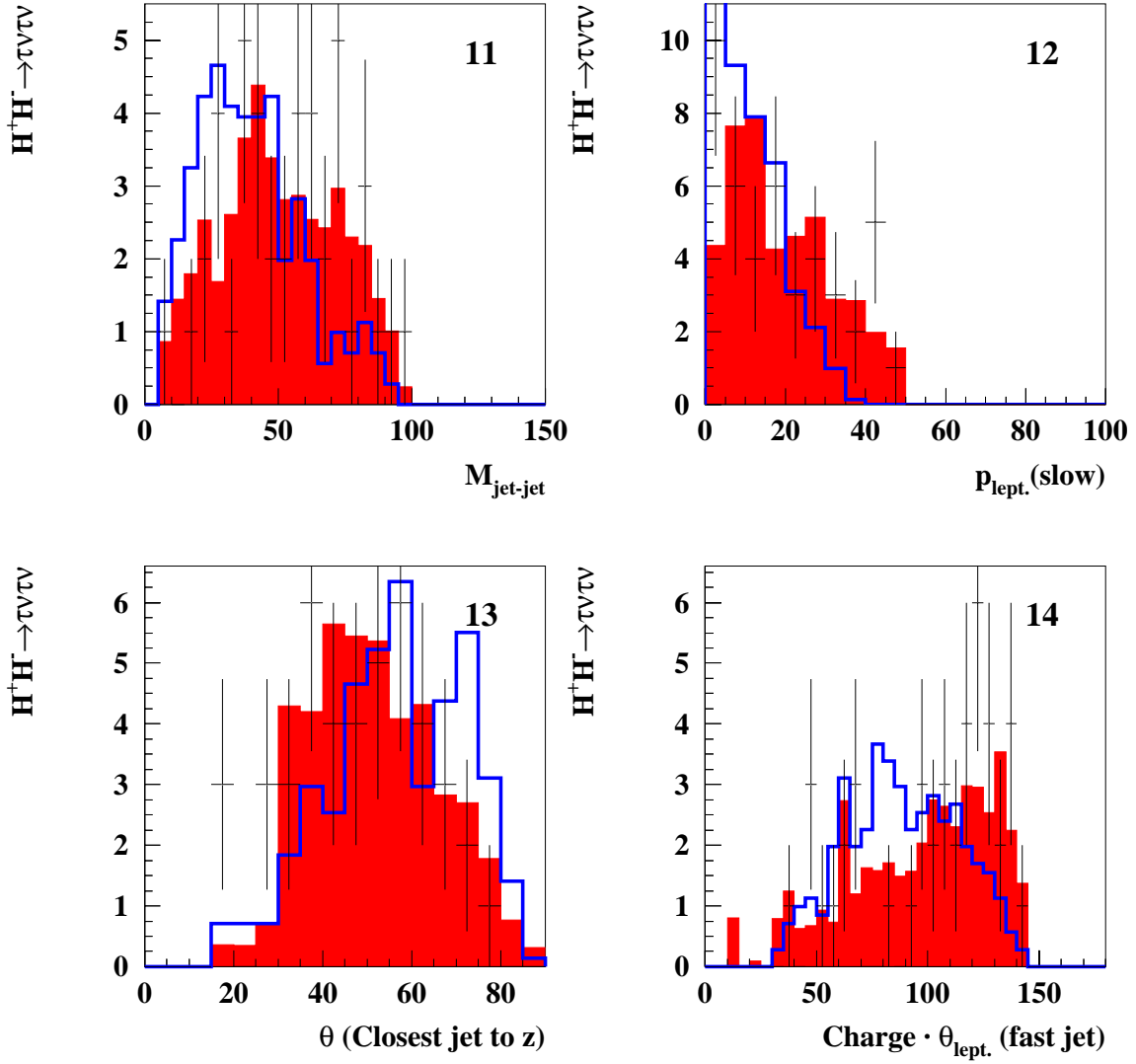
Figure 3.14: Distributions of the observables used for separation of $H^+H^- \rightarrow \tau^+\nu_\tau\tau^-\bar{\nu}_\tau$ from the background are shown in figures 1-14. Distributions of the measured data are drawn with error bars, signal is represented by open blue and background by full red histogram. Signal distributions were rescaled to number of background events for easier visual comparison. Different types of background in the background distribution were rescaled to their corresponding generated cross sections.

3.6 The probabilistic approach

Idea of a probabilistic approach is to construct a signal probability from all separating variables. By choosing a cut on the probability we get a sample of events with desired purity. Construction of the signal probability was done in the following way. First, one had to look at distributions of various kinematical observables as obtained in Monte Carlo in order to estimate their separating power between signal, i.e. charged Higgs boson decays, and background reactions. In the previous sections this was done for all three charged Higgs boson decay channels (hadronic, mixed and leptonic channel). After choosing variables with good separating power between signal and background, their distributions are smoothed (figure 3.15) and normalised to theoretical cross-sections of the appropriate reactions (table 2.2).
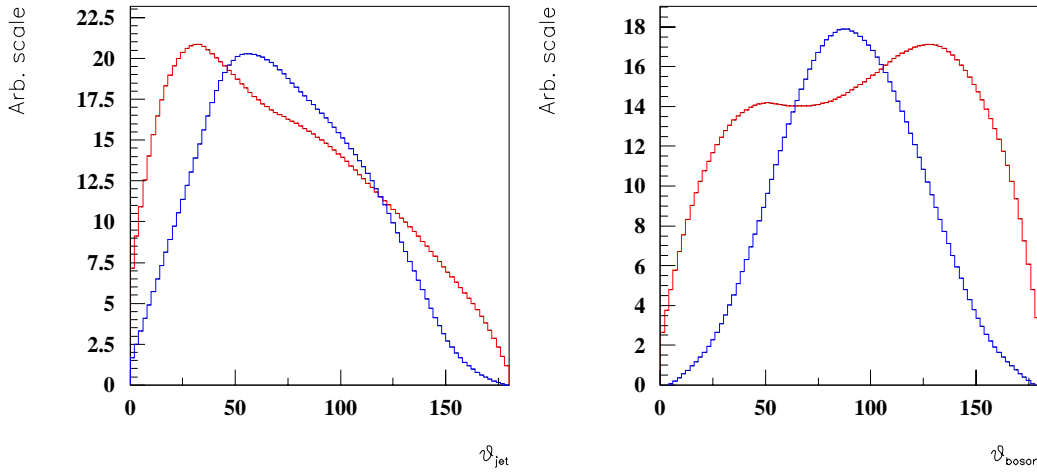

Figure 3.15: Left: Smoothed angular distribution of the jet in the boosted system with respect to the reconstructed boson. Right: smoothed angular distribution of the reconstructed boson with respect to the direction of positrons in the colliding beams. For easier comparison of the signal (blue) and background (red) distributions, signal is rescaled by an arbitrary factor. Sample distributions are for hadronic channel and for the Higgs mass of $60\,\mathrm{GeV}/c^2$.

From an independent set of simulated reactions of the same type as used for obtaining the distributions of kinematical observables, we calculated the probability for a given event with a particular value of the observable x_i to be either a signal (P_i^{sig}) or a background (P_i^{bkg}) event,

$$P_i^{sig} = \frac{\mathcal{L}(x_i)^{sig}}{\mathcal{L}(x_i)^{sig} + \mathcal{L}(x_i)^{bkg}} \qquad (3.8)$$

$\mathcal{L}$ is a distribution for a given observable obtained previously from an independent sample of events. An example of P_i^{sig}, where the observable was centre of mass energy of an event after initial state radiation, is shown in figure 3.16 (top). After calculating partial probabilities for all selected kinematical observables, they are combined into the total kinematical probability for

the signal (figure 3.16 bottom). P^{sig} is obtained as

$$P^{sig} = \frac{\prod_i \frac{P_i^{sig}}{P_i^{bkg}}}{\prod_i \frac{P_i^{sig}}{P_i^{bkg}} + \prod_i \frac{P_i^{bkg}}{P_i^{sig}}} . \tag{3.9}$$

The advantage of this method is that in the process of selection no information is discarded. Separating power of different observables can therefore be exploited in an unbiased sample. Finally, since signal enhanced data samples are obtained by cutting in the final probability only, efficiency and purity of the selection are easy to obtain.
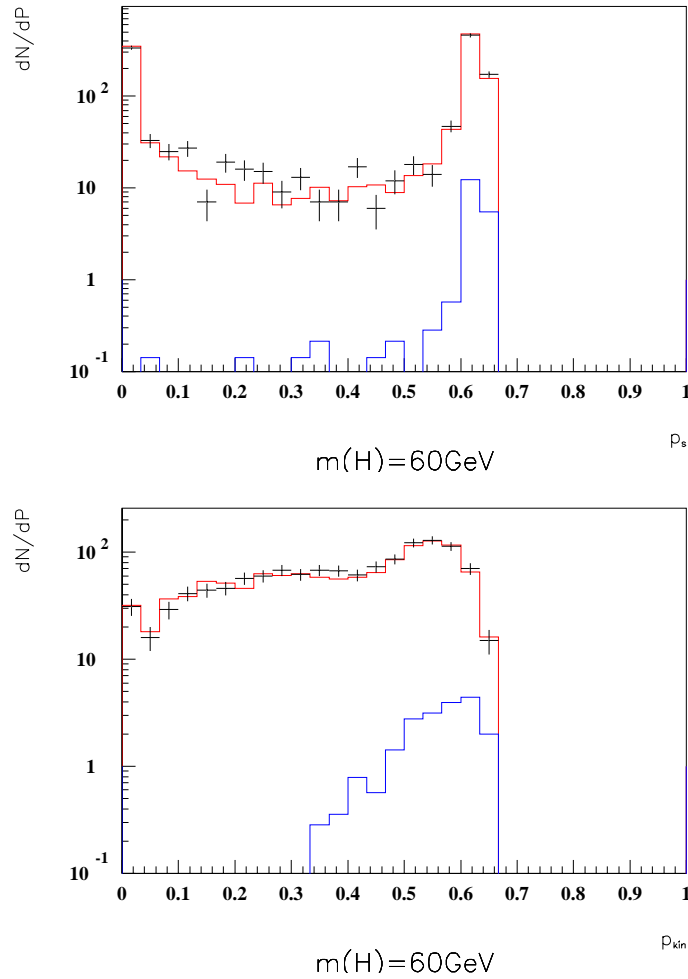
Figure 3.16: Probability for a single observable (centre of mass energy of an event after initial state radiation) that a given event is signal (top) and the total kinematical probability combined from all the selected variables for the hadronic channel. Background reactions are presented by red and signal by blue histogram. Histogram with error bars is probability distribution for the data. Generated Higgs boson mass was $60\,\mathrm{GeV}/c^2$.

Signal probabilities can thus be used for background rejection. A sample of signal events

with desired purity can be obtained from measured data by selecting only events with total event probability above a certain value. Efficiency and purity of the selection are determined from simulated signal and background reactions.

In the hadronic and mixed channel it is possible to enhance efficiency and purity by taking into account reconstructed invariant mass of the dijets. Reconstructed dijet mass can be identified as mass of a Higgs boson, and in simulated Higgs boson samples this mass is well described by a Gaussian peak (figure 3.17). If one searches for a Higgs boson with a specific mass, only events with dijet masses within an interval around that specific mass can be considered. In this way one excludes W^+W^- reactions with their well known peak at $80\,\mathrm{GeV}/c^2$ in the reconstructed dijet mass from calculation of efficiency and purity, which improves performance of the cut. For Higgs boson masses up to $70\,\mathrm{GeV}/c^2$, background in the mass range of interest is relatively flat and in this estimate it was taken to be constant.
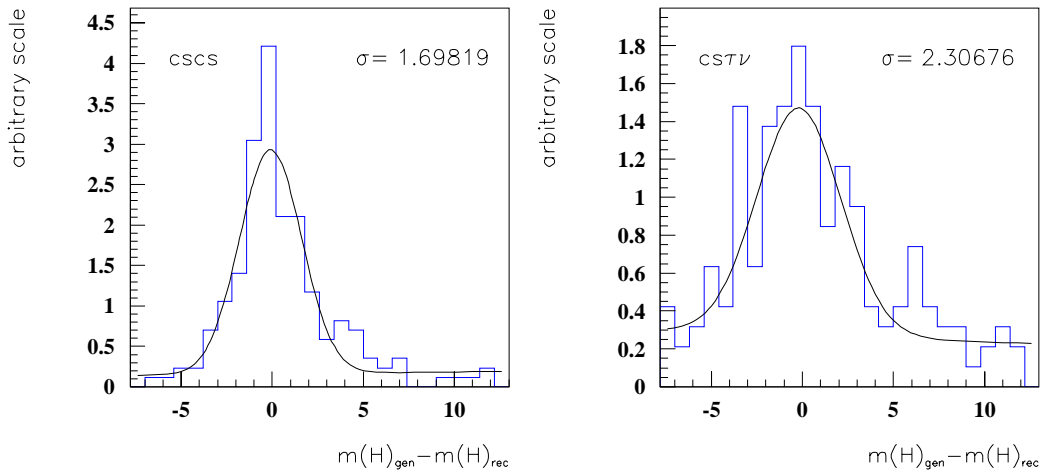
Figure 3.17: Resolution of the reconstructed dijet mass for simulated charged Higgs boson decays in the hadronic channel (left) end mixed channel (right). Generated Higgs boson mass was $60\,\mathrm{GeV}/c^2$. Distributions were fitted by a sum of a Gaussian and a linear function.

This procedure weakly depends on the model used for generation of Higgs boson samples since it uses simulated Higgs boson decays and their cross sections in determination of the optimal cut. Dependence on the simulated Higgs cross section has been studied by repeating the cut optimisation at several different cross sections. In the cross section range of interest, that is for cross sections lower than the one generated by PYTHIA, differences were negligible (figure 3.18).

Another question that had to be answered is determination of interval width for efficiency and purity calculation. Too narrow an interval would loose too much signal and too wide one would not provide enough background rejection. To estimate the interval width providing

optimal separation, signal distribution shape was taken to be Gaussian,

$$s(x) = \frac{s_0}{\sqrt{2\pi}\sigma}\, e^{-x^2/2\sigma^2}, \tag{3.10}$$

and background distribution was taken to be flat,

$$b(x) = \frac{b_0}{2\sigma}. \tag{3.11}$$

By integrating the distributions in an interval $[-a, a]$, we obtain $N'_s = s_0\,\mathrm{Erf}(a/\sqrt{2}\sigma)$ for the signal and $N'_b = a/b_0\sigma$ for the background. Efficiency and purity are calculated as

$$\varepsilon = \frac{N'_s}{N_s},\ P = \frac{N'_s}{N'_s + N'_b}, \tag{3.12}$$

N'_s, N'_b beeing the accepted signal and background and N_s the total signal. In our case, Efficiency times purity is thus

$$\varepsilon \cdot P = \frac{\mathrm{Erf}^2(\kappa/\sqrt{2})}{\mathrm{Erf}(\kappa/\sqrt{2}) + b_0\kappa/s_0}, \tag{3.13}$$

where for convenience interval a is measured in units of Gaussian distribution width, $a = \kappa\sigma$. Dependence of efficiency times purity on the interval width was looked into in three different
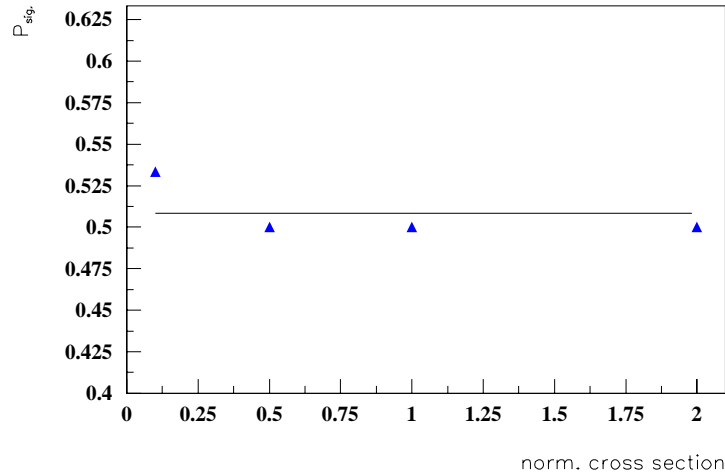
Figure 3.18: Dependence of the cut which maximises efficiency times purity on signal cross section. Figure presents hadronic decay channel of Higgs bosons with mass of $55\,\mathrm{GeV}/c^2$. Cross sections in the figure are measured in units of the generated PYTHIA cross section.

cases (figure 3.19). In the first case (dotted line) signal is half of the background in the given interval, in the second case (blue line) they are equal and in the third case (dashed line) signal

is twice as high as background. Interval providing maximal efficiency times purity varies from $1.4\,\sigma$ in the first to $1.8\,\sigma$ in the third case, where σ is the width of the Gaussian distribution (eq. 3.10). Interval width around $m_{H^\pm}$, for which efficiency times purity is maximal, is obtained using the condition

$$\frac{\partial(\varepsilon \cdot P)}{\partial \kappa} = 0.$$

It is shown as a function of amplitude ratios of signal over background in figure 3.20.

Figure 3.19: Dependence of efficiency times purity at a certain cut value on the interval width around selected Higgs boson mass. In the dotted case, th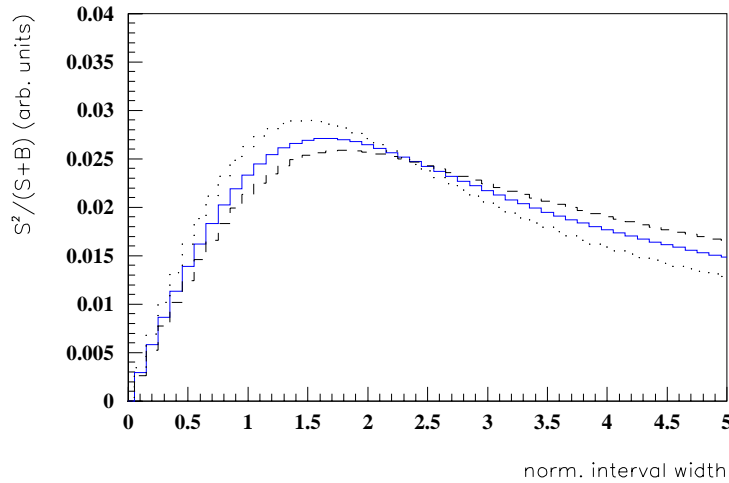e signal amplitude s_0 is one half of the background amplitude b_0, in the blue case they are equal and in the dashed case signal amplitude is twice as high as the background. The interval is measured in units of Gaussian distribution width.

On basis of generated signal and background events, Higgs boson signal is expected to be small or comparable with background in the region of interest (figure 3.21) after aplying the final signal selection cut. The optimal interval width for the event selection in hadronic and mixed channel, as it follows from the estimate above, was thus taken to be 1.5σ around the expected $H^\pm$ mass. To obtain smoother background distribution, interval chosen for the background was 3 standard deviations. Background is than rescaled to be compared with signal,

$$N_b = N_b^s(l_1) \cdot \frac{l_0}{l_1}, \tag{3.14}$$

where N_b^s is the simulated number of background events in the interval l_1 around the generated Higgs mass in the reconstructed dijet mass distribution. l_0 is the interval, where the number of signal events is counted.

Since mass of the Higgs boson is unknown, efficiency and purity of the signal selection had to be optimised separately for each possible mass that could be detected. In our case,
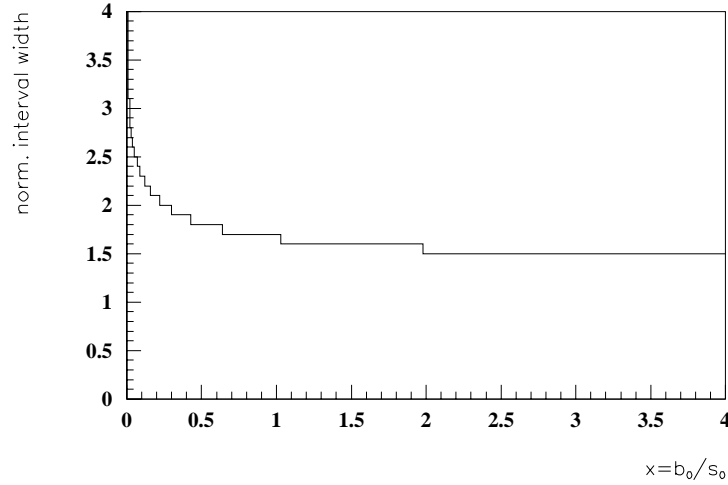
Figure 3.20: Dependence of the interval width around $m_{\mathrm{H}^\pm}$ providing maximal efficiency times purity on signal over background amplitude ratio. Interval is measured in units of Gaussian distribution width.
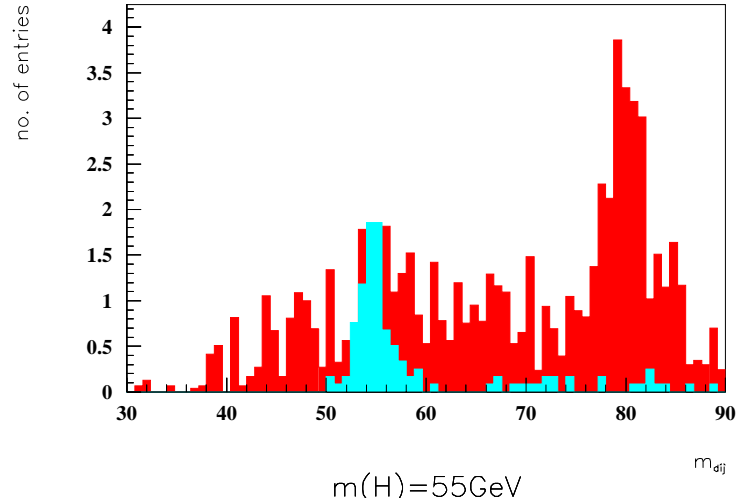
Figure 3.21: Reconstructed dijet mass in the hadronic channel. Distribution includes only events that survive a cut on the signal probability $P_{sig.}$, optimised for maximal efficiency times purity in 1.5σ around simulated Higgs boson mass, $55\,\mathrm{GeV}/c^2$. Signal is represented by light blue and background by red histogram. Both are normalised to generated PYTHIA cross-sections.

this was done in the Higgs boson mass range from 45 to $70\,\mathrm{GeV}/c^2$ in steps of $5\,\mathrm{GeV}/c^2$, due to availability of simulated Higgs boson samples. Doing this, we also took into account that the resolution on the Higgs boson mass depends on the mass itself. Figure 3.22 shows the dependence for both hadronic and mixed channel. Resolutions obtained from Higgs boson samples with different masses were fitted with a linear function. When determining the dijet mass interval for cut optimisation, value obtained by the fit was used.
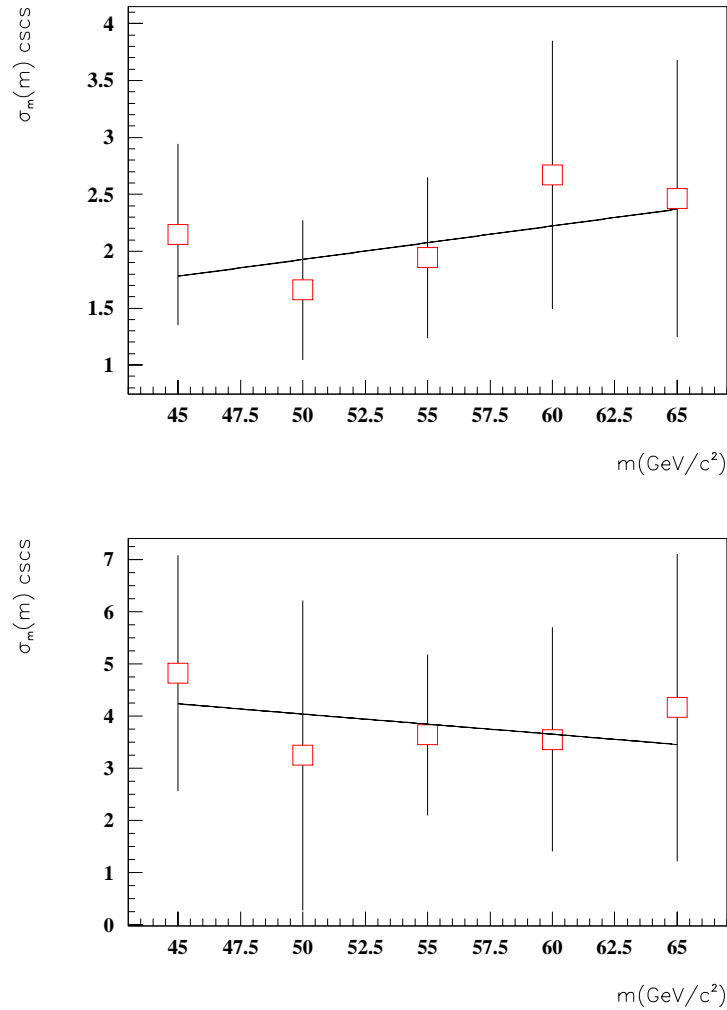
Figure 3.22: Resolution of the reconstructed dijet mass for simulated charged Higgs bosons with masses from 45 to 70 GeV. Top figure shows the hadronic and bottom figure the mixed channel. Resolutions are fitted by a linear function.

An example of the total signal selection probability for all three channels is given in figure 3.23. Mass of the simulated Higgs bosons in this case was $60\ \mathrm{GeV}/c^2$. Arrows in the histograms denote position of the cut on $P_{sig.}$. Signal selection efficiencies for all three channels and for all available simulated Higgs boson samples in the mass range from 45 to $70\ \mathrm{GeV}/c^2$ are shown in figure 3.24.
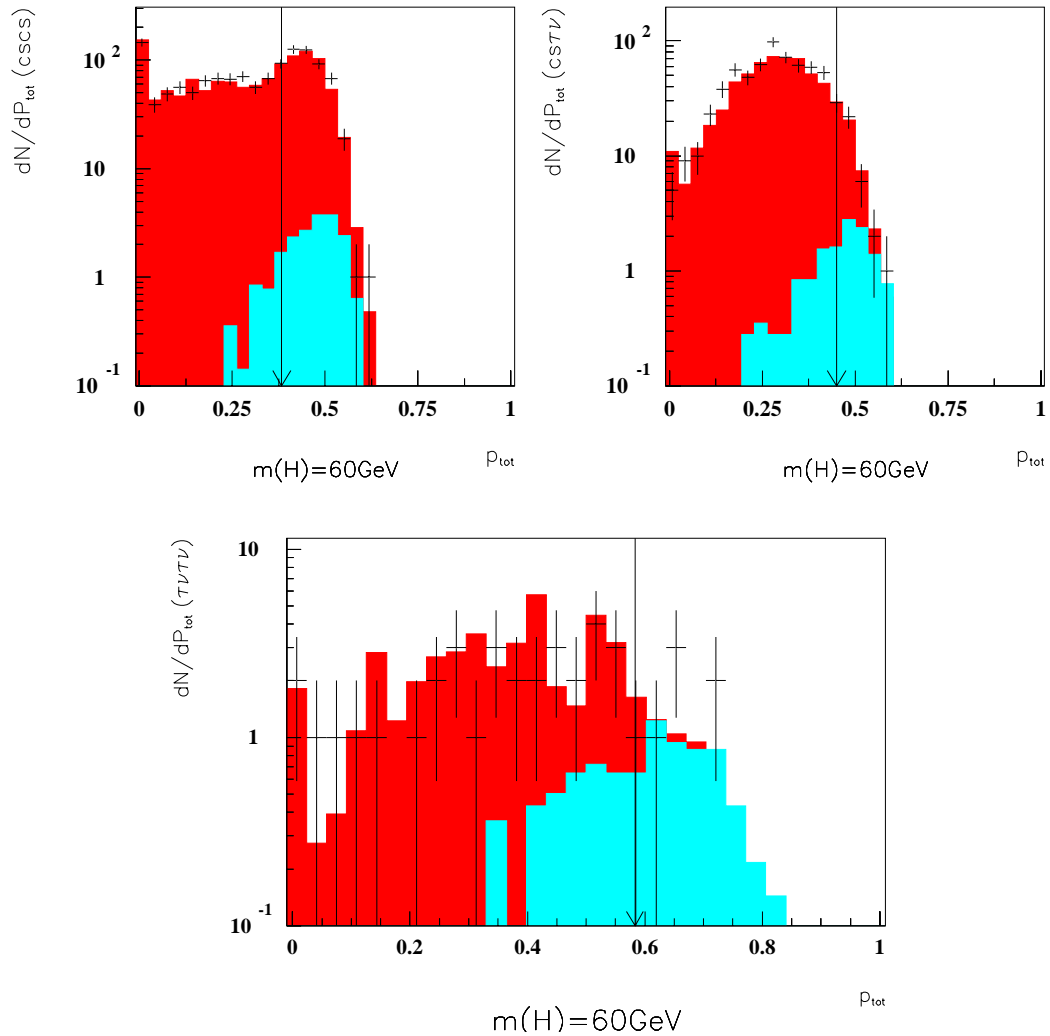
Figure 3.23: Distribution of the final separator for hadronic and mixed channel (top) and leptonic channel (bottom). Red full histogram represents background, blue represents signal and open histogram with error bars stands for measured data. Signal and background histograms are scaled to generated PYTHIA cross-sections. Arrows denote the cut at maximised value of efficiency times purity for given separator.
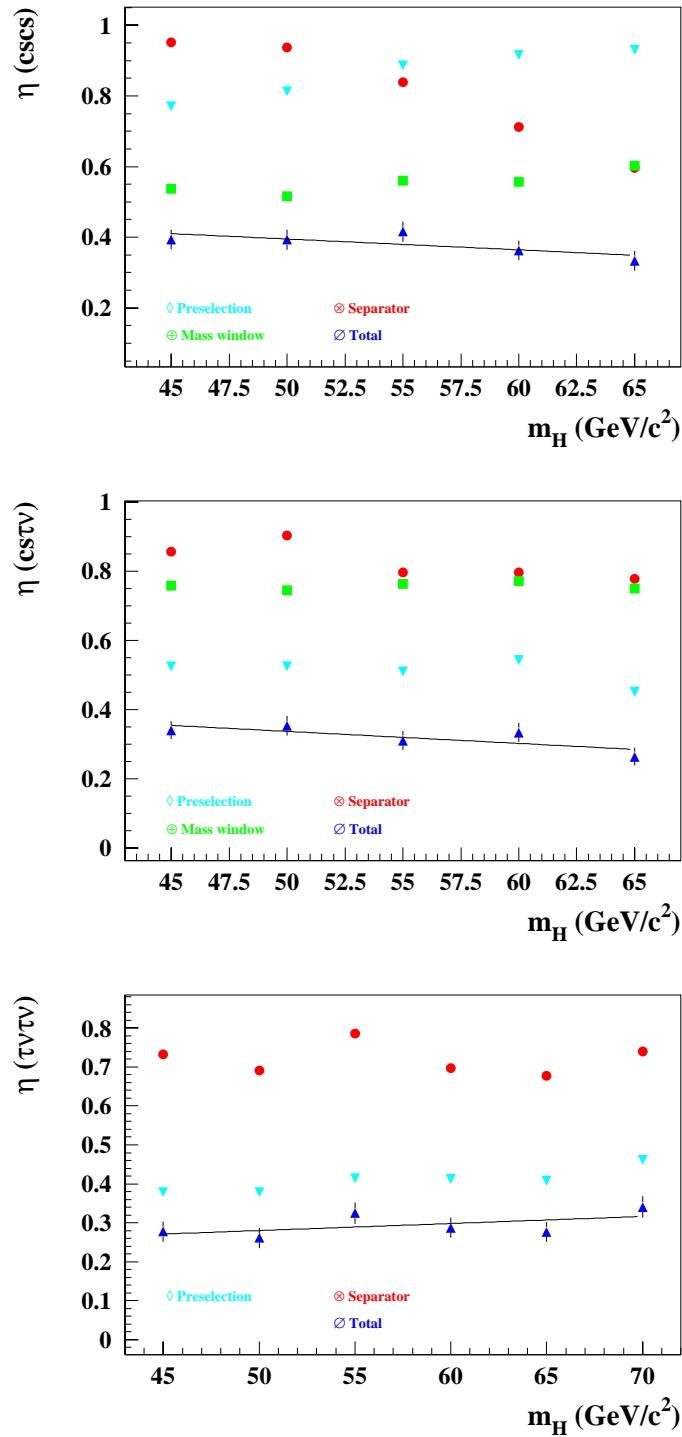
Figure 3.24: Signal selection efficiency for hadronic (top), mixed (centre) and leptonic channel (bottom) for different values of generated Higgs boson mass. Event preselection efficiency is drawn in light blue, efficiency due to a cut in the total signal probability is red and efficiency due to the required mass window is green. They are all combined in the total selection efficiency (dark blue), which is fitted by a linear function.

4

Data Analysis

We tried to extract the charged Higgs boson signal from the events that passed the selection criteria. Since we were looking for decay signatures of particles with well defined but unknown mass, we repeated the analysis for a number of possible Higgs boson masses. The final signal probability P_{sig} (defined in equation 3.9) was calculated for 30 different masses from 43 to $72 \, \mathrm{GeV}/c^2$ in steps of $1 \, \mathrm{GeV}/c^2$. The signal selection was optimised to extract charged Higgs bosons with that specific mass from the data separately for each of the steps. In mass points with no simulated charged Higgs boson samples, kinematical distributions combined in P_{sig} were taken from the sample with smallest mass difference with respect to the chosen mass. In the hadronic and the mixed channel the optimisation included only simulated signal and background events with reconstructed dijet masses within an interval around the chosen Higgs boson mass. In the leptonic channel where no dijet mass reconstruction was possible all events were used. Efficiency used for the cut optimisation was taken from a linear fit to the efficiencies calculated at the Higgs boson masses with available simulated samples (figure 3.24).

Finally, a sample of charged Higgs boson candidates was obtained by cutting at the value of P_{sig} that maximised the product of the efficiency of the selection procedure and purity of the selected sample. If the mass chosen for the cut optimisation was close to the actual mass of the charged Higgs particle we would expect an excess of measured events over the expected background. Number of events surviving the final selection at each chosen mass is shown in figure 4.1 for all three decay channels.

4.1 Unified approach

In the interpretation of measurements we followed the Unified approach to the classical statistical analysis of small signals [48] as suggested by the Particle Data Group [32]. This method is based on frequentist (classical) concept of probability, which depends on the limiting frequency of repeatable experiments. In our case, we wanted to determine number of the signal events s in the measured data.
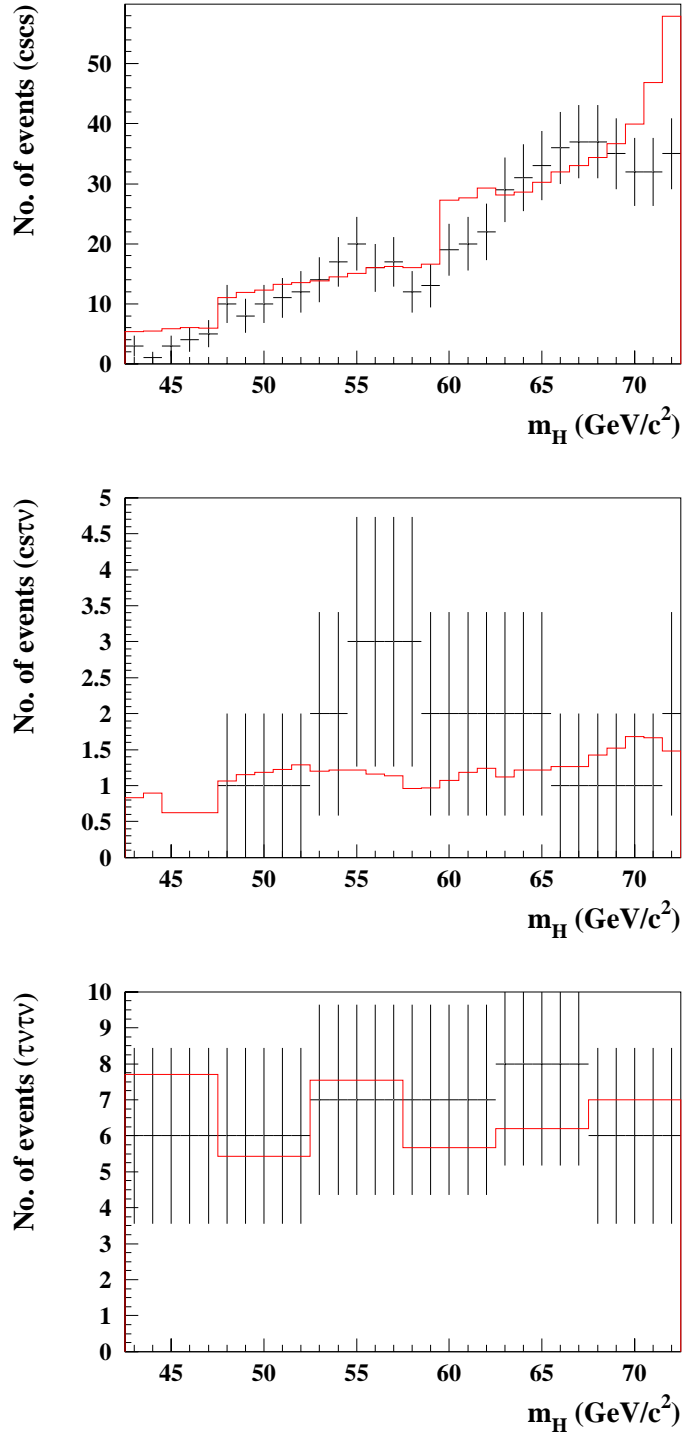
Figure 4.1: Number of events in measured data (histogram with error bars) and simulated background (red) surviving a cut on the signal probability P_{sig} at the expected Higgs boson mass. The cut maximised the product of the efficiency of the selection procedure and purity of the selected sample at a given $m_{H^\pm}$. Histogram entries at different $m_{H^\pm}$ are correlated since they represent the same data at slightly different cut values. Cut optimisations included simulated signal and background events in 1.5σ intervals around simulated Higgs boson masses in the hadronic and mixed channel (top and centre) and all events in the leptonic channel (bottom).

The method limits the value of s within an interval in a case where s has a fixed but unknown mean value μ_s. Properties of the experiment must be embedded in a function $f(n;s)$ that gives the probability of collecting n events of data if the true number of signal events is s. Function $f(n;s)$ has to be known to be able to interpret experimental results. It is determined numerically using simulated Higgs boson events. For a given $f(n;s)$ and an arbitrary value of the parameter s it is possible to obtain such an interval $\big(n_1(s,\epsilon), n_2(s,\epsilon)\big)$ that repeated experiments would give n within that interval in a fraction $1 - \epsilon$ of all cases, the probability for that being

$$P(n_1 < n < n_2) = 1 - \epsilon = \int_{n_1}^{n_2} f(n;s)\,dn. \qquad (4.1)$$

If the interval bounds $n_1(s)$ and $n_2(s)$ are monotonous functions of s they can be re-parametrised as functions of n, namely $s_2(n)$ and $s_1(n)$, respectively. For an arbitrary s_0, all n in the interval $n_1(s_0) < n < n_2(s_0)$ give such bounds $s_1(n)$ and $s_2(n)$ that $s_1(n) < s_0 < s_2(n)$. We can thus write

$$P(n_1(s_0) < n < n_2(s_0)) = 1 - \epsilon = P(s_1(n) < s_0 < s_2(n)). \qquad (4.2)$$

Since this is true by construction for any value of s_0, we obtain the probability that the confidence limits will contain the true value of s:

$$P(s_1(n) < s < s_2(n)) = 1 - \epsilon. \qquad (4.3)$$

In an experiment, numerical values $s_1(n)$ and $s_2(n)$ are obtained by applying the procedure described by equations (4.1, 4.2) to the measured data. Any method giving confidence intervals containing the true value s with probability $1 - \epsilon$ is said to have *coverage*. Frequentist intervals constructed above have coverage by construction.

The condition of coverage (equation 4.1) however does not yet determine bounds of the confidence interval n_1 and n_2 completely, since any range that gives the desired value of the integral has the same coverage. Additional criterion needed to determine the intervals uniquely is the ordering principle [48], which chooses the interval with the largest values of a likelihood ratio. It can be used in the case of Poisson processes where the total number of events n of an observable consist of signal events with an unknown mean μ_s, and background events with a known mean μ_b. Probability to obtain n measured events if the signal mean is μ_s is given as

$$P(n|\mu_s) = e^{-(\mu_s + \mu_b)} \frac{(\mu_s + \mu_b)^n}{n!}. \qquad (4.4)$$

In the same way we can define $P(n|\mu_{best})$ as the probability to obtain n measured events if μ_{best} is the best-fit physically allowed mean. For the background events with the known expected number μ_b, one can now calculate the likelihood $P(n|\mu_s)$ with different hypotheses for the signal mean μ_s. For each n we let μ_{best} be that value of the mean signal μ_s which maximises

$P(n|\mu_s)$. We require μ_{best} to be physically allowed, i.e. non-negative. From equation (4.4) we see that

$$\mu_{best} = \max(0, n - \mu_b).$$

The likelihood ratio R is defined as

$$R = \frac{P(n|\mu_s)}{P(n|\mu_{best})}. \tag{4.5}$$

For a given μ_s, values of n are added to the acceptance region in decreasing order of R until the sum of $P(n|\mu_s)$ meets or exceeds the desired confidence level. Because the number of events n is discrete, the acceptance region contains a summed probability greater than the prescribed confidence level $1 - \epsilon$. This is unavoidable for any ordering principle and leads to conservative confidence intervals. An example of a confidence belt based on this ordering principle is shown in figure 4.2.
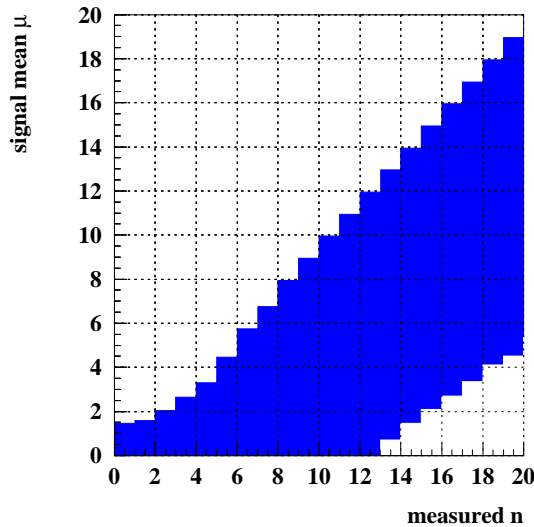
Figure 4.2: A sample confidence belt based on likelihood ratio ordering principle for 95% confidence level intervals for unknown Poisson signal mean μ_s in the presence of a Poisson background with known mean $\mu_b = 7.03$.

The confidence interval calculation was performed for all mass points in hadronic, mixed and leptonic Higgs boson decay channel (figure 4.1) and the obtained intervals that contain the true mean of the signal with 95% confidence are shown in figure 4.3. Since zero can not be excluded as a true mean in either of the mass points in any of the three channels, we are not able to claim a discovery of an excess of events that can be attributed to the production of charged Higgs bosons. Instead, upper limits for the cross-section for the reaction $e^+e^- \rightarrow H^+H^-$ at the LEP collider can be deduced.
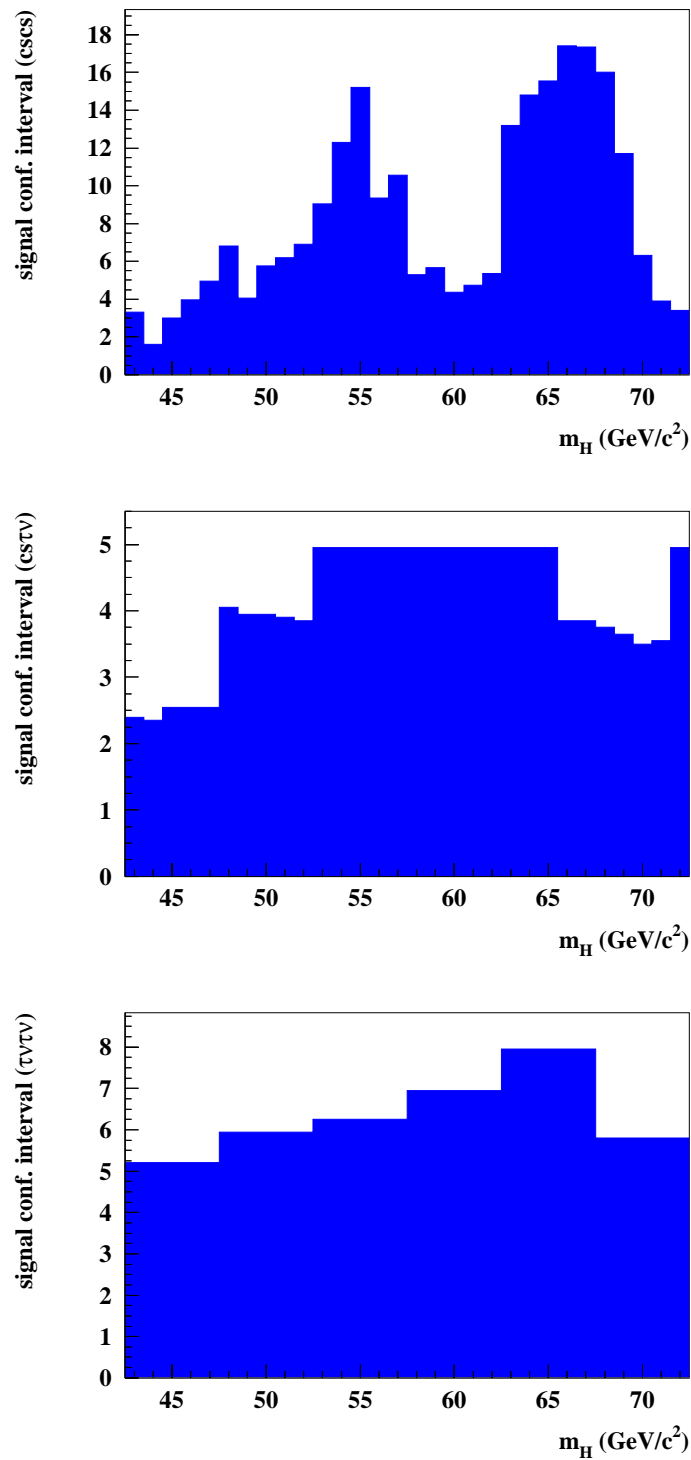
Figure 4.3: 95% confidence intervals that contain true mean of the number of signal events in hadronic (top), mixed (centre) and leptonic channel (bottom plot) as obtained by the likelihood ratio method.

4.2 Upper limits

In a hypothetical case with no background reactions, a small number of measured events n_0 and the signal n_s distributed according to the Poisson statistics, the upper limit on the signal mean μ_s is defined as such a value N, that the probability of observing less or equal than n_0 events in a random observation is ϵ,

$$\epsilon = \sum_{n_s=0}^{n_0} P(n_s; N) = \sum_{n_s=0}^{n_0} \frac{e^{-N} N^{n_s}}{n_s!} \equiv P_{\mu_s}(n_s \leq n_0). \tag{4.6}$$

If a true mean of the signal distribution was μ_s, the measured n_0 would result in N which is less than μ_s in only a fraction ϵ (e.g. 5%) of all cases in the tail of the Poisson distribution (figure 4.4). We say that at a given confidence level, $CL = 1 - \epsilon$, N is the upper limit on the true distribution mean μ_s.
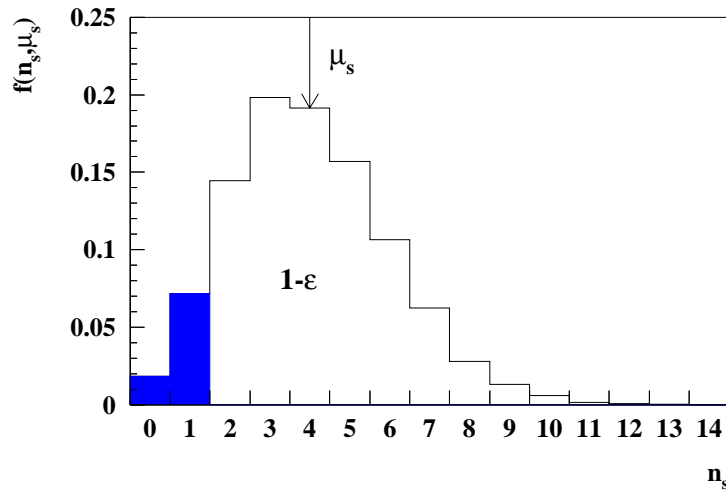
Figure 4.4: Illustration of a confidence interval (unshaded) for determination of an upper limit on a single quantity steming from Poisson processes. Shaded area is integrated probability defined by ϵ.

Usually, as for example in our case, a contribution from the background also has to be taken into account, so the total number of events becomes $n_0 = n_s + n_b$. We do not know the value of n_b, which is the actual number of events resulting from the background processes, but we do know that $n_b \leq n_0$. We assume that background also originates from Poisson processes and that its distribution mean is known with a negligible error. Let N again be the upper limit on μ_s that corresponds to the desired confidence level $1 - \epsilon$. By repeating the experiment with μ_s set to N and μ_b being the expected number of background events, we would observe in total less or equal than n_0 events and would have $n_b \leq n_0$ with a probability ϵ. For any asummed value

of N and μ_b the probability ϵ can be calculated as a ratio of two probabilities,

$$\epsilon = \frac{P_{\mu_s + \mu_b}(n \leq n_0)}{P_{\mu_b}(n \leq n_0)} = \frac{e^{-(\mu_b + N)} \displaystyle\sum_{n=0}^{n_0} \frac{(\mu_b + N)^n}{n!}}{e^{-\mu_b} \displaystyle\sum_{n=0}^{n_0} \frac{\mu_b^n}{n!}}. \tag{4.7}$$

$P_{\mu_s + \mu_b}(n \leq n_0)$ is the probability of observing less than or equal to n_0 events in an experiment where signal and background reactions are Poisson processes with mean values $\mu_s = N$ and μ_b,

$$P_{\mu_s + \mu_b}(n \leq n_0) = e^{-(\mu_b + N)} \sum_{n=0}^{n_0} \frac{(\mu_b + N)^n}{n!}, \tag{4.8}$$

and $P_{\mu_b}(n \leq n_0)$ is the same probability function with μ_s set to zero. This is a generalised case of equation (4.6), which can be obtained by setting $\mu_b = 0$. The value of N is iteratively adjusted until the desired confidence level $1 - \epsilon$ is obtained. As in the case of the likelihood ratio method, this procedure also gives a conservative upper limit, namely, the probability that $N \geq \mu_s$ is greater or equal $1 - \epsilon$ for any given true μ_s.

In two of the three decay configurations, in the hadronic and in the mixed channel, the calculation of the upper limits can be improved by taking into account information from the distribution of dijet masses. For signal events with reconstructed dijets coming from the $H^\pm$ decays, a peak close to the nominal value of $m_{H^\pm}$ is expected while there should be no such enhancement for the background. Technically, this was achieved by multiplying the probability function (eq. 4.8) with a term which includes invariant mass distribution of jet pairs. The new probability function reads

$$\begin{aligned} P_{\mu_s + \mu_b}(n, \vec{m}) &= P_{\mu_s + \mu_b}(n; \mu_s + \mu_b) \cdot M_n(n_1, n_2, \ldots, n_n; p_1, p_2, \ldots, p_n) = \\ &= e^{-(\mu_s + \mu_b)} \frac{(\mu_s + \mu_b)^n}{n!} \cdot n! \prod_{i=1}^{n} \frac{p_i^{n_i}}{n_i!}, \end{aligned} \tag{4.9}$$

where $P_{\mu_s + \mu_b}$ is a Poisson and M_n a multinomial distribution. M_n is a probability to observe n_1 out of n measured events in the first bin of dijet mass distribution, n_2 in the second bin, etc. $p_{1\ldots n}$ are the probabilities that an event, randomly picked from the collected sample of $H^+ H^-$ candidates, would fall into the i-th bin,

$$p_i = \frac{(\mu_s g_s(m_i) + \mu_b g_b(m_i)) \Delta m_i}{\mu_s + \mu_b}.$$

The expected dijet invariant mass distributions for signal and background events, $g_s(m_i)$ and $g_b(m_i)$, were obtained from samples of simulated events (see figure 4.5) and were normalised to unity,

$$\int g_s(m) dm = 1 \text{ and } \int g_b(m) dm = 1.$$

To simplify the calculation, mass bins can be made as narrow as necessary, $\Delta m \rightarrow dm$, so that there is one event at most in each of the bins. In the case where $N_i = 0$, the product term $(p_i^{N_i}/N_i!)$ in equation (4.9) is one, and in the case where $N_i = 1$ the product term is p_i. The total probabilities can thus be rewritten as

$$
\begin{aligned}
P_{\mu_s+\mu_b}(n, \vec{m}) &= e^{-(\mu_s+\mu_b)} \prod_{i=1}^{n} \left(\mu_s g_s(m_i) + \mu_b g_b(m_i) \right) dm, \\
P_{\mu_b}(n, \vec{m}) &= e^{-\mu_b} \prod_{i=1}^{n} \left(\mu_b g_b(m_i) \right) dm.
\end{aligned}
\tag{4.10}
$$

Now we can re-evaluate the upper limits with these new probabilities. Instead of the probability $P_{\mu_s+\mu_b}(n \leq n_0)$ we can introduce a new probability $P_{\mu_s+\mu_b}(X \leq X_0)$, taken that the statistics X satisfies the same ordering relations as n. A good choice would be, for example,

$$
X = \left(\frac{\mu_s + \mu_b}{\mu_b} \right)^n = \left(\frac{\mu_s}{\mu_b} + 1 \right)^n = a^n.
$$

Since a^n is always greater or equal one, the ordering relations remain the same. In our case, we used the statistics

$$
\begin{aligned}
X = \frac{P_{\mu_s+\mu_b}(n, \vec{m})}{P_{\mu_b}(n, \vec{m})} &\propto \frac{\prod_i \left(\mu_s g_s(m_i) + \mu_b g_b(m_i) \right)}{\prod_i \left(\mu_b g_b(m_i) \right)} = \\
&= \prod_{i=1}^{n} \left(\frac{\mu_s g_s(m_i)}{\mu_b g_b(m_i)} + 1 \right),
\end{aligned}
\tag{4.11}
$$

which was proven to be optimal for the discovery of small signals in processes with background [50]. The upper limit on μ_s was derived in a similar way as before. First the statistics X_0 was calculated for n_0 measured events where also the values of their dijet invariant masses were taken into account. Then the upper limit N on μ_s was determined by solving the equation

$$
\epsilon = \frac{P_{\mu_s+\mu_b}(X \leq X_0)}{P_{\mu_b}(X \leq X_0)},
\tag{4.12}
$$

where X denotes the statistics of a sample, simulated according to the probability function (4.10) with $\mu_s = N$ and μ_b being the mean values for signal and background. The equation (4.12) was solved using Monte Carlo integration.

The upper limits on μ_s were calculated for 30 different charged Higgs boson masses from 43 to $72\,\mathrm{GeV}/c^2$ in steps of $1\,\mathrm{GeV}/c^2$. Results of both, the event counting upper limit calculation (equation 4.7) and the calculation taking into account dijet mass distributions (equation 4.12) are shown in figure 4.6.
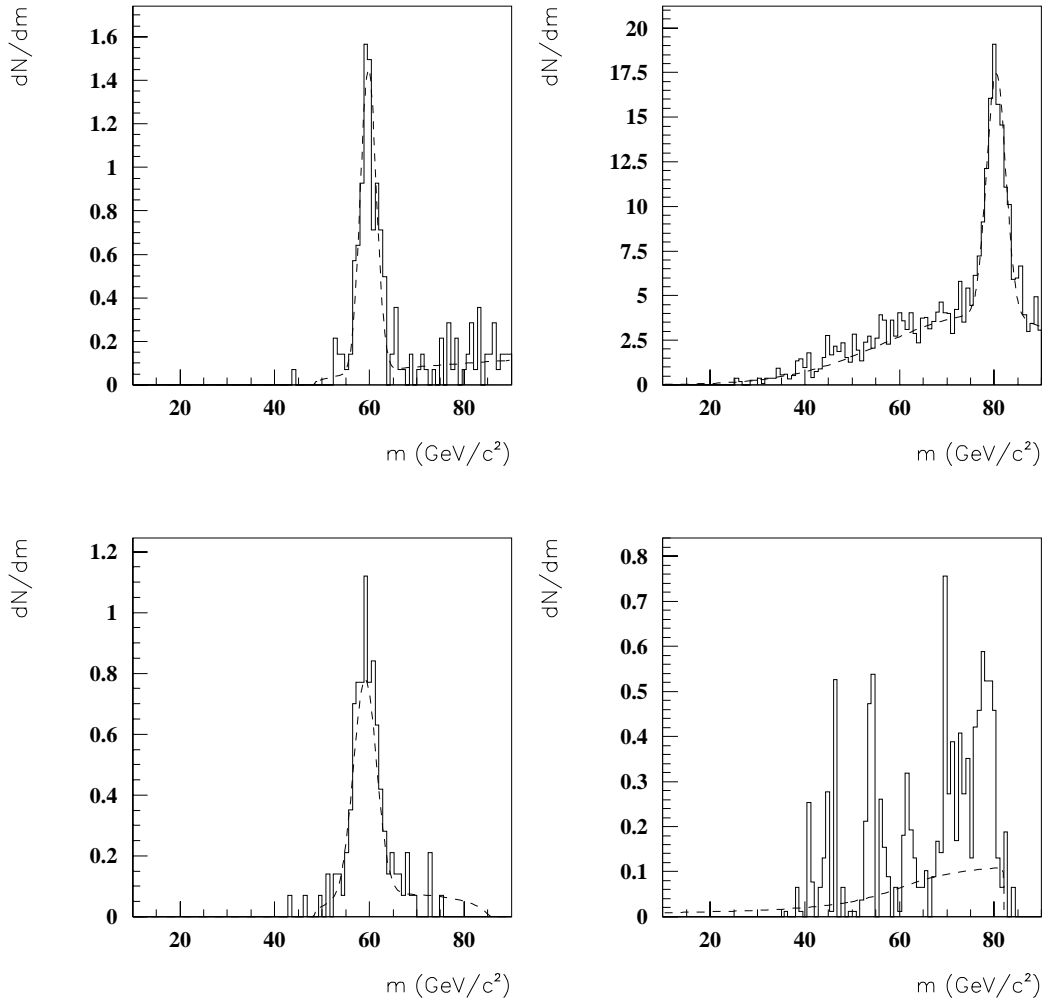
Figure 4.5: Example of a fit of the reconstructed dijet mass for simulated signal (left column) and background reactions (right column). Top figures show the distributions in the hadronic and the bottom ones in the mixed channel. The signal sample was generated with $m_{\mathrm{H}^\pm} = 60\,\mathrm{GeV}/c^2$. Enhancement of the background at $m \sim 80\,\mathrm{GeV}/c^2$ is a result of the production of $\mathrm{W}^+\mathrm{W}^-$ pairs. Simulated samples were normalised to the luminosity of the collected data.
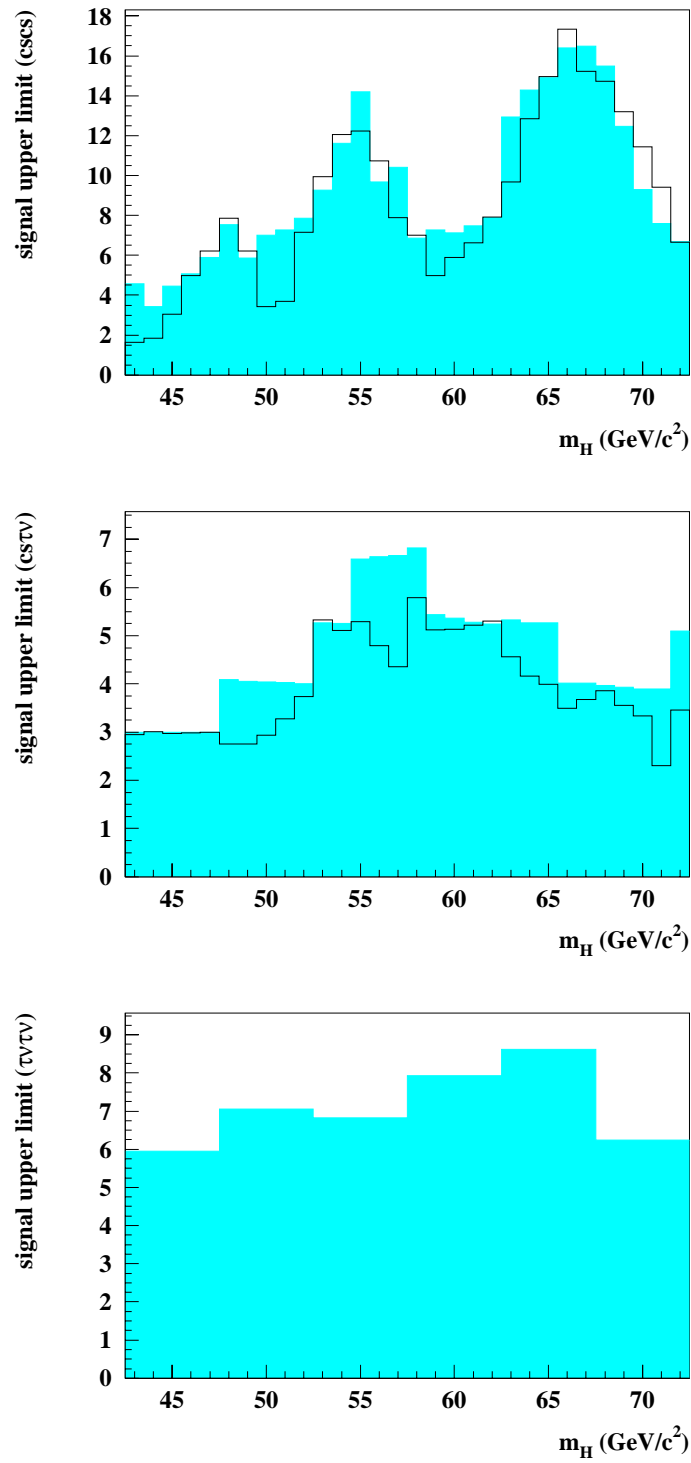
Figure 4.6: Upper limits with 95% confidence level on the number of signal events in hadronic (top), mixed (centre) and leptonic channel (bottom figure). The blue histograms present the calculation of eq. (4.7), taking into account the Poisson probability only. The black histogram in the hadronic and mixed channel takes into account also the reconstructed dijet mass information (eq. 4.12).

Having the upper limits on the number of signal events in hadronic, mixed and leptonic channels ready, we wanted to set an upper limit on $e^+e^- \to H^+H^-$ cross-section. However, the branching ratios for H^+ and H^- decays are not known, so we can only obtain the H^+H^- pair production cross-section upper limit weighted by a product of the unknown branching ratios. Since we assume that $H^+ \to c\bar{s}$ and $H^+ \to \tau^+\nu_\tau$ are the only two types of charged Higgs boson decays taking place in the investigated Higgs boson mass range, the sum of the two branching ratios can be constrained to unity. The branching ratios for the two decays

$$
\begin{aligned}
\mathrm{Br}\,(H^+ \to c\bar{s}) &= \mathrm{Br}\,(H^- \to \bar{c}s) = r, \\
\mathrm{Br}\,(H^+ \to \tau^+\nu_\tau) &= \mathrm{Br}\,(H^- \to \tau^-\bar{\nu}_\tau) = 1 - r,
\end{aligned}
\tag{4.13}
$$

can therefore be parametrised by a single parameter r. Cross-section upper limits, obtained from the analyses of the three possible H^+H^- decay channels, are thus

$$
\begin{aligned}
\sigma_{UL}(\text{hadronic}) &= \sigma(e^+e^- \to H^+H^-) \times r^2 = \frac{N_1}{L\varepsilon_1}, \\
\sigma_{UL}(\text{mixed}) &= \sigma(e^+e^- \to H^+H^-) \times 2r(1-r) = \frac{N_2}{L\varepsilon_2}, \\
\sigma_{UL}(\text{leptonic}) &= \sigma(e^+e^- \to H^+H^-) \times (1-r)^2 = \frac{N_3}{L\varepsilon_3}.
\end{aligned}
\tag{4.14}
$$

where $N_{1..3}$ (figure 4.6) are the upper limits on the number of signal events for a given Higgs boson mass in a given decay channel. N_1 stands for the hadronic, N_2 for the mixed and N_3 for the leptonic decay channel. L is the integrated luminosity of the analysed data. The signal selection efficiencies ε_i for the three channels were obtained from simulated samples as described in the third chapter.

Plots of the cross-section upper limits (4.14) are shown in figure 4.7. The obtained upper limits are compared to the predicted PYTHIA cross-section $\sigma(e^+e^- \to H^+H^-)$.

To be able to set a limit on charged Higgs boson mass, measured data in the three decay channels (figure 4.1) have to be combined into a $e^+e^- \to H^+H^-$ cross-section upper limit for all possible values of the branching ratio r (equation 4.13). This yields a two dimensional distribution of the cross-section upper limit, depending both on $m_{H^\pm}$ and on the parameter r. In order to consider all three decay channels simultaneously, the equation (4.7) must be replaced by

$$
1 - \epsilon = 1 - \prod_{i=1}^{3} \frac{P_{\mu_s + \mu_b}(X^i \le X_0^i)}{P_{\mu_b}(X^i \le X_0^i)},
\tag{4.15}
$$

where the index $i = 1$ stands for the hadronic, $i = 2$ for the mixed and $i = 3$ for the leptonic decay channel.
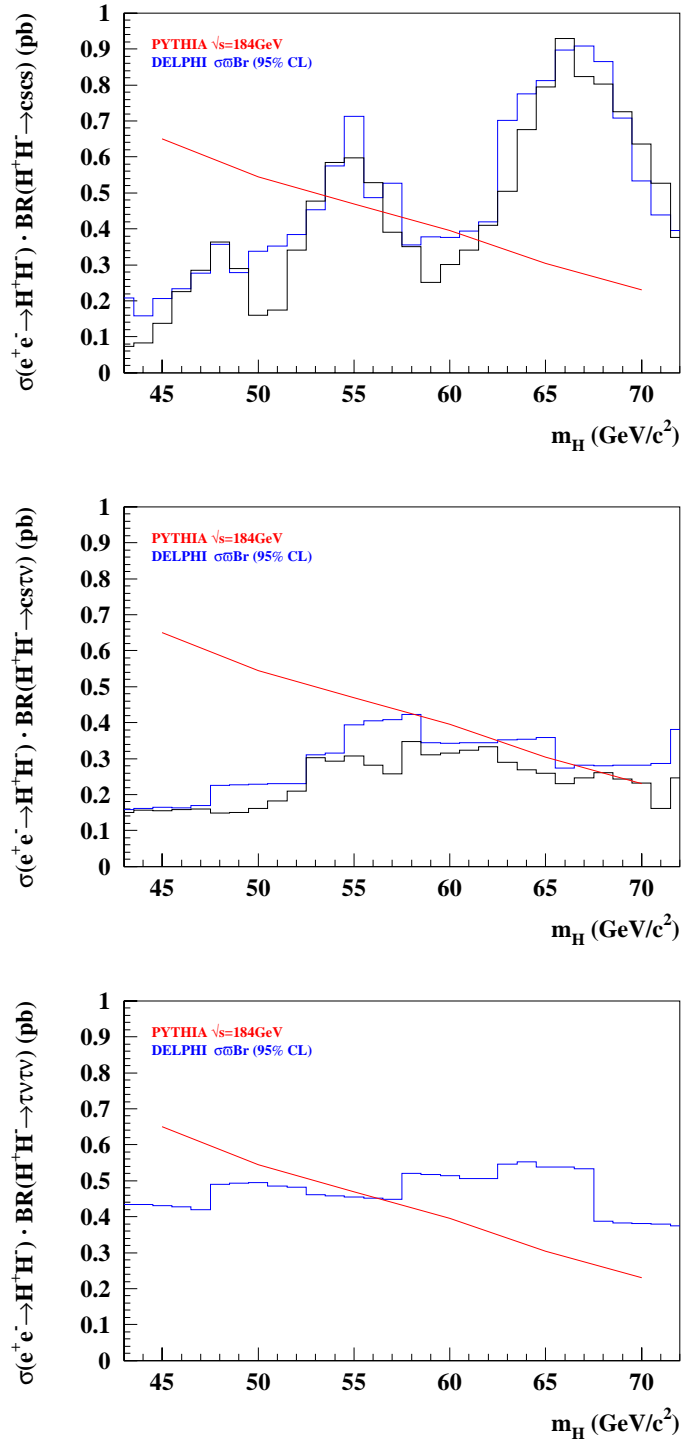
Figure 4.7: Plots of cross-section upper limits times branching ratios for the hadronic (top), mixed (centre) and leptonic channel (bottom). Blue histograms present the upper limits taking into account only the Poisson probabilities. Black histograms in the hadronic and mixed channels take into account also the reconstructed dijet mass information. Cross-section predicted by PYTHIA is red. In the case of PYTHIA, branching ratio for each decay channel was taken to be one.

The statistics X^i is a function of N_i, which in turn can be expressed in terms of the $e^+e^- \rightarrow H^+H^-$ cross-section, efficiencies and integrated luminosities corresponding to the three decay channels and the branching ratio r (see eqeuation 4.14). The combined upper limit on $\sigma(e^+e^- \rightarrow H^+H^-)$ was then derived with required confidence level $1 - \epsilon$ by numerical integration of equation (4.15) separately for different values of $m_{H^\pm}$ and r.

Figure 4.8: Top: Exclusion region for charged Higgs bosons in the plane $\mathrm{Br}(H \rightarrow \mathrm{hadrons})$ vs. charged Higgs boson mass as obtained from the collected data. Existence of a $H^\pm$ with mass in the blue region is excluded with 95% confidence level. Bottom: Expected exclusion region for charged Higgs bosons in the plane $\mathrm{Br}(H \rightarrow \mathrm{hadrons})$ vs. charged Higgs boson mass as obtained from the simulation.
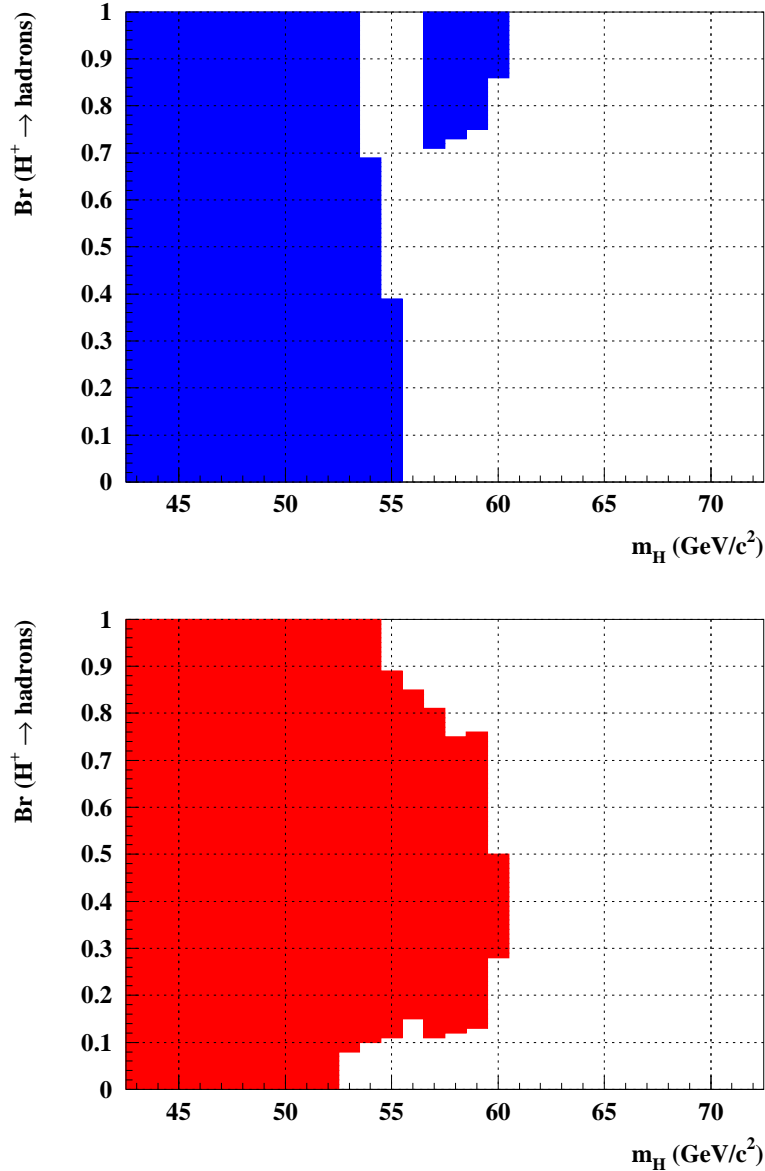
To set a lower limit on the charged Higgs boson mass, one has to compare upper limits on the cross-section to the values predicted by a model. If the measured $\sigma(e^+e^- \rightarrow H^+H^-)$ is smaller than the predicted cross-section at a given mass $m_{H^\pm}$ for all possible values of the branching ratio r, then the existence of a charged Higgs boson at that mass can be excluded with a certain confidence $1 - \epsilon$. The obtained lower limit on $m_{H^\pm}$ of course strongly depends on the chosen model, since the exclusion criterion depends directly on the model generated $e^+e^- \rightarrow H^+H^-$ cross-section. Results of the comparison of cross-section upper limit to the PYTHIA event generator predicted cross-section is shown as an exclusion region in figure 4.8. The described analysis sets a lower limit on $H^\pm$ mass at

$$m_{H^\pm} > 53.5 \, \text{GeV}/c^2 \tag{4.16}$$

at a 95% confidence level.

Apart from the measured lower limit on the charged Higgs boson mass, we also calculated the expected lower limit. In this calculation the number collected data events is substituted by a randomly generated number of events according to Poisson distribution with μ_b as its mean. By repeating the calculation and taking the mean value of all calculated cross-section upper limits, the expected cross-section can be obtained with desired precision. An exclusion region obtained after comparing the upper limit with the PYTHIA event generator predicted cross-section is shown if figure 4.8 (bottom).

4.3 Systematic uncertainties

It is expected that the biggest systematic uncertainties of the measurement could arise mainly from two different sources: from unadequate description of quark and gluon fragmentation and detector response in computer simulated events, and from poorly known cross-sections for different background reactions, e.g. cross-sections for the two-photon interactions. Instead of taking them into account one by one, we tried to construct two inclusive systematic checks, each covering as many sources as possible. Both of them were studied for each decay channel separately.

4.3.1 Systematic uncertainties on the signal selection efficiency

The uncertainty of the signal efficiency stems in uncertainties of the simulated probability distributions. The largest contribution to the signal efficiency is expected from modelling of fragmentation processes and modelling of the detector response to simulated reactions. We tried to include all sources contributing to the uncertainty of the signal selection efficiency in the following check.

At the beginning of the data taking, each year the LEP collider operated for some time at centre-of-mass energy of $91 \, \text{GeV}$, at the so called Z^0 peak. By merging the collected Z^0 decays two by two, one can nicely reproduce the H^+H^- decay topology. Systematic uncertainty on the

selection of possible signal events was estimated by comparing measured and simulated merged Z^0 events.

First, we separated hadronic Z^0 decays from leptonic decays, which were further classified into $\tau\tau$ decays and the rest of the leptonic processes. The separation criteria were very loose. For an event to pass as a hadronic Z^0 decay we required more than five charged tracks and the total reconstructed energy larger $15\,\mathrm{GeV}$. An event was selected as a leptonic decay if the two jets were oriented back to back and enough energy was reconstructed. Tau events were separated from the rest on the basis of the number of reconstructed particle tracks and reconstructed energy. Particles belonging to one of the jets were removed to simulate a neutrino of a leptonic H decay. A part of events was removed from the sample in order to obtain the same angular distributions of jets as expected for the jets from H^+H^- decays. The remaining Z^0 events were then merged two by two into new events. Momenta of the particles were rescaled to correspond to charged Higgs boson decays.

The selected simulated sample was normalised to the number of selected Z^0 events in the measured sample. From this point on, merged Z^0 events passed the same analysis procedure as the high energy events. The whole procedure yields six signal probabilities P_{sig}, one per channel for the merged measured Z^0 events and one per channel for the simulated ones. Agreement between P_{sig} distributions of the real and the simulated merged events is shown in figure 4.9. After a cut on P_{sig} with the same selection efficiency as in the charged Higgs boson analysis, relative differences of the selection efficiencies between real and simulated merged events were used to estimate the systematic uncertainty (equation 4.17).

$$\sigma_{eff} = \frac{\varepsilon_{sim} - \varepsilon_{data}}{\varepsilon_{sim}} \tag{4.17}$$

ε_{MC} is the selection efficiency for the simulated and ε_{data} for the measured merged Z^0 events. Statistical errors of relative differences were also taken into account and added to the overall systematic error. The obtained values of σ_{eff} for the three channels are summarised in table 4.1.

We believe that the presented systematic check includes most of the systematic effects due to jet fragmentation and detector response simulation. The results are valid under an assumption that the performance of the DELPHI spectrometer did not change significantly during the entire period of data taking. Stability of the spectrometer was tested by looking at the time evolution of some general quantities in the high energy data. No significant effects were observed.

4.3.2   Systematic uncertainties due to the background description

The main source of the uncertainty on the background description comes from the poorly known cross-sections for different background processes and from inadequate modelling of the detector response.
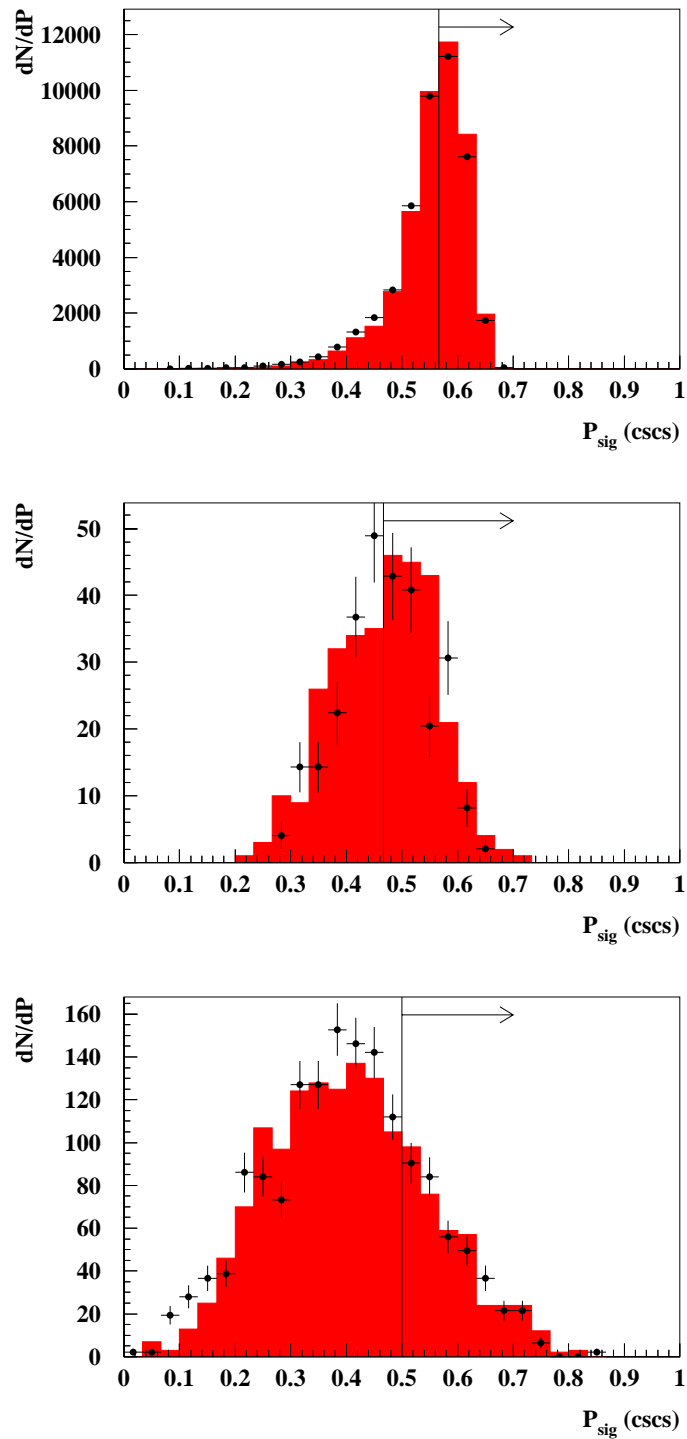
Figure 4.9: Comparison of probability distributions between measured and simulated merged Z^0 events, used to estimate the systematic errors of the signal selection efficiency.
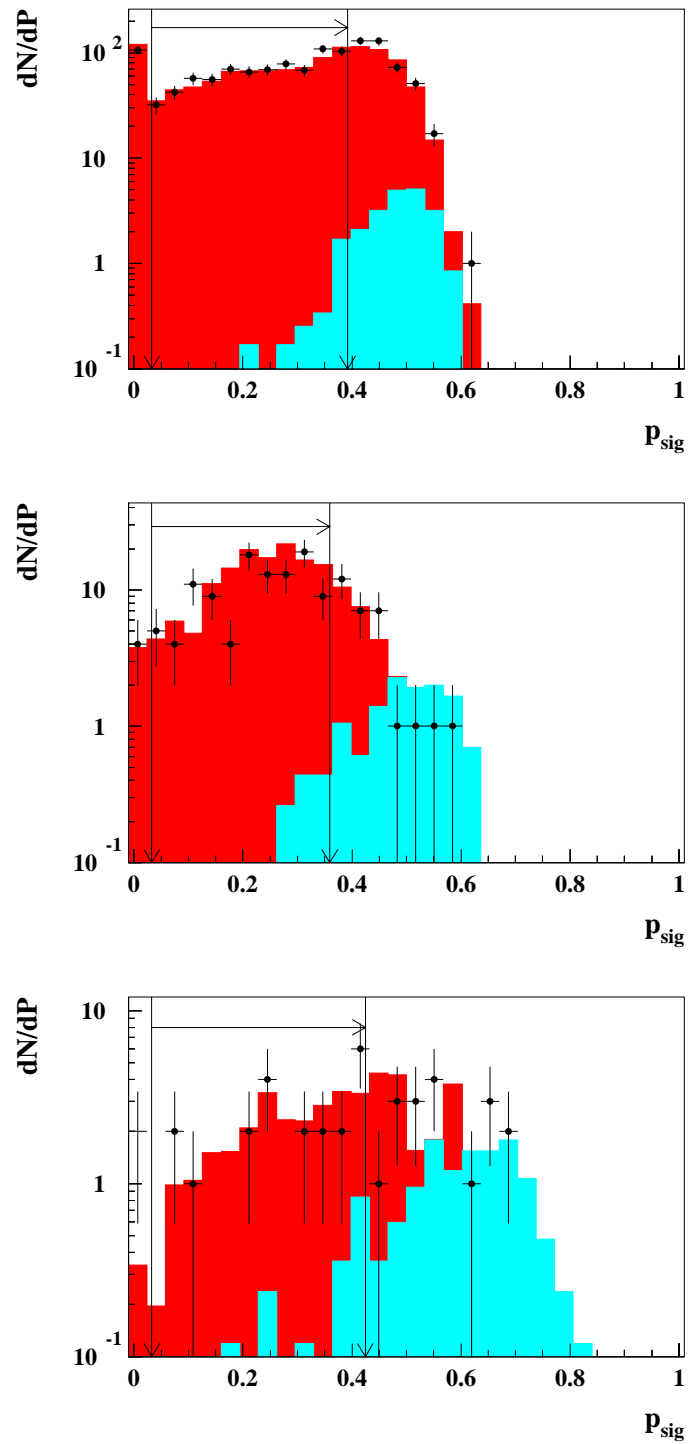
Figure 4.10: Side band region of the final separating variable P_{sig}, used to estimate the systematic errors due to discrepancies between the collected data and simulated reactions.

All these effects were combined within a single check by a direct comparison of collected and simulated event samples with low values of the signal probability P_{sig}. The collected data sample therefore contained mostly background events. To obtain large event samples we applied looser preselection cuts than in the actual analysis (figure 4.10). Relative difference

$$\sigma_{bkg} = \frac{N_{data} - N_{sim}}{N_{data}} \tag{4.18}$$

between the number of measured events N_{data} and appropriate simulated events N_{sim} was used as an estimate of the uncertainty on the background normalisation in the whole P_{sig} region. Obtained values of σ_{bkg} for the three decay channels are summarized in table 4.1. We found that the more preselection cuts are relaxed the larger is the disagreement, therefore we can expect that the estimated disagreement (table 4.1) is very conservative.

Channel	σ_{eff}	σ_{bkg}
hadronic	0.063	0.035
mixed	0.058	0.20
leptonic	0.064	0.15

Table 4.1: Systematic errors on the on the signal selection efficiency P_{sig} and the number of expected background events in all three decay channels.

In the calculation of the $e^+ e^- \rightarrow H^+ H^-$ cross-section upper limits (figure 4.7) and the lower limit on the charged Higgs boson mass (figure 4.8 and equaton 4.15), systematic uncertainties were taken into account by smearing the signal selection efficiencies ε (equation 4.14) and the expected background mean μ_b (equation 4.8). Distributions of the smeared values were taken to be Gaussian. As a conservative estimate, the values of the relative systematic uncertainties σ_{eff} and σ_{bkg} were used as the corresponding standard deviations for the smearing.

5

Conclusions

This thesis describes the search for pair produced charged Higgs boson decay signatures in the LEP electron-positron collisions at centre-of-mass energy $183\,\mathrm{GeV}$. Data were collected by the DELPHI spectrometer in 1997.

Each of the two charged Higgs bosons can decay either hadronically or leptonically, so the events were classified into hadronic, mixed and leptonic decay channel. Signal selection was optimised in each decay channel separately, according to the simulated samples of charged Higgs bosons at different values of the generated Higgs mass. In none of the three channels we observed any statistically significant excess of data over the expected background to be able to claim a discovery of a charged Higgs boson. Instead, we were only able to calculate the upper limit on the charged Higgs boson pair production cross-section in the $\mathrm{e^+e^-}$ collisions as a function of the expected charged Higgs boson mass. By comparing this upper limit to theoretical value of the cross-section as predicted by the PYTHIA event generator, we obtained the lower limit on the Higgs boson mass,

$$m_{\mathrm{H^\pm}} > 53.5\,\mathrm{GeV}/c^2\,(95\%\mathrm{CL}).$$

Other analyses of the charged Higgs boson production and decay in electron positron collisions at LEP collider [53, 54, 55] yield similar upper limits (figure 5.1), with slight variations due to statistical fluctuations, detector specifics and different experimental approaches.

Another type of searches is being conducted at the Fermilab Tevatron [56], where they look for decay signatures of the charged Higgs bosons in decays of pair-produced top quarks. This type of searches does not cover the entire range of the parameter $\tan\beta$, so it can not set a definite lower limit on $m_{\mathrm{H^\pm}}$, since $\tan\beta$ is not known. However, for specific values of the $\tan\beta$ they can set a higher lower limit on $m_{\mathrm{H^\pm}}$ (figure 5.2) than the LEP experiments, thus further constraining the available parameter space for the charged Higgs bosons.
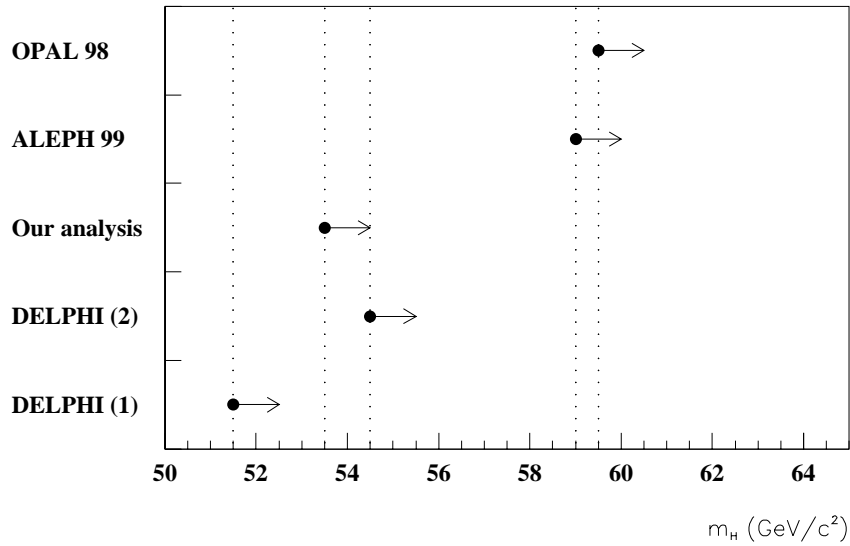
Figure 5.1: A comparison of our limit set on the charged Higgs boson mass with limits of other LEP analyses. Points represent values of the upper limits. All measurements cover the entire range of the parameter $\tan\beta$.
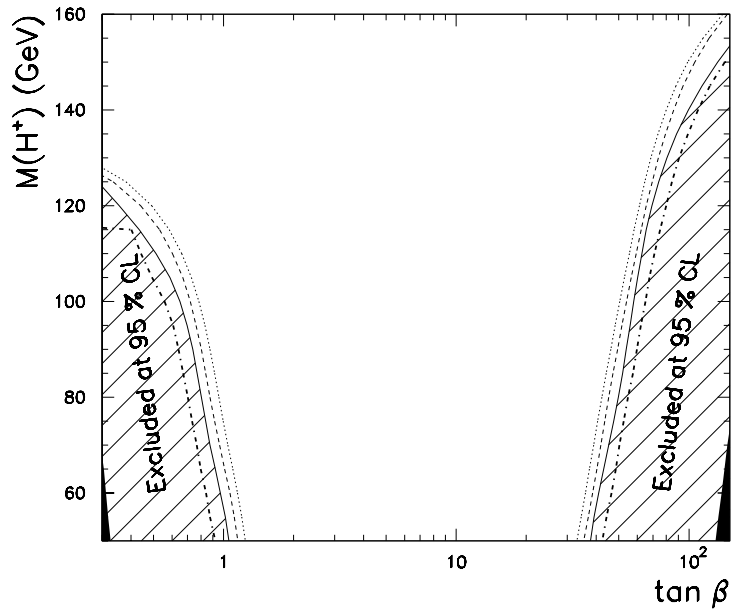
Figure 5.2: D0 Collaboration at Tevatron: The 95% CL exclusion boundaries in the $\left[m_{\mathrm{H}^\pm}, \tan\beta\right]$ plane for $m_t = 175$ GeV, and value of $\sigma(t\bar{t})$ set to 5.5 pb (hatched area, solid lines), 5.0 pb (dashed lines), and 4.5 pb (dotted lines). The thicker dot-dashed lines inside the hatched area represent the exclusion boundaries obtained from a frequentist analysis with $\sigma(t\bar{t}) = 5.5$ pb.

It is expected that the experimental limits on the charged Higgs boson mass will gradually increase with the increased centre-of-mass energy of the LEP collider. However, coming close to the nominal masses of the weak bosons $W^\pm$ and Z^0, the analyses will face serious difficulties due to overwhelming background from $e^+e^- \to W^+W^-$ and $e^+e^- \to Z^0Z^0$ events. The search will than continue at still higher energies at the LHC proton anti-proton collider at CERN, which is expected to provide either a discovery of Higgs bosons or to show that our present understanding of elementary particle physics need be thoroughly reconsidered.

6

Povzetek

Po splošnem prepričanju je najprikladnejši opis fizikalnega sistema tak, ki upošteva njegove simetrije. V primeru osnovnih delcev, kvarkov in leptonov, je mogoče njihove lastnosti opisati z modelom, ki temelji na neabelskih simetrijskih grupah SU(2) in SU(3) ter abelski grupi U(1). Imenujemo jih umeritvene grupe modela. Naš model je umeritveno invarianten, ker se njegova Lagrangeeva gostota ne spreminja pri lokalnih umeritvenih transformacijah. Je tudi renormalizabilen, kar pomeni, da je mogoče neskončnosti pri računih osamiti in odstraniti. Ker se njegove napovedi dobro ujemajo z meritvami, je model, ki temelji na neabelskih simetrijskih grupah, postal osnova splošno priznanega Standardnega modela močnih in elektrošibkih interakcij med osnovnimi delci. Težava takega modela je, da napoveduje brezmasne fermione - kvarke in leptone, prav tako pa tudi brezmasne nosilce interakcij - umeritvene bozone. Ker se to ne sklada z meritvami, saj so bile mase osnovnih delcev eksperimentalno določene, je bilo potrebno model spremeniti tako, da so ti delci pridobili maso. To dosežemo z uvedbo dodatnega potenciala, ki lahko povzroči degeneracijo osnovnega stanja sistema. S tem, da izberemo eno izmed ekvivalentnih osnovnih stanj za fizikalni vakuum, energijska stanja ne bodo več odražala simetrije sistema, čeprav bo Lagrangeeva gostota modela ostala invariantna na lokalne umeritvene transformacije, kar zagotavlja renormalizabilnost modela. Tak primer se imenuje spontani zlom simetrije. V Standardnem modelu nam da perturbativni razvoj okrog izbranega vakuumskega stanja štiri nova skalarna polja. Tri izmed njih interpretiramo kot longitudinalne polarizacije šibkih umeritvenih bozonov $W^{\pm}$ in Z^0, ki na ta način dobijo maso. Četrto polje identificiramo z realnim skalarnim delcem - Higgsovim bozonom. Preostali delci v Standardnem modelu - fermioni - dobijo maso preko sklopitve s Higgsovim bozonom, ki tako igra ključno vlogo pri generaciji mas osnovnih delcev. Na žalost pa model mase samega Higgsovega bozona ne napove, kar otežuje njegovo odkritje. Higgsov bozon je zadnji osnovni delec Standardnega

modela, katerega obstoj še ni eksperimentalno preverjen.

Naslednji korak k globljem razumevanju fizike osnovnih delcev je torej odkritje Higgsovega bozona. Eno izmed eksperimentalnih ocen za njegovo maso so dobili iz meritev elektrošibkih procesov pri trkih elektronov in pozitronov na trkalniku LEP. Ker Standardni model postane renormalizabilen šele, ko za določene procese v perturbativnem razvoju upoštevamo tudi izmenjavo Higgsovih bozonov, bi morale biti nekatere elektrošibke opazljivke občutljive na njihovo maso. S prilagajanjem določena masa Higgsovih bozonov, ki najbolj ustreza vsem meritvam, je okoli $80\,\mathrm{GeV}/c^2$ [6], vendar se moramo zavedati, da so odvisnosti logaritemske in napake ogromne (slika 6.1). Take ocene služijo kot motivacija za nove eksperimente, katerih cilj je njihovo direktno odkritje. Za direktno odkritje je potrebno izmeriti statistično signifikanten signal, rekonstruiran iz njihovih razpadnih produktov. Tako iskanje je omejeno z razpoložljivo težiščno energijo današnjih trkalnikov. Dosedanji poskusi niso uspeli potrditi njihovega obstoja, pač pa so odsotnost signala interpretirali kot spodnjo mejo za njihovo maso in izključili obstoj lažjih Higgsovih bozonov.
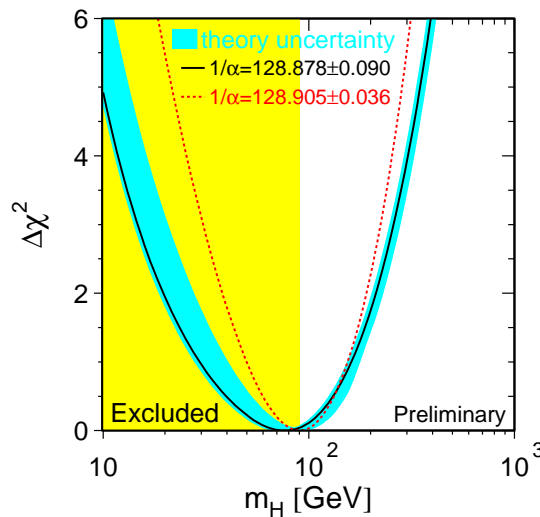
Slika 6.1: Spreminjanje parametra χ^2 pri prilagajanju parametrov Standardnega modela merjenim vrednostim. Prost parameter je masa Higgsovega bozona, ki varira med 10 in $400\,\mathrm{GeV}$. Moder pas predstavlja oceno napake zaradi manjkajočih popravkov višjih redov. Z rumeno barvo osenčeno področje mas je bilo izključeno z meritvami na trkalniku LEP. Rdeča krivulja prikazuje izboljšanje ocene, če bi imeli na voljo natančnejšo meritev parametra $\alpha(m_Z^2)$.

Čeprav je Standardni model uspešna teorija, ki dobro opiše fizikalne procese med osnovnimi delci pri danes dosegljivih energijah, fizikalni principi, ki se skrivajo za obstojem mas osnovnih delcev še niso do konca razjasnjeni. Higgsovi bozoni, kot jih napoveduje Standardni model, še

niso bili eksperimentalno opaženi, zato ne moremo z gotovostjo trditi, da je del Standardnega modela, ki jih opisuje, res pravilen. Eksperimentalno je potrebno preveriti tudi druge možnosti, predvsem nadgradnje Standardnega modela z bolj zapletenim Higgsovim potencialom, ki v nasprotju s Standardnim modelom prinese ne samo eno, ampak več vrst Higgsovih bozonov. Higgsov potencial zdaj ni več funkcija enega samega, ampak dveh dubletov kompleksnih polj, tako da je po podelitvi mas umeritvenim šibkim bozonom na voljo še pet prostostnih stopenj, ki jih interpretiramo kot realne Higgsove bozone. V okviru modela z dvemi dubleti Higgsovih polj sta dva izmed njih nabita delca H^+ in H^-, dva nevtralna skalarna delca H^0 in h^0 ter psevdoskalarni A^0. Cilj doktorskega dela je bil preveriti, ali pri trkih elektronov in pozitronov nastajajo nabiti Higgsovi bozoni in določiti njihovo maso. V primeru odsotnosti signala pri določeni težiščni energiji e^+e^- bi meritev interpretirali kot spodnjo mejo za njihovo maso in do te mase njihov obstoj izključili.
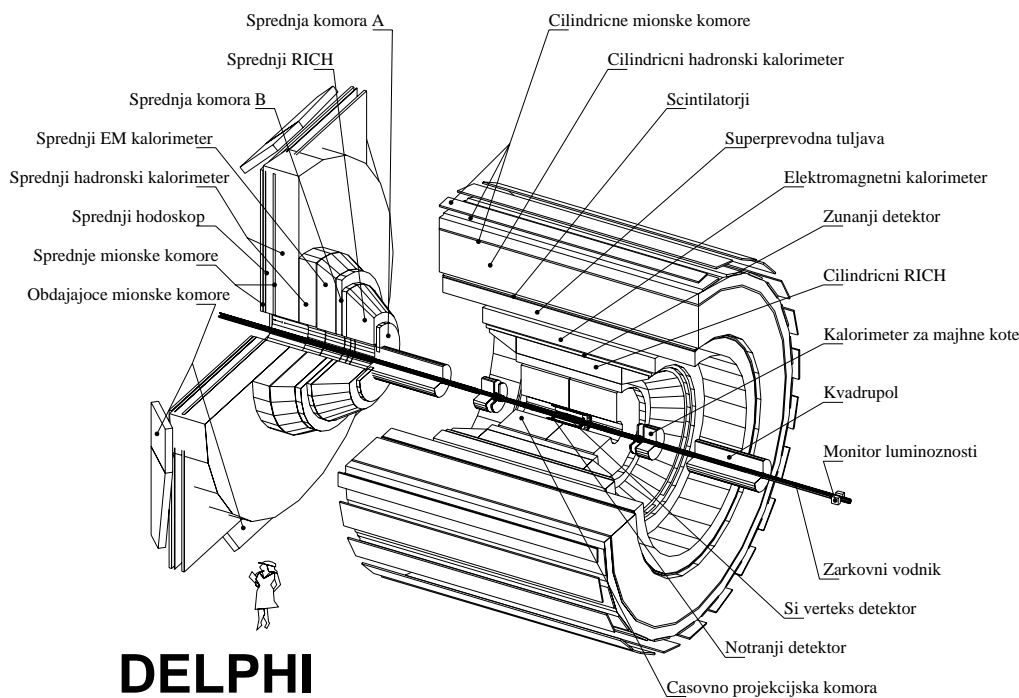

Slika 6.2: Shematski prikaz spektrometra DELPHI.

Meritev je bila izvedena na trkalniku elektronov in pozitronov LEP v evropskem laboratoriju za fiziko osnovnih delcev CERN pri Ženevi. Od leta 1995 naprej težiščno energijo trkalnika

LEP postopoma povečujejo od prvotnih $90\ \mathrm{GeV}$ do predvidenih $200\ \mathrm{GeV}$ v letih 1999 in 2000. S tem se odpirajo nove možnosti za odkritje Higgsovih bozonov, oziroma za izključitev njihovega obstoja do večjih mas kot s predhodnimi meritvami. Podatki so bili zbrani s spektrometrom DELPHI (slika 6.2), enim izmed štirih detektorjev na trkalniku LEP. Spektrometer DELPHI [10] je namenjen sledenju in identifikaciji delcev, ki izhajajo iz trkov e^{+} in e^{-}. Sestavljen je iz velikega števila detektorjev, ki si sledijo od mesta interakcije navzven in sestavljajo cilinder premera 10m. Spektrometer je na obeh koncih zaprt s pokrovoma s podobno strukturo detektorjev kot v cilindričnem delu in tako pokriva praktično ves prostorski kot.

Sledni detektorji, detektorji Čerenkovih obročev in elektromagnetni kalorimeter se nahajajo znotraj superprevodnega solenoida, ki ustvarja homogeno magnetno polje v smeri osi detektorja. Zunaj solenoida so števci časa preleta, hadronski kalorimeter in mionske komore. Pokrovi imajo podobno zgradbo, le da so ob žarkovni cevi nameščeni še monitorji luminoznosti.

Nastanek nabitih Higgsovih bozonov na trkalniku LEP poteka preko izmenjave fotona ali nevtralnega šibkega bozona Z^{0} (slika 6.3).
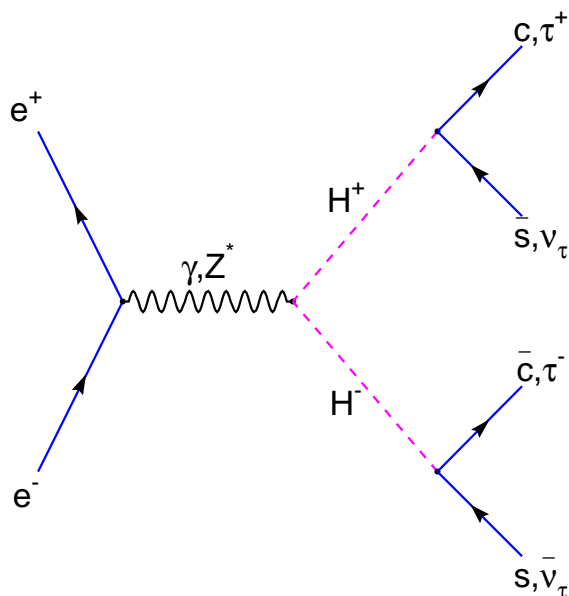
Slika 6.3: Feynmanovi diagrami v drevesnem redu za nastanek in razpad nabitih Higgsovih bozonov v okviru razširitve Standardnega modela z dvema dubletoma Higgsovih polj.

Reakcija je bila simulirana z generatorjem dogodkov PYTHIA 5.7 [36], ki poleg drevesnega reda upošteva tudi popravke višjih redov. Nabiti Higgsovi bozoni večinoma razpadejo v par fermionov z največjo kinematično še dosegljivo maso, $\mathrm{H}^{+} \rightarrow \tau^{+}\nu_{\tau}$ ali $c\bar{s}$. Končna eksperi-

mentalno opazljiva stanja so torej $\tau^+\nu_\tau\tau^-\bar{\nu}_\tau$, c$\bar{\text{s}}\tau^+\nu_\tau$ in c$\bar{\text{s}}$c$\bar{\text{s}}$. V nadalnjem tekstu so označena kot leptonski, mešani in hadronski razpadni kanal. Katero izmed stanj bo prevladujoče, je odvisno od parametra $\tan\beta$, razmerja med pričakovanima vrednostima vakuumskih stanj obeh dubletov Higgsovih polj. Ker je vrednost $\tan\beta$ neznana, je treba eksperimentalno preveriti vse razpadne možnosti. Pri anihilaciji elektronov in pozitronov potekajo tudi druge reakcije, ki pri naši meritvi predstavljajo ozadje. Sipalni presek za nastanek para nabitih Higgsovih bozonov je približno dva reda velikosti manjši od presekov za ozadje.

V hadronskem kanalu pričakujemo signal kot štiri dobro ločene hadronske pljuske z rekonstruirano energijo razpadnih produktov blizu težiščne energije prvotnega elektrona in pozitrona. Reakcije, ki predstavljajo večino ozadja, so hadronski procesi $\text{e}^+\text{e}^- \to \text{q}\bar{\text{q}}(\gamma)$ in razpadi nabitih šibkih bozonov W^+W^-. Tako $\text{e}^+\text{e}^- \to \text{q}\bar{\text{q}}$ z dvema detektiranima hadronskima pljuskoma kot $\text{e}^+\text{e}^- \to \text{q}\bar{\text{q}}\gamma$, kjer ima foton zelo majhen polarni kot glede na žarkovno cev, lahko zavrnemo z zahtevami o določeni topologiji zaznanega dogodka. Ozadja, ki izvira iz hadronskih razpadov $\text{W}^\pm$, se lahko deloma znebimo zaradi drugačne kotne porazdelitve nastalih bozonov $\text{W}^\pm$, kot pri $\text{H}^\pm$. Še posebej pri masah nabitih Higgsovih bozonov blizu m_W pa se ozadja zaradi $\text{W}^\pm$ ne da v celoti znebiti.

V mešanem kanalu eden izmed nabitih Higgsovih bozonov razpade v par kvarkov c$\bar{\text{s}}$, drugi pa v par leptonov $\tau^+\nu_\tau$. V tem primeru detektiramo dva hadronska pljuska, dodatno pa še en šibek pljusk oziroma elektron ali mion, ki so razpadni produkti leptona τ. Detektirana energija bo manjša od težiščne energije e^+e^-, ker del energije odnesejo nevtrini. Glavni viri ozadja so reakcije $\text{e}^+\text{e}^- \to \text{q}\bar{\text{q}}(\gamma)$ in razpadi $\text{W}^\pm$. Prve lahko zavrnemo, ker praktično ni manjkajoče energije kot v primeru signala, druge pa na podlagi drugačne porazdelitve težiščne energije razpada.

V leptonskem kanalu oba nabita Higgsova bozona razpadeta v par $\tau\nu$. Ti razpadi imajo majhno število razpadnih produktov in rekonstruirano energijo vseh delcev dosti manjšo od težiščne energije pri trku e^+e^-. Vsak izmed leptonov τ razpade hadronsko v ozek pljusk ali leptonsko v elektron oziroma mion in ustrezne nevtrine. Nastanejo vsaj štirje nevtrini, ki odnesejo velik del energije in ostanejo nedetektirani. Zaradi tega v leptonskem kanalu ni mogoče rekonstruirati mase Higgsovih bozonov iz razpadnih produktov. Glavno ozadje so dvofotonske reakcije $\text{e}^+\text{e}^- \to \gamma\gamma$, ki pa se jih lahko znebimo zaradi majhne prečne gibalne količine razpadnih produktov glede na žarkovno os. Najteže je spet zavrniti ozadje, ki zvira iz razpadov $\text{W}^\pm$.
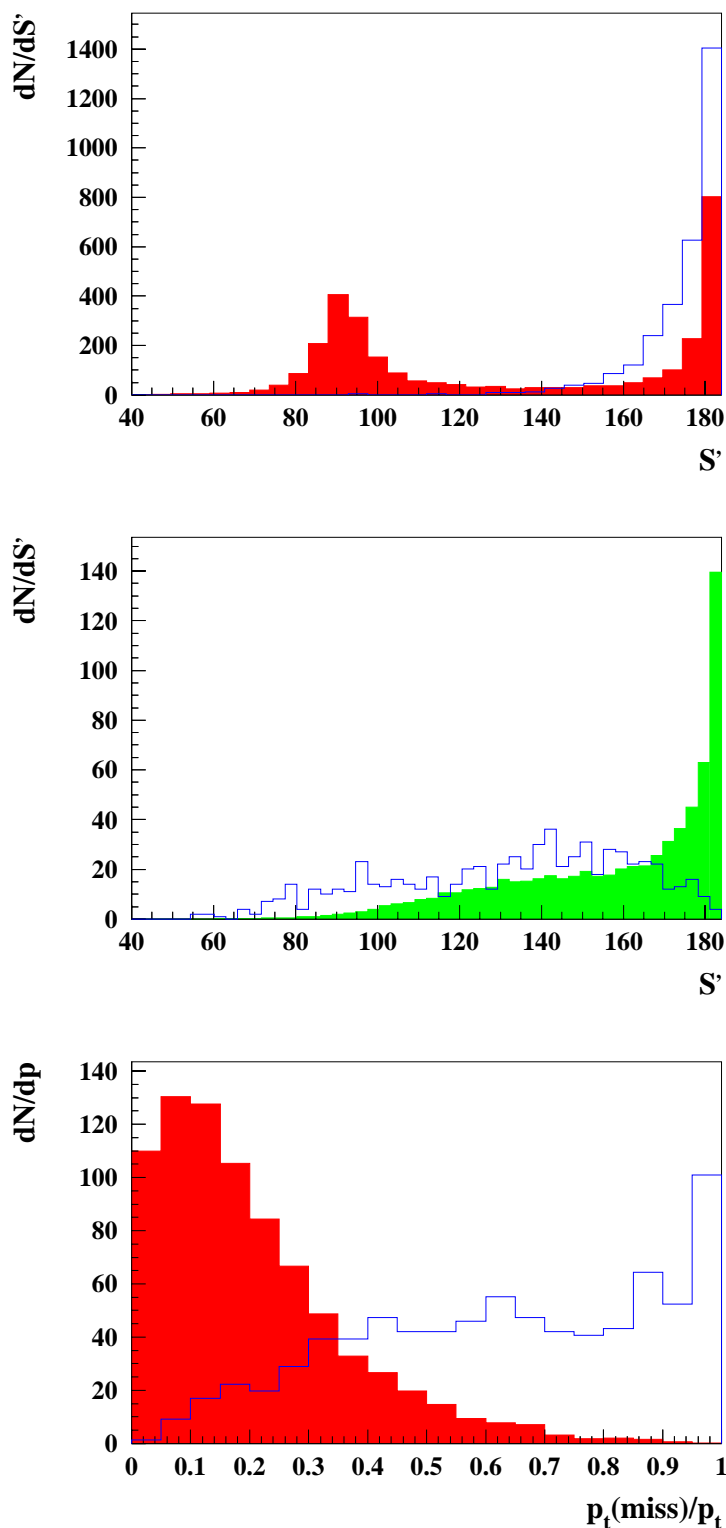
Slika 6.4: Porazdelitev efektivne težiščne energije, $s\prime$, kot primer uporabljene kinematične spremenljivke za ločevanje signala od ozadja v hadronskem (zgornja slika) in mešanem kanalu (sredina). Na spodnji sliki je porazdelitev skupne prečne gibalne količine vseh delcev v dogodku glede na os dogodka kot primer uporabljene kinematične spremenljivke za ločevanje signala od ozadja v leptonskem kanalu. S polnim histogramom je označeno simulirano ozadje, z odprtim histogramom pa simuliran signal. Za lažjo primerjavo oblike porazdelitev sta bila signal in ozadje normirana na enako število dogodkov.

Električne signale, ki so jih produkti anihilacije e^+e^- povzročili v raznih detektorjih spektrometra DELPHI, smo najprej obdelali s standardnim programom za dekodiranje signalov in izračun sledi delcev DELANA [38]. Vsako tako obdelano anihilacijo e^+ in e^- imenujemo dogodek. Od nabitih delcev v dogodku zahtevamo dolžino rekonstruirane sledi nad 15cm in za nevtralne delce, da so v kalorimetrih pustili nad $0.5\,\mathrm{GeV}$ energije. Glede na tri pričakovane razpadne načine para nabitih Higgsovih bozonov H^+H^- nato dogodke ločimo v tri skupine: hadronski, mešani in leptonski razpadni kanal. Izbrane delce v dogodku razvrstimo v pljuske s pomočjo algoritma LUCLUS [36]. V hadronskem kanalu zahtevamo štiri, v mešanem tri in v leptonskem kanalu dva pljuska. Dogodke nato obravnavamo v vsakem razpadnem kanalu posebej. Sprejeti so v nadaljno obdelavo, če zadostijo blagim preselekcijskim kriterijem na številu nabitih delcev, njihovi energiji in v razpadnih kanalih z leptoni smeri rekonstruiranih pljuskov.

Ločevanje signala od reakcij, ki predstavljajo ozadje, smo optimizirali s pomočjo simuliranih vzorcev razpadov H^+H^- in ozadja v vsakem razpadnem kanalu posebej. Signal in QCD ozadje so bili generirani z generatorjem PYTHIA 5.7, ozadje iz razpadov W^+W^- in Z^0Z^0 pa z generatorjem EXCALIBUR [43]. Vzorce signala smo generirali pri petih različnih masah nabitih Higgsovih bozonov med 45 in $65\,\mathrm{GeV}/c^2$, v leptonskem kanalu pa pri šestih masah med 45 in $70\,\mathrm{GeV}/c^2$. Generirane reakcije smo obdelali z računalniško simulacijo spektrometra DELPHI s programom DELSIM [42]. Na ta način smo dobili signale iz simuliranih detektorjev, ki jih nato dekodiramo in rekonstruiramo na enak način in z istimi programi kot dejanske meritve. V vsakem izmed treh razpadnih kanalov smo izbrali okoli deset kinematičnih spremenljivk, ki dobro ločujejo posamezne vrste ozadja v danem kanalu od iskanega signala. Po ena spremenljivka za vsak kanal je kot primer predstavljena na sliki 6.4. Vse izbrane spremenljivke v danem razpadnem kanalu smo nato kombinirali v verjetnost P_{sig}, da gre pri danem dogodku za signal. V hadronskem in mešanem kanalu, kjer dobimo iz fragmentacije primarnih kvarkov hadronske pljuske, smo poleg kinematičnih spremenljivk kot ločevalno spremenljivko uporabili tudi označevanje okusa primarnih kvarkov. Pljuske, ki izvirajo iz kvarkov b ali c (pri hadronskem razpadu $H^\pm$) lahko namreč ločimo od pljuskov iz lahkih kvarkov zaradi večjega življenjskega časa hadronov s težkimi kvarki. Ta lastnost se odraža tako, da sledi delcev iz takega pljuska ne kažejo v mesto interakcije e^+e^-, ampak v tako imenovani sekundarni verteks, mesto razpada mezona, ki vsebuje težki kvark. V naši analizi smo uporabili paket AABTAG [45] za označevanje pljuskov, ki izvirajo iz kvarkov c (slika 6.5). Poleg tega smo uporabili tudi informacijo o vrsti nabitega delca z največjo gibalno količino v pljusku iz detektorja Čerenkovih obročev. Če je tak delec kaon, je zelo verjetno, da vsebuje primarni kvark s ali kvark s iz razpada $c \to s$.
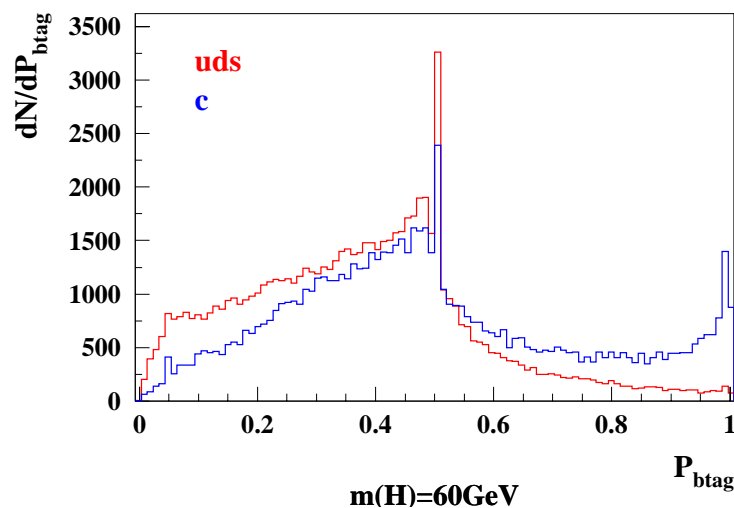
Slika 6.5: Porazdelitev identifikacijske spremenljivke za ločevanje hadronskih pljuskov, ki izvirajo iz fragmentacije kvarkov c in kvarkov s. Histograma predstavljata simulirane dogodke.

V primeru, da pričakujemo maso nabitih Higgsovih bozonov pod $70 \, \text{GeV}/c^2$, lahko v mešanem in hadronskem razpadnem kanalu dodatno izboljšamo izkoristek ločevanja signala od ozadja, če upoštevamo še informacijo o rekonstruirani invariantni masi parov hadronskih pljuskov. Rekonstruirano invariantno maso lahko namreč identificiramo z iskano maso nabitega Higgsovega bozona. V vzorcu simuliranih Higgsovih bozonov vidimo rekunstruirano invariantno maso para pljuskov kot značilen vrh Gaussove oblike pri generirani masi $m_{\text{H}^\pm}$. Ker iščemo Higgsove bozone s sicer neznano, vendar natanko določeno pričakovano maso, se pri analizi lahko omejimo le na dogodke z rekonstruirano invariantno maso v nekem intervalu okoli pričakovane mase, ostale pa lahko zavržemo. Na ta način se znebimo predvsem reakcij, kjer nastaneta nabita šibka bozona W^+W^- in ki se sicer od iskanih razpadov Higgsovih bozonov kinematično le malo razlikujejo. Invariantna masa para pljuskov ima v tem primeru vrh pri masi $\text{W}^\pm$, to je pri $80 \, \text{GeV}/c^2$ [32]. Širino intervala invariantne mase, ki nam da največjo vrednost produkta izkoristka izbire in čistosti izbranega vzorca smo ocenili za primer, ko je na danem intervalu ozadje konstantno, signal Gaussove oblike in je število dogodkov iskanega signala primerljivo ali manjše številu dogodkov ozadja. Ker je masa nabitih Higgsovih bozonov iskana količina, smo optimizirali ločevanje signala od ozadja za cel spekter možnih mas $m_{\text{H}^\pm}$. S pomočjo simuliranih vzorcev signala smo pri vsakem vzorcu posebej določili vrednost reza na končni spremenljivki P_{sig}, ki da največjo vrednost produkta izkoristka izbire in čistosti izbranega vzorca. Upoštevali smo tudi, da je eksperimentalna širina vrha invariantne mase dveh pljuskov in s tem širina intervala okrog generirane mase Higgsovega bozona odvisna od mase same. Izkoristek izbire signala pri masah, kjer ni bilo simuliranega vzorca signala, smo dobili z

linearno interpolacijo med simuliranimi vrednostmi.

Opisano selekcijo dogodkov smo nato uporabili pri analizi meritev spektrometra DELPHI. V vsakem razpadnem kanalu posebej smo izračunali verjetnost za signal P_{sig} za mase nabitih Higgsovih bozonov od 43 do $72\,\mathrm{GeV}/c^2$ v korakih po $1\,\mathrm{GeV}/c^2$.

Pri interpretaciji meritev smo se držali napotkov skupine Particle Data Group [32] o klasični statistični obravnavi majhnih signalov. Za vsako hipotetično maso nabitih Higgsovih bozonov smo pri danem številu izmerjenih dogodkov izračunali številski interval, znotraj katerega s 95% verjetnostjo leži število razpadov nabitih Higgsovih bozonov α v izmerjenih podatkih. Ker pri nobeni izmed uporabljenih vrednosti za $m_{\mathrm{H}\pm}$ nismo mogli izključiti vrednosti nič iz omenjenega intervala, smo se raje kot za izračun intervalov zaupanja odločili za izračun zgornjih mej [51]. Analogno kot pri izračunu intervala zaupanja smo določili zgornjo mejo, pod katero je s 95% stopnjo zanesljivosti število vseh dogodkov v merjenem vzorcu, ki jih pripisujemo signalu.

Bolj kot zgornje meje za število dogodkov signala v posameznem razpadnem kanalu nas zanima zgornja meja za presek iskane reakcije, $\mathrm{e^+e^-} \to \mathrm{H^+H^-}$. Ne moremo je eksplicitno izračunati, ker razvejitvena razmerja pri razpadu nabitih Higgsovih bozonov niso znana. Ob predpostavki, da $\mathrm{H}^{\pm}$ razpade bodisi v par kvarkov $\mathrm{c\bar{s}}$ bodisi v par $\tau^+\nu_\tau$, lahko obe razvejitveni razmerji parametriziramo z eno samo spremenljivko r. Z analizo meritev v posameznih razpadnih kanalih dobimo zgornje meje za presek,

$$\sigma_i(\mathrm{e^+e^-} \to \mathrm{H^+H^-})_{UL} = \frac{N_i(m_{\mathrm{H}\pm}, r; \epsilon_i)}{L},$$

kjer indeks $i = 1, 2, 3$ označuje posamezni razpadni kanal. N_i so zgornje meje za število dogodkov signala pri določeni masi v danem razpadnem kanalu, ϵ_i so izkoristki izbire, L pa je integrirana luminoznost analiziranih meritev. Zgornje meje za vse tri kanale so predstavljene na sliki (6.6).

Glavni rezultat analize je spodnja meja za maso nabitih Higgsovih bozonov, pod katero lahko njihov obstoj izključimo. Izračunamo jo tako, da kombiniramo meritve iz vseh treh razpadnih kanalov v zgornjo mejo za presek za vse možne vrednosti razvejitvenega parametra r. Na ta način dobimo dvodimenzionalno porazdelitev zgornje meje za presek kot funkcijo $m_{\mathrm{H}\pm}$ in parametra r. Izmerjeno zgornjo mejo za presek nato primerjamo z izračunanim presekom, ki ga napove model. Če je pri dani masi $m_{\mathrm{H}\pm}$ izmerjena vrednost $\sigma(\mathrm{e^+e^-} \to \mathrm{H^+H^-})_{UL}$ manjša od napovedanega preseka za vse možne vrednosti razvejitvenega razmerja r, potem lahko s stopnjo zanesljivosti $1 - \epsilon$ izključimo možnost obstoja nabitih Higgsovih bozonov pri tej masi. Izračunana spodnja meja za $m_{\mathrm{H}\pm}$ je seveda močno odvisna od izbranega modela, saj je pogoj za izključitev obstoja $\mathrm{H}^{\pm}$ direktno odvisen od napovedanega preseka za $\mathrm{e^+e^-} \to \mathrm{H^+H^-}$.
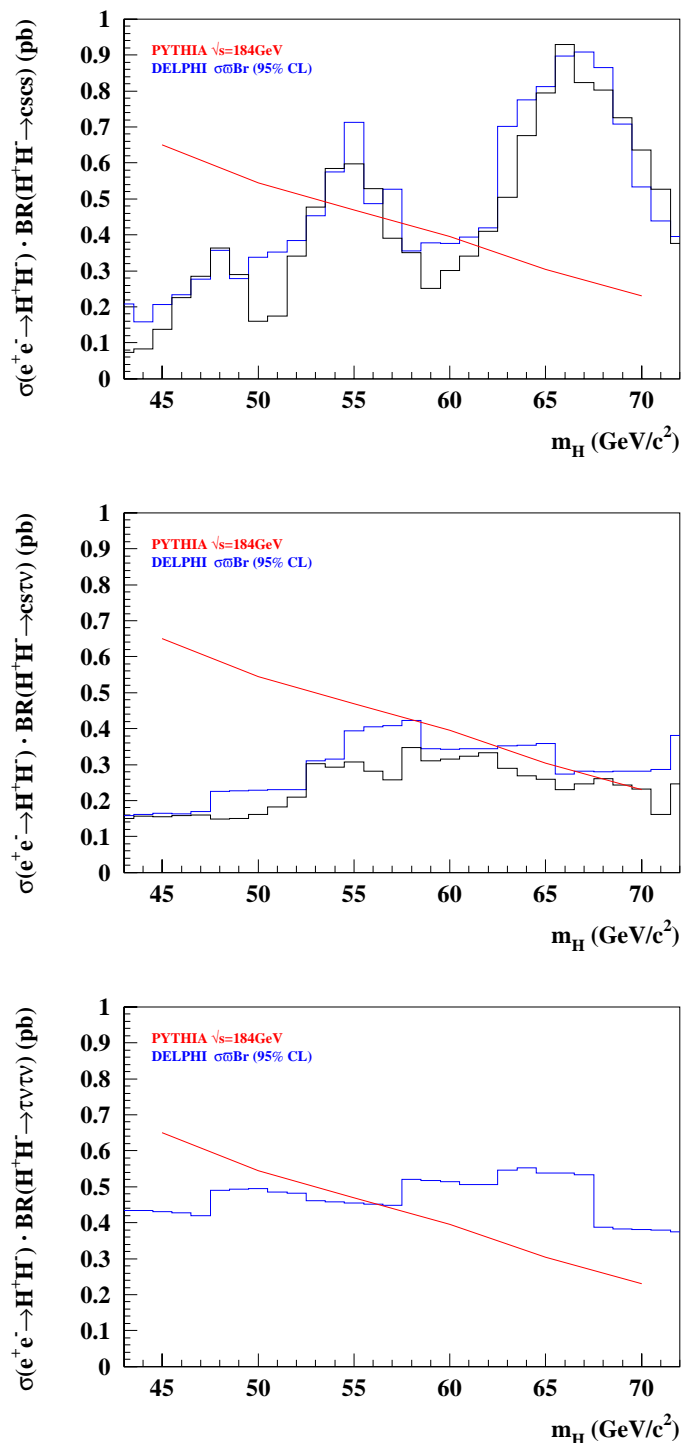
Slika 6.6: Zgornje meje preseka za reakcijo $e^+e^- \to H^+H^-$, dobljene pri analizi hadronskega (zgornja slika), mešanega (sredina) in leptonskega kanala (spodnja slika). Izmerjena zgornja meja za presek je označena z modro, z generatorjem PYTHIA napovedana vrednost pa z rdečo barvo. S črno barvo je označena zgornja meja za presek, kjer smo dodatno upoštevali informacijo o invariantni masi pljuskov. Pri napovedi smo za vsak razpadni kanal privzeli, da je razpadno razmerje ena.
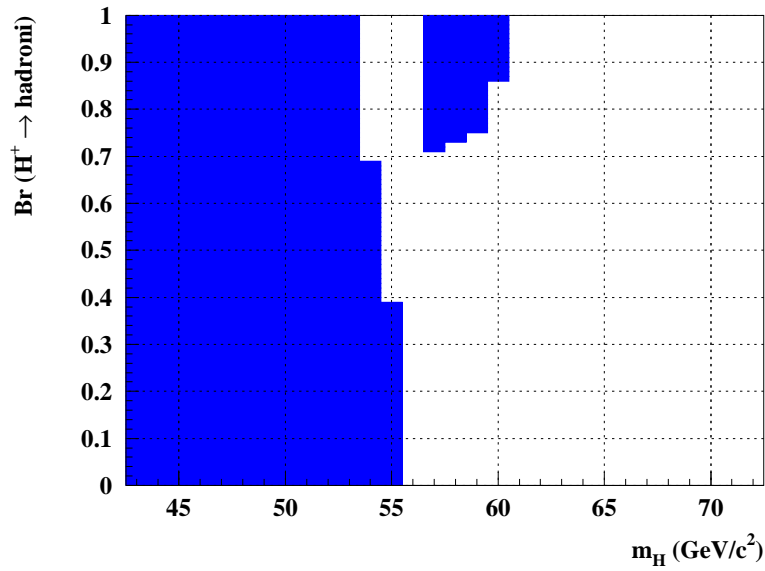
Slika 6.7: Izključeno območje za obstoj nabitih Higgsovih bozonov kot funkcija hadronskega razvejitvenega razmerja, $\mathrm{Br}(\mathrm{H} \to \mathrm{hadroni}$, in mase nabitih Higgsovih bozonov. Obstoj $\mathrm{H}^{\pm}$ je v modrem področju izključen s 95% verjetnostjo.

Rezultati primerjave izmerjene zgornje meje in napovedanega preseka so prikazani na sliki (6.7). Spodnja meja za maso nabitih Higgsovih bozonov, ki je rezultat te metode, je $m_{\mathrm{H}^{\pm}} > 53.5\,\mathrm{GeV}/c^2$ s 95% stopnjo zanesljivosti.

Pričakujemo, da največje sistematske napake pri meritvi nastopajo iz dveh razlogov: nepopolnega opisa fragmentacije kvarkov in gluonov in odzivov detektorja na simulirane dogodke ter nenatančnega poznavanja presekov za različne reakcije, npr. dvofotonske reakcije, ki pri meritvi predstavljajo ozadje. Namesto da bi ocenjevali prispevek vsakega procesa posebej, smo raje ocenili sistematsko napako na podlagi dveh inkluzivnih testov, kjer vsak od njiju zajame več možnih prispevkov.

Prvi test zajema oceno napak pri ločevanju signala od ozadja. Ta izvira iz neujemanja simuliranih kinematičnih porazdelitev, ki jih uporabljamo za separacijo, s porazdelitvami v dejanskih meritvah. Največji prispevek pričakujemo od modeliranja fragmentacijskih procesov in odzivov detektorja na simulirane reakcije. Vse te prispevke smo skušali oceniti s pomočjo reakcij pri težiščni energiji $91\,\mathrm{GeV}$, kjer pri anihilaciji elektrona in pozitrona nastane nevtralni šibki bozon Z^0. Če združimo po dva razpada Z^0 v en dogodek, lahko namreč zadovoljivo reproduciramo topologijo razpada $\mathrm{H}^+\mathrm{H}^-$. Postopek združevanja razpadov Z^0 smo ponovili za merjen in simuliran vzorec dogodkov v vsakem razpadnem kanalu posebej. Nadaljna analiza tako dobljenih dogodkov je bila enaka kot analiza dejanskih meritev pri težiščni energiji $184\,\mathrm{GeV}$.

Dobili smo šest verjetnosti, tri za simulirane sestavljene dogodke in tri za merjene sestavljene dogodke. Po rezu na verjetnosti pri vrednosti, dobljeni iz optimizacije reza z vzorcem nabitih Higgsovih bozonov in ozadja pri težiščni energiji $184\,\mathrm{GeV}$, smo primerjali simulirane dogodke z izmerjenimi. Relativna razlika med deležema sprejetih simuliranih in merjenih dogodkov nam je služila kot ocena za sistematsko napako izkoristka izbire signala,

$$\sigma_{eff} = \frac{\varepsilon_{sim} - \varepsilon_{data}}{\varepsilon_{sim}}.$$

Sistematske napake pri opisu ozadja v glavnem izvirajo iz slabo poznanih presekov za posamezne reakcije in modeliranja odzivov detektorja na simulirane podatke. Vse te lastnosti smo upoštevali tako, da smo primerjali merjene in simulirane dogodke z nizkimi vrednostmi končne verjetnosti za signal P_{sig}. Zgornja meja intervala za P_{sig} je bila izbrana tako, da so merjeni dogodki vsebovali največ 10% vsega pričakakovanega signala, spodnja pa tako, da je bila statistična napaka na številu izbranih dogodkov manjša od 5%. Relativna razlika med številom merjenih in simuliranih dogodkov s P_{sig} v izbranem intervalu,

$$\sigma_{bkg} = \frac{N_{data} - N_{sim}}{N_{data}},$$

nam je služila za oceno sistematske napake pri vseh vrednostih P_{sig}.

Sistematske napake smo pri izračunu zgornje meje za reakcijo $e^{+}e^{-} \rightarrow H^{+}H^{-}$ in pri določitvi spodnje meje za maso nabitih Higgsovih bozonov upoštevali tako, da smo namesto verjetnosti izbire signala ε in pričakovanega števila ozadja μ_b uporabljali po Gaussovi porazdelitvi razmazane vrednosti.

To delo predstavlja majhen del v celoti eksperimentalnih prizadevanj, s trenutno dosegljivimi eksperimentalnimi sredstvi pridobiti nova spoznanja o fiziki Higgsovih bozonov. V večini fizikalnih modelov, ki opisujejo fiziko osnovnih delcev, ena ali več vrst Higgsovih bozonov igra ključno vlogo v razlagi obstoja mas vseh osnovnih delcev v naravi. V razpadnih produktih trkov elektronov in pozitronov pri težiščni energiji $184\,\mathrm{GeV}$ v trkalniku LEP smo s spektrometrom DELPHI iskali take dogodke, ki bi jih lahko pripisali razpadom nabitih Higgsovih bozonov. Meritve v vseh pričakovanih razpadnih kanalih kažejo, da ni statistično signifikantnega signala, zato smo se odločili za izračun zgornjih mej za produkcijski presek parov $H^{+}H^{-}$ v trkih e^{+} in e^{-}. Glavni rezultat meritve, spodnja meja za maso nabitih Higgsovih bozonov, do katere lahko s 95% stopnjo zanesljivosti izključimo njihov obstoj, znaša

$$m_{\mathrm{H}^{\pm}} > 53.5\,\mathrm{GeV}/c^2 \ (95\%\mathrm{CL}).$$

Druge analize razpadov nabitih Higgsovih bozonov, nastalih pri trkih elektronov in pozitronov v trkalniku LEP [53, 54, 55] dajo podobne vrednosti spodnjih mej za $m_{\mathrm{H}^{\pm}}$ (slika 6.8).
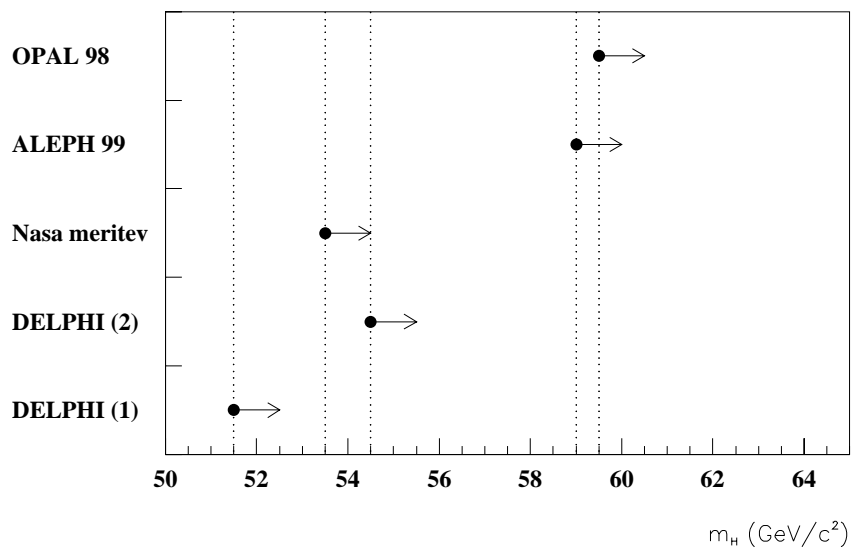
Slika 6.8: Primerjava naše spodnje meje za maso nabitih Higgsovih bozonov z mejami, ki so jih dosegle druge analize eksperimentov na trkalniku LEP. mass with limits of other LEP analyses. Točke predstavljajo vrednosti spodnjih mej. Vse meritve zajemajo celotno območje parametra $\tan\beta$.
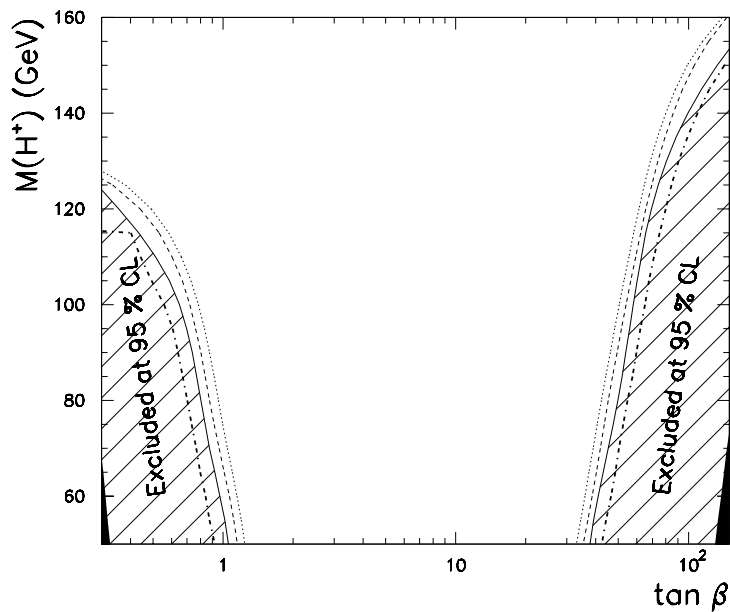
Slika 6.9: Kolaboracija D0: Iskanje razpadnih produktov nabitih Higgsovih bozonov pri razpadih k-varkov t. V šrafiranem področju ravnine $\left[m_{\mathrm{H}^\pm}, \tan\beta\right]$ je za $m_t = 175\,\mathrm{GeV}/c^2$ in $\sigma(t\bar{t}) = 5.5$ pb obstoj nabitih Higgsovih bozonov izključen s 95% stopnjo zanesljivosti.

Razlike lahko pripišemo statističnim fluktuacijam, razlikam med detektorji in različnim eksperimentalnim pristopom.

Drugačna vrsta analize poteka na pospeševalniku Tevatron [56], kjer iščejo značilne razpade nabitih Higgsovih bozonov v razpadih kvarkov t. Ker niso občutljivi na celotno območje parametra $\tan\beta$, ne morejo izmeriti spodnje meje na masi $m_{H^\pm}$, za specifične vrednosti $\tan\beta$ pa je njihova občutljivost boljša od eksperimentov na trkalniku LEP (slika 6.9). Tako lahko dodatno omejijo možne konfiguracije parametrov v izbranem modelu.

Če ne bo prišlo do odkritja, lahko pričakujemo, da se bo s povečanjem težiščne energije trkalnika LEP spodnja meja za $m_{H^\pm}$ še povišala. Ker pa se bo močno približala masam šibkih bozonov $W^\pm$ in Z^0, bodo analize naletele na resne težave zaradi ogromne količine ozadja iz reakcij $e^+e^- \to W^+W^-$ in $e^+e^- \to Z^0Z^0$. Iskanje nabitih Higgsovih bozonov se bo nato nadaljevalo na trkalniku protonov in antiprotonov LHC, od katerega se pričakuje bodisi odkritje Higgsovih bozonov, bodisi močan namig, da je fundamentalno razumevanje obstoja mas osnovnih delcev v slepi ulici.

References

[1] S. Weinberg, *The Quantum Theory of Fields Vol. I and II*, Cambridge Univ. Press, Cambridge (1995, 1996).

[2] R. Mills, Phys. Rev. **96** (1954) 191.

[3] G. t'Hooft, Nucl. Phys. **B35** (1971) 167.

[4] J. Goldstone, A. Salam, S. Weinberg, Phys. Rev. **127** (1962).

[5] P.W. Higgs, Phys. Lett **12** (1964) 132, Phys. Rev. Lett. **13** (1964) 508, Phys. Rev. **145** (1966) 1156.

[6] D. Karlen, Electroweak Review Writeup, ICHEP 98, Vancouver (1998).

[7] K.H. Kissler, SPS and LEP status report, CERN SL 98-053 (1998).

[8] S. Myers, LEP2: Present and future performance and limitations, CERN SL 97-022 (1997).

[9] K. Hübner, LEP2 present and future performance and limitations, CERN SL 98-043 (1998).

[10] DELPHI Collaboration, P. Abreu *et al.*, Nucl. Instr. Meth. **A303** (1991) 233-376.

[11] DELPHI Collaboration, P. Abreu *et al.*, Nucl. Instr. Meth. **A378** (1996) 57-100.

[12] Y. Sacquin, The DELPHI time projection chamber, Nucl. Instr. and Meth. **A323** 209-212 (1992).

[13] P. Chochula *et al.* The DELPHI Silicon Tracker at LEP 2, Nucl. Instr. Meth. **A412** (1998) 304-328.

[14] V. Chabaud *et al.* The DELPHI Silicon Strip Microvertex Detector with Double Sided Readout, Nucl. Instr. and Meth. **A368** 314 (1996).

[15] W. de Boer *et al.* Tests of the first Pixel detectors for the DELPHI upgrade, DELPHI 95-118 TRACK 82 (1995).

[16] P. Chochula *et al.* Results from beam tests with VFT ministrip prototypes, DELPHI 94-44 TRACK 78 (1994).

[17] A. Cattai *et al.* Equalization of the Readout Channels of the HPC by Means of Radioactive Gas, internal note, DELPHI 93-115 CAL-105 (1993).

[18] A. De Min *et al.*, Performance of the HPC Calorimeter in DELPHI, CERN PPE 95-04 (1995).

[19] M. Feindt *et al.*, ELEPHANT Reference Manual, internal note, DELPHI 96-82 PROG-217 (1996).

[20] C. Fabjan, Calorimetry in High Energy Physics, in *Experimental Techniques in High Energy Physics*, T. Ferbel *ed.*, Addison-Wesley Publishing Co., 257 (1987).

[21] W. Adam *et al.*, Analysis Techniques for the DELPHI Ring Imageing Cherenkov Detector, DELPHI 94-112 PHYS-429 (1994).

[22] DELPHI Collaboration, DELSIM, DELPHI event generation and detector simulation - Reference Manual, DELPHI Note 89-68 PROG 143 (1989).

[23] W.R. Leo, *Techniques for Nuclear and Particle Physics Experiments*, Springer-Verlag, Berlin (1987).

[24] S. Weinberg, Phys. Rev. Lett. **19** (1967); A. Salam, Proc. 8th Nobel Symposium, *ed.* N. Svartholm (1968).

[25] G. Altarelli, R. Kleiss, C. Verzognassi, Z Physics at LEP 1, CERN-89-08 (1989).

[26] DELPHI Collaboration, P. Abreu *et al.*, Eur. Phys. J. **C2** (1998).

[27] OPAL Collaboration, M. Vincter *et al.*, Proc. 11th Lake Louise Winter Institute, A. Astbury, B. A. Campbell, F. C. Khanna and J. L. Pinfold *ed.*, World Sci., Singapore, (1997).

[28] N. G. Deshpade, E. Ma, Phys. Rev. **D18** (1978).

[29] H. Georgi, Hadronic Journal 1 (1978).

[30] E. Witten, Nucl. Phys. **B231** (1984); S. Dimopoulos, H. Georgi, Nucl. Phys. **B193** (1981).

[31] J. Wess, J. Bagger, *Supersymmetry and Supergravity*, Princeton Univ. Press, New Jersey (1991).

[32] C. Caso *et al.*, Review of Particle Physics, Eur. Phys. J. **C 3** (1998).

[33] J.F. Gunion, H.E. Haber, G.L. Kane, S. Dawson, *The Higgs Hunter's Guide*, Addison-Wesley, New York (1990).

[34] S Glashow, S. Weinberg, Phys. Rev. **D15** (1977) 1958.

[35] G. Altarelli, T. Sjöstrand, F. Zwirner, Physics at LEP 2, CERN-96-01 (1996).

[36] T.Sjöstrand, *PYTHIA 5.7 / JETSET 7.4*, CERN-TH.7112/93 (1993).

[37] M. Kobayashi, T. Maskawa, Prog. Theor. Phys. **49**, 652, (1973).

[38] DELPHI Collaboration, DELPHI Data Analysis Program (DELANA) User's Guide, DELPHI Note 89-44 PROG 137 (1989).

[39] R. Chierici, C. Parkes and A. Tonazzo, WWANA - A standard package for W analysis, DELPHI Note 96-128 PROG 218 (1996).

[40] N.Kjaer, R.Möller, *Reconstruction of Invariant Masses in Multijet Events*, Delphi Note 91-17 PHYS 88.

[41] DELPHI Collaboration, P.Abreu *et al.*, Z. Phys. **C73** (1996) 11.

[42] DELPHI Collaboration, DELSIM, Delphi Event Generation and Detector Simulation User's guide, DELPHI Note 89-67 PROG 142 (1989).

[43] F.A. Berends, R. Pittau, R. Kleiss, *Comput. Phys. Commun.* **85** (1995), 437.

[44] P.Abreu, D. Fassouliotis, A. Grefrath, R.P. Henriques, L. Vitale, *SPRIME, A Package for Estimating the Effective $\sqrt{s'}$ Centre of Mass Energy in $q\overline{q}(\gamma)$ Events*, DELPHI Note 96-124 PHYS 632.

[45] G.Borisov, *Lifetime Tag of Events $Z^0 \rightarrow b\overline{b}$ with the DELPHI Detector*, DELPHI 94-125 PROG 208 (1994).

[46] G.Borisov, *Combined b-tagging*, DELPHI 97-94 PHYS 716 (1997).

[47] G.V. Borisov, Lifetime Tag of events $Z^0 \rightarrow b\overline{b}$ with the DELPHI detector, DELPHI 94-125 (1994).

[48] G.J. Feldman, R.D. Cousins, Phys. Rev. **D57**, 3873 (1998).

[49] R.D. Cousins, Am. J. Phys. **63**, 398 (1995).

[50] A.L. Read, Optimal statistical analysis of search results based on the likelihood ratio and its application to the search for the MSM Higgs boson at $\sqrt{(}s)$=161 and 172 GeV, DELPHI 97-158 PHYS 737 (1997).

[51] R.M. Barnett *et al.*, Review of Particle Physics, Phys. Rev. **D54** (1996).

[52] W.H. Press *et al.*, *Numerical recipes*, Cambridge Univ. Press (1992).

[53] DELPHI Collaboration, P. Abreu *et al.*, Search for charged Higgs bosons in e^+e^- collisions at $\sqrt{s} = 172$ GeV, Phys. Lett., B : 420 (1998).

[54] ALEPH Collaboration, R. Barate *et al.*, Search for charged Higgs bosons in e^+e^- collisions at $\sqrt{s} = 181$-184 GeV, CERN-EP-99-011 (1999).

[55] OPAL Collaboration, G. Abbiendi *et al.*, Search for Higgs Bosons in e^+e^- Collisions at 183 GeV, CERN-EP-98-173 (1998).

[56] D0 Collaboration, B. Abbott *et al.*, Search for charged Higgs bosons in decays of top quark pairs, hep-ex/9902028 (1999).

Izjavljam, da je disertacija rezultat samostojnega raziskovalnega dela.

V Ljubljani, aprila 1999.

Samo Stanič